SANDIA REPORT

SAND2015-9860
Unlimited Release
Printed November 9, 2015

Implementing and diagnosing magnetic flux compression on the Z pulsed power accelerator

R. D. McBride, D. E. Bliss, M. R. Gomez, S. B. Hansen, M. R. Martin, C. A. Jennings, S. A. Slutz, D. C. Rovang, P. F. Knapp, P. F. Schmit, T. J. Awe, M. H. Hess, R. W. Lemke, D. H. Dolan, D. C. Lamppa, M. R. L. Jobe, L. Fang, K. D. Hahn, G. A. Chandler, G. W. Cooper, C. L. Ruiz, A. J. Maurer, G. K. Robertson, M. E. Cuneo, D. B. Sinars, K. Tomlinson, G. Smith, R. R. Paguio, T. P. Intrator, T. E. Weber, and J. B. Greenly

Prepared by
Sandia National Laboratories
Albuquerque, New Mexico 87185 and Livermore, California 94550

Sandia National Laboratories is a multi-program laboratory managed and operated by Sandia Corporation, a wholly owned subsidiary of Lockheed Martin Corporation, for the U.S. Department of Energy's National Nuclear Security Administration under contract DE-AC04-94AL85000.

Sandia National Laboratories

Issued by Sandia National Laboratories, operated for the United States Department of Energy by Sandia Corporation.

Available to DOE and DOE contractors from
U.S. Department of Energy
Office of Scientific and Technical Information
P.O. Box 62
Oak Ridge, TN 37831

Telephone: (865) 576-8401
Facsimile: (865) 576-5728
E-Mail: reports@adonis.osti.gov
Online ordering: http://www.osti.gov/bridge

Available to the public from
U.S. Department of Commerce
National Technical Information Service
5285 Port Royal Rd
Springfield, VA 22161

Telephone: (800) 553-6847
Facsimile: (703) 605-6900
E-Mail: orders@ntis.fedworld.gov
Online ordering: http://www.ntis.gov/help/ordermethods.asp?loc=7-4-0#online

SAND2015-9860
Unlimited Release
Printed November 9, 2015
Reprinted November 9, 2015

Implementing and diagnosing magnetic flux compression on the Z pulsed power accelerator

R. D. McBride,[1] D. E. Bliss,[2] M. R. Gomez,[3] S. B. Hansen,[4] M. R. Martin,[5] C. A. Jennings,[4] S. A. Slutz,[4] D. C. Rovang,[1] P. F. Knapp,[1] P. F. Schmit,[4] T. J. Awe,[1] M. H. Hess,[4] R. W. Lemke,[5] D. H. Dolan,[6] D. C. Lamppa,[7] M. R. L. Jobe,[7] L. Fang,[8] K. D. Hahn,[9] G. A. Chandler,[9] G. W. Cooper,[9] C. L. Ruiz,[9] A. J. Maurer,[10] G. K. Robertson,[10] M. E. Cuneo,[11] and D. B. Sinars[12]

[1]High Energy Density Experiments, Org. 1688
[2]Imaging and Spectroscopy, Org. 1675
[3]Radiation and Fusion Experiments, Org. 1683
[4]Radiation and ICF Target Design, Org. 1684
[5]High Energy Density Physics Theory, Org. 1641
[6]Dynamic Material Properties, Org. 1646
[7]Electromagnetic Launch Systems, Org. 5445
[8]Microsystems Integration, Org. 1718
[9]Neutron and Particle Diagnostics, Org. 1677
[10]Load and Diagnostic Engineering, Org. 1678
[11]Pulsed Power Accelerator Science and Technology, Org. 1650
[12]Radiation and Fusion Physics, Org. 1680

Sandia National Laboratories
P.O. Box 5800
Albuquerque, NM 87185–MS1193

K. Tomlinson, G. Smith, and R. R. Paguio
General Atomics
San Diego, CA 92186

T. P. Intrator and T. E. Weber
P-24 Plasma Physics
Los Alamos National Laboratory
Los Alamos, NM 87545

J. B. Greenly
Laboratory of Plasma Studies
Cornell University
Ithaca, NY 14853

Abstract

We report on the progress made to date for a Laboratory Directed Research and Development (LDRD) project aimed at diagnosing magnetic flux compression on the Z pulsed-power accelerator (0–20 MA in 100 ns). Each experiment consisted of an initially solid Be or Al liner (cylindrical tube), which was imploded using the Z accelerator's drive current (0–20 MA in 100 ns). The imploding liner compresses a 10-T axial seed field, $B_z(0)$, supplied by an independently driven Helmholtz coil pair. Assuming perfect flux conservation, the axial field amplification should be well described by $B_z(t) = B_z(0) \times [R(0)/R(t)]^2$, where R is the liner's inner surface radius. With perfect flux conservation, $B_z(t)$ and dB_z/dt values exceeding 10^4 T and 10^{12} T/s, respectively, are expected. These large values, the diminishing liner volume, and the harsh environment on Z, make it particularly challenging to measure these fields. We report on our latest efforts to do so using three primary techniques: (1) micro B-dot probes to measure the fringe fields associated with flux compression, (2) streaked visible Zeeman absorption spectroscopy, and (3) fiber-based Faraday rotation.

We also mention two new techniques that make use of the neutron diagnostics suite on Z. These techniques were not developed under this LDRD, but they could influence how we prioritize our efforts to diagnose magnetic flux compression on Z in the future. The first technique is based on the yield ratio of secondary DT to primary DD reactions. The second technique makes use of the secondary DT neutron time-of-flight energy spectra. Both of these techniques have been used successfully to infer the degree of magnetization at stagnation in fully integrated Magnetized Liner Inertial Fusion (MagLIF) experiments on Z [P. F. Schmit *et al.*, Phys. Rev. Lett. **113**, 155004 (2014); P. F. Knapp *et al.*, Phys. Plasmas, **22**, 056312 (2015)].

Finally, we present some recent developments for designing and fabricating novel micro B-dot probes to measure $B_z(t)$ inside of an imploding liner. In one approach, the micro B-dot loops were fabricated on a printed circuit board (PCB). The PCB was then soldered to off-the-shelf 0.020-inch-diameter semi-rigid coaxial cables, which were terminated with standard SMA connectors. These probes were recently tested using the COBRA pulsed power generator (0–1 MA in 100 ns) at Cornell University. In another approach, we are planning to use new multi-material 3D printing capabilities to fabricate novel micro B-dot packages. In the near future, we plan to 3D print these probes and then test them on the COBRA generator. With successful operation demonstrated at 1-MA, we will then make plans to use these probes on a 20-MA Z experiment.

Acknowledgment

We would like to thank the MagLIF/ICF and the Dynamic Material Properties research groups at Sandia National Laboratories for many useful technical discussions regarding various aspects of magnetic flux compression on Z.

We would also like to thank the personnel of the Pulsed-Power Sciences Center (including the Z and ZBL facilities) at Sandia National Laboratories and the personnel of the Laboratory of Plasma Studies (including the COBRA facility) at Cornell University; without their hard work and dedication, this work would not have been possible.

This work was funded by the Laboratory Directed Research and Development Program at Sandia National Laboratories under Project Number 165736. Sandia National Laboratories is a Multi-Program Laboratory managed and operated by Sandia Corporation, a wholly owned subsidiary of Lockheed Martin Corporation, for the U.S. Department of Energy's National Nuclear Security Administration under Contract Number DE-AC04-94AL85000.

Contents

1 Introduction **17**

2 A description of magnetic flux compression **21**

3 Experiments on the Z accelerator **25**

3.1 Diagnostics development 27

3.1.1 Micro B-dots: The challenges of using micro B-dot probes for measuring magnetic flux compression directly, and the challenges and use of micro B-dot probes to measure the fringe fields associated with magnetic flux compression on the Z accelerator 27

3.1.2 Streaked visible spectroscopy (SVS): SVS for measuring Zeeman-split absorption features and inferring the associated flux-compressed magnetic field on Z 33

3.1.3 Faraday rotation: A fiber-based Faraday rotation diagnostic for directly measuring flux-compressed magnetic fields inside of an imploding liner on Z 34

3.2 Liner implosion design work to improve implosion stability and thus improve compatibility for probe measurements of magnetic flux compression 40

3.3 Early experimental results 44

3.3.1 Micro B-dot measurements on Z shot 2537 44

3.3.2 Micro B-dot measurements on Z shot 2592 46

3.3.3 SVS measurements on Z shot 2592 47

3.3.4 SVS measurements on Z shots 2592, 2653, and 2713 48

3.3.5 Faraday rotation and other measurements on Z shots 2592 and 2653 48

3.4 Latest experimental results: Z shot 2713 49

3.4.1 Faraday rotation and micro B-dot measurements on Z shot 2713 49

3.4.2 SVS measurements on Z shot 2713 50

3.4.3 Load current measurements on Z shot 2713 51

3.5 New design for flux compression experiments scheduled for November of 2015 . . . 51

4 Micro B-dot package development and experiments on the COBRA facility 55

4.1 Design and fabrication of the "quad-pack" micro B-dot package 55

4.2 Testing of the "quad-pack" at Cornell University's COBRA facility 61

4.3 Design of a novel differential micro B-dot package to be fabricated using new multi-material 3D printing technology 64

5 Conclusion 71

References 73

Appendix

A An obsolete lens-coupled setup for SVS measurements on Z 83

B GORGON simulations to study the effects of the metallic load hardware on the dynamic fringe fields 85

C GORGON design simulations to compare a plastic liner fill with a vacuum liner fill 87

D Conference presentations associated with this LDRD project 89

List of Figures

1.1 Illustration of magnetized liner inertial fusion (MagLIF), highlighting the important flux compression component of the concept. 18

2.1 Conceptual illustration of magnetic flux compression. The solid red boxes indicate the position and volume occupied by the liner at various times during the implosion. The dashed red boxes indicate the liner's initial position when the liner implosion is in progress (thus the solid red boxes are contained within the dashed red boxes). In the first plot, the liner is in its initial position prior to the implosion. In the second and third plots, the liner is in flight while the implosion proceeds. The sum of the static initial field $B_z(0)$ and the dynamic solenoidal field [due to $J_\theta(z)$ on the liner's inner surface] is the total flux-conserved field $B_z(t)$. The red mark located on axis 1 mm above the top of the liner illustrates where we have placed micro B-dot probes to measure the solenoidal fringe fields associated with flux compression on the Z accelerator. 22

2.2 Simulation of the MagLIF point design discussed in Ref. [1]. Plotted are the drive current (black), the liner implosion trajectory (brown), and the radially-averaged axial magnetic field (red). 24

3.1 Experimental platform developed for diagnosing vacuum magnetic flux compression on the Z pulsed power accelerator. The red region of the on-axis Faraday fiber represents the 3-mm-long terbium (Tb) doped magneto-optical region of the probe. 26

3.2 Various construction and fielding configurations for single-ended coaxial-cable-based micro B-dot probes. (a) Standard loop construction enabling measurements of $B_\theta(t)$ and/or $B_r(t)$ inside of an imploding liner. This is the configuration that was used in Ref. [8] to measure $B_\theta(t)$ inside of an imploding liner on Z. (b) An approach to reorienting the plane of the micro B-dot loop to enable $B_z(t)$ measurements inside of an imploding liner. As indicated by the illustration, this approach gives rise to a vertical standoff issue, where the probe is sensitive not only to the desired $B_z(t)$ field, but also to the unwanted perpendicular components $B_\theta(t)$ and/or $B_r(t)$. A mitigation strategy for the standoff issue is provided below in Sec. 4.1. (c) An approach to reorienting the plane of the micro B-dot loop to enable $B_z(t)$ measurements inside of an imploding liner while eliminating the vertical standoff issue. This technique has been used at Cornell to construct some novel micro B-dot probes [73], and it is the basis for the novel 3D printed probe design discussed below in Sec. 4.3. In (b) and (c), the coaxial cable's outer conductor is flux excluding to the B_z field because the outer conductor, with its high conductivity, supports azimuthal current densities J_θ along its outer surface. (d) Standard loop construction enabling measurements of $B_z(t)$ in the fringe field region above an imploding liner. This is the fielding configuration that was used for the Z experiments of this LDRD project. We fielded four of these probes per shot and paired them off ('+' probes with '−' probes), and thus we effectively fielded two differential pairs per shot. . . . 29

3.3 An example of using the simple field solver tool, coupled to the SAMM code, that was developed to understand fringe field micro B-dot voltage responses as well as how these voltage responses relate to the flux compressed $B_z(t)$ field down inside the heart (origin) of the imploding liner. The dashed vertical lines indicate the times when convergence ratios of interest occur, i.e., when $C_R = 3$, 5, and 10 occur. The second plot from the top shows how we used this tool to quickly assess how uncertainties in the probes axial positioning could affect the voltage responses. This figure demonstrates the overall difficulty of using this method to assess $B_z(t)$ down inside the imploding liner, especially at high convergence ratios. 32

3.4 Illustration of the Faraday Effect [77]. Here, **E** is the electric field vector of the linearly polarized light and **B** is the magnetic field that one would like to diagnose. The plane of polarization is rotated by an angle β after the light propagates a distance d through the cylindrical magneto-optical fiber with Verdet constant $\mathscr{V}$. . . 35

3.5 (a) Conceptual illustration of the Tb-doped Faraday rotation probe. (c)–(d) Photographs of the bench testing conducted at Los Alamos National Laboratory. (b) The optical board with various components. (c) The solenoid coil that the Tb-doped magneto-optical fiber and a reference B-dot probe were placed inside of for testing and calibration. (d) The overall testing and calibration setup. 36

3.6 (a) Schematic of the Faraday rotation diagnostic system. (b) Schematic of the Faraday rotation diagnostic system integrated into the Z facility. 37

3.7 Faraday probe calibration data taken at the Systems Integration Test Facility (SITF) at Sandia National Laboratories. 38

3.8 Results from a SAMM simulation to better understand how fast the polarization would be oscillating as a function of time, liner convergence, and flux compressed magnetic field strength. The horizontal red line indicates the outer radius of the Faraday probe and the vertical red lines indicate the time when the liner's inner surface first impacts the Faraday probe. 39

3.9 GORGON 2D simulation results illustrating an end-effect instability. 40

3.10 GORGON 2D simulation of a "thick-end" design for mitigating end-effect instabilities. This design looked at the effects of thickening the ends of the liner. This design could work, but would require a large Δz between the approximately cylindrical region of the implosion and the undisturbed region far above the liner where one might consider placing a probe. 41

3.11 GORGON 2D simulation of a "cushion" design for mitigating end-effect instabilities. This design uses the higher density aluminum (Al) "cushion" to hold back the instability as the instability breaks through the lower density beryllium (Be) liner. This is the design that we ultimately chose for some of our first flux compression experiments on the Z accelerator (shots 2494 and 2537). 42

3.12 ALEGRA 2D simulation of a liner design that was intentionally "over-massed" to preserve an ideal cylindrical geometry during the implosion. This liner was designed to coast to the cylindrical axis of symmetry after having some momentum imparted to it during the fast Z pulse. The lack of drive pressure during the implosion preserves the cylindrical geometry by avoiding driving instabilities like end-effect instabilities. This design was tested on Z shot 2493. 43

3.13 A description of the target for Z shot 2537 and the resulting micro B-dot probe data. The peak of the voltage and the shape of the voltage waveform were much different than what was expected based on the simple solenoidal field solution in the SAMM calculation. Post-shot GORGON simulations suggest that the signals don't agree with the vacuum solenoid field solution because a plasma jet forms on axis, which advects B_z into the probe region rapidly. 45

3.14 The single-ended voltage from one of the two micro B-dot probes of the lower differential pair on Z shot 2592 (its differential pair partner failed early in the shot). Here the waveform looks much more like what is expected from the simple solenoidal field solver tool (in contrast to the micro B-dot data shown in Fig. 3.13 for shot 2537, where the experimental data did not look like what was expected from the solenoidal field solver tool). We believe that the better agreement here for shot 2592 is because the on-axis Faraday probe and the filled dielectric end cap eliminated the possibility of an on-axis plasma jet interacting with the micro B-dot probes. Also note that the experimental voltage waveform swings positive due to bounce sooner than in the simulation. However, this is likely because the liner bounces sooner in the experiment due to hitting the on-axis Faraday probe. The presence of the Faraday probe was not accounted for in the simulation. 46

3.15 Streaked visible spectroscopy (SVS) data collected on Z shot 2592. (a) The streaked image. The green dashed line is the time of shock breakout from the liner wall. The red dashed line is the time when the liner hits the Faraday rotation probe. (b) A lineout through the streaked image at $t = 3065$ ns and simulated lineouts for $B_z = 20$ T and 30 T. The agreement between the simulated and experimental lineouts indicates that the flux compressed B_z field in the experiment was in the range of 20–30 T at $t = 3065$ ns. 47

3.16 Faraday rotation data and fringe-field micro B-dot data obtained on Z shot 2713. SAMM simulation data are shown for comparison and for a timing reference. The single-ended measurements from the two micro B-dot probes that comprise the upper differential pair are shown. The agreement between the two single-ended measurements indicates very little common-mode noise. The error bars shown for the simulated micro B-dot voltage is due to the uncertainty in the axial positioning of the micro B-dot probes above the liner. Note that both of the upper micro B-dot probes fail at about the same time, which is shortly after the lower pair (not shown) failed. Also note that the Faraday rotation measurement failed shortly after the micro B-dot measurements. These relative timings for probe failures provide supporting evidence for the possible failure mechanism described in the text (i.e., an axially-propagating magnetic bubble/pressure wave that first crushes the micro B-dot probes and then races down the micro B-dot feedthrough channels, destroying the on-axis Faraday rotation probe; this failure mechanism will hopefully be eliminated in future experiments using the new design discussed below in Sec. 3.5). 49

3.17 The Z shot 2713 liner target mounted in surrounding electrode hardware [anode (top) and cathode (bottom)]. Also shown are two micro B-dot probes (one from each of the differential pair heights fielded above the liner) and the Faraday rotation fiber fielded on axis. The red region of the on-axis Faraday fiber represented the 3-mm-long terbium (Tb) doped magneto-optical region of the probe. 50

3.18 (a) Upstream and downstream current pulses measured/inferred for Z shot 2591 (a short-pulse fully integrated MagLIF shot using the standard MagLIF feed and a liner with an outer radius of 2.79 mm [16]). (b) Upstream and downstream current pulses measured on Z shot 2713 (a long-pulse flux compression shot using the standard MagLIF feed and a liner with an outer radius of 5 mm). Comparing the two shots, the significantly smaller difference between the upstream and downstream current on shot 2713 indicates significantly lower current loss on shot 2713. Here, "upstream" and "downstream" is with respect to the post-hole convolute region on Z. Thus, the current loss that we are referring to here presumably occurs in the post-hole convolute region. 51

3.19 The new liner target design that will be tested on Z in November of 2015. This design attempts to maximize the robustness of the Faraday rotation measurement. . 52

3.20 ALEGRA 2D simulation of the new liner target design shown in Fig. 3.19. This design attempts to maximize the robustness of the Faraday rotation measurement and will be tested on Z in November of 2015. 53

4.1 Standard true differential probe construction using coaxial cables. This particular implementation is not conducive to measurements of $B_z(t)$ inside of an imploding liner [only $B_\theta(t)$ and/or $B_r(t)$ could be measured reasonably well inside of an imploding liner with this configuration]. 56

4.2 Conceptual illustration of the quad-pack design. 57

4.3 Conceptual illustration showing the effective loop areas that are sensitive to $B_z(t)$ assuming a perfectly symmetric radial fanout of the B field as the field lines approach the flux excluding region from below. 58

4.4 Graphics from the SolidWorks model of the quad-pack design. The magnetic field lines (purple arrows) are visual aids for understanding the conceptual operation of the quad-pack and the areas of the probe that are sensitive to $B_z(t)$. The PCB is partially transparent for illustrative purposes. In (b), the two regions within the dashed red lines represent the areas of the two differential loops that are effectively sensitive to $B_z(t)$, assuming a symmetric radial fanout of the B-field around the flux excluding region. In practice, the probes are calibrated relative to a known reference to find the true sensitivity to $B_z(t)$. 58

4.5 (a) Engineering drawing for the printed circuit board (PCB) component of the quad-pack micro B_z-dot design. Here the signal numbering convention (1–4) is also indicated. (b) SolidWorks model graphics illustrating the careful attention paid to proper SMA connectorization for the quad-pack design. 59

4.6 Photographs of the various scale sizes involved with quad-pack assembly. (a) Tweezers holding an 0.020" semi-rigid coaxial cable soldered to a quad-pack PCB under the microscope that was purchased to enable quad-pack assembly. (b) That in (a) zoomed in. (c) That in (b) zoomed in. (d) That in (c) zoomed in. In (d), the poor quality of the PCB traces and vias that resulted from earlier PCB fabrication attempts at local shops is apparent. (e) The much improved PCB trace and via quality obtained from Sierra Circuits Proto Express in California. (f) That in (e) after solder has been applied to assemble the quad-pack. (g) Slightly rotated view of that in (f) for perspective. (h) Full view of a completed quad-pack assembly. . . . 60

4.7 Photographs of the experimental setup for COBRA shot 3705. (The 3704 setup was similar.) 62

4.8 Photographs of the experimental setup for COBRA shot 3706. 62

4.9 Photographs of the experimental setup for COBRA shot 3707. 63

4.10 Photographs of the experimental setup for COBRA shot 3708. 63

4.11 Photographs of the experimental setup for COBRA shot 3709. 64

4.12 Experimental data collected for COBRA shots 3704–3706. The raw signal voltages are presented in the left column. The time-integrated signals are presented in the right column. The error bars indicate the spread between the two differential pairs of the quad-packs. Large error bars indicate large cross-cutting (non-axial) field components and possibly other non-ideal behavior. On shot 3704, quad-pack differential pair A failed at $t = 1906$ ns; after $t = 1906$ ns, a constant ratio of differential pair A to differential pair B was assumed (which is the ratio of the two pairs at $t = 1906$ ns) to generate the mean axial field plotted. In general, the waveform shapes of the axial fields measured by the quad-packs agree well with the waveform shapes of the COBRA load current measured by a Rogowski coil and, on shot 3706, the waveform shape of the fringe field measured by a standard Cornell micro B-dot probe. Notably, excellent quad-pack results were obtained on shot 3704. . . . 65

4.13 Experimental data collected for COBRA shots 3707–3709. The raw signal voltages are presented in the left column. The time-integrated signals are presented in the right column. The error bars indicate the spread between the two differential pairs of the quad-packs. Large error bars indicate large cross-cutting (non-axial) field components and possibly other non-ideal behavior. In general, the waveform shapes of the axial fields measured by the quad-packs agree well with the waveform shapes of the COBRA load current measured by a Rogowski coil and the waveform shapes of the fields measured by Cornell micro B-dot probes. Notably, excellent quad-pack results were obtained on shot 3707. 66

4.14 Four-frame, time-gated XUV pinhole camera images taken during the COBRA experiments. Both side-on and axial views were obtained, though the axial views were often problematic due to obstructions and/or other technical difficulties. These images reveal the presence of plasmas in and around the various load coils tested. These plasmas could have been the culprit for some of the non-ideal behavior observed in the quad-pack data. 67

4.15 Multi-material 3D printing capabilities at EoPlex in San Jose, California. 68

4.16 The design of a novel differential micro B-dot package to be fabricated using new multi-material 3D printing technology. 69

List of Tables

3.1 Overview of the Z shots designed and executed for this LDRD project. SVS stands for streaked visible spectroscopy (which was used for Zeeman absorption spectroscopy). The '×' symbol for Faraday rotation on shot 2653 indicates that we intended to field the Faraday rotation probe, but the Faraday fiber housed within the target broke at some point prior to the shot. The three TBD shots indicate a future shot series; their experiment dates below are those published on the Z shot schedule at the time of this writing. 26

Chapter 1

Introduction

The Magnetized Liner Inertial Fusion (MagLIF) concept [1, 2] is presently being investigated experimentally [3–20] using the Z facility [21, 22] at Sandia National Laboratories. MagLIF is part of a broader class of concepts referred to collectively as magneto-inertial fusion (MIF) [23–40]. These concepts seek to significantly reduce the implosion velocity and pressure requirements of traditional inertial confinement fusion (ICF) [41–45] by using a magnetic field to thermally insulate hot fuel [46] from a cold pusher and to increase fusion product confinement.

The MagLIF concept at Sandia (see Fig. 1.1) uses the electromagnetic pulse supplied by the Z accelerator to radially implode an initially solid cylindrical metal tube (liner) filled with preheated and premagnetized fusion fuel (deuterium or deuterium-tritium). The implosion is a result of the fast z-pinch process, where a large gradient in the applied magnetic field pressure operates near the liner's outer surface [5, 47]. The fuel preheating is accomplished using the 1-TW Z beamlet laser (ZBL) [16, 48], and the fuel premagnetization is accomplished using the Applied B on Z (ABZ) axial field coil system [49]. One- and two-dimensional simulations of MagLIF using the LASNEX radiation magnetohydrodynamics code [50] predict that if sufficient liner integrity can be maintained throughout the implosion, then significant fusion yield (>100 kJ) can be attained on the Z accelerator when deuterium-tritium fuel is used and the accelerator's Marx generators are charged to 95 kV to obtain a peak drive current of about 27 MA [1, 5].

Premagnetizing the fuel in MagLIF is necessary to keep the fuel hot during the relatively slow implosion of a MagLIF liner. The ABZ system supplies an axially-aligned B_z field of about 10–30 T. This initial seed field is to be amplified by a factor of 10^2–10^3 within the fuel-filled volume of the imploding liner via magnetic flux compression. This large axial field is required to mitigate energy loss from the fuel due to electron and ion thermal conduction. Additionally, the axial field should enhance α-particle confinement and heating of the fuel, and thus increase the overall fusion yield.

Since the MagLIF concept relies so heavily on the efficacy of magnetic flux compression, it is important for us to test our understanding of the phenomenon. For example, magnetohydrodynamics codes predict that flux loss can occur due to resistive diffusion into the liner wall and due to the Nernst thermo-electric effect [1, 51–53]; however, these physics, particularly the Nernst effect, are largely unvalidated, especially at the time scales and field values expected on Z [i.e., $B_z(t)$ and dB_z/dt values exceeding 10^4 T and 10^{12} T/s, respectively].

In order to test our understanding of the physics of magnetic flux compression, new diagnostics

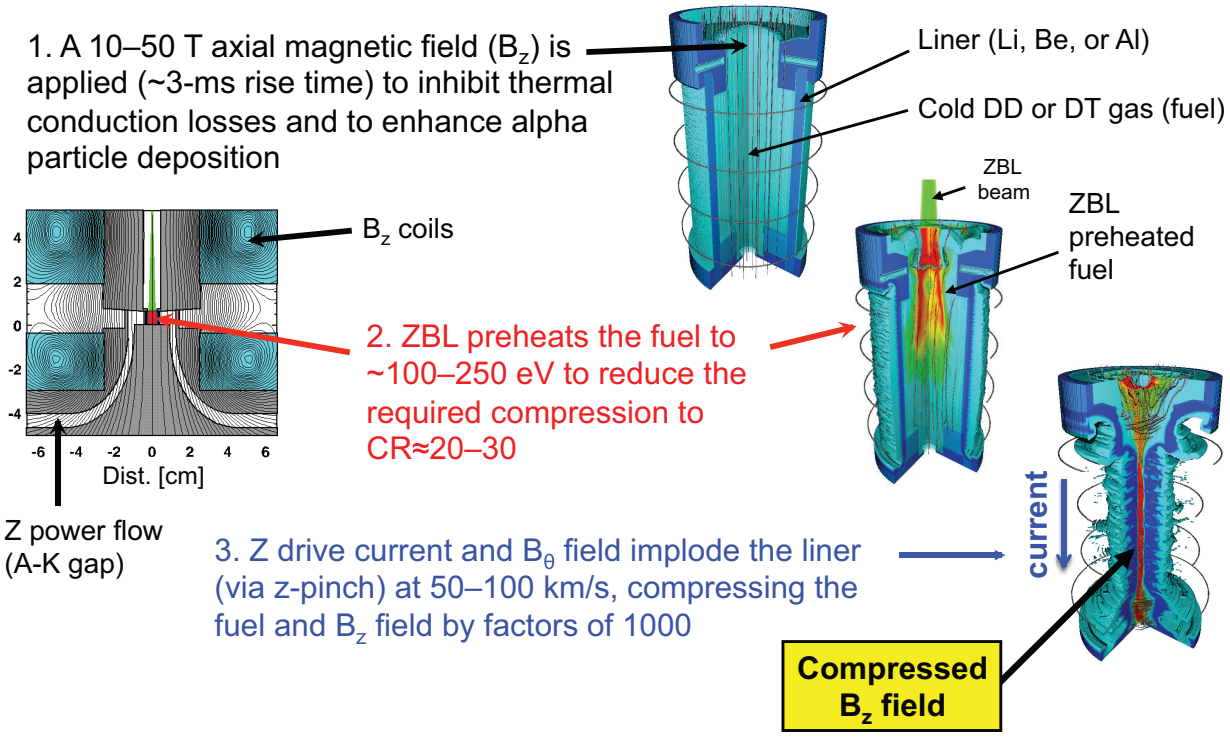

Figure 1.1: Illustration of magnetized liner inertial fusion (MagLIF), highlighting the important flux compression component of the concept.

capabilities are needed to measure the expected large magnetic fields. This is not trivial due to the harsh environment on Z, the diminishing liner volume during the implosion, and the large $B_z(t)$ and dB_z/dt values expected. Thus, a three-year Laboratory Directed Research and Development (LDRD) project was awarded to investigate possible solutions. The three primary techniques investigated during this project were: (1) micro B-dot probes to measure the fringe fields associated with flux compression, (2) streaked visible Zeeman absorption spectroscopy, and (3) fiber-based Faraday rotation. In this report, we present the progress made to date on each of these approaches.

This LDRD project also investigated various approaches for fabricating novel, compact micro B-dot packages for measuring dB_z/dt inside of an imploding liner directly. In one approach, the micro B-dot loops were fabricated on a printed circuit board (PCB). The PCB was then soldered to off-the-shelf 0.020-inch-diameter semi-rigid coaxial cables, which were terminated with standard SMA connectors (Sec. 4.1). These probes were recently tested using Cornell University's COBRA pulsed power generator (0–1 MA in 100 ns) [54]. We present the results of these initial tests in Sec. 4.2. In another approach, we are planning to use new multi-material 3D printing capabilities to fabricate novel micro B-dot packages. This new capability to 3D print structures with both electrical insulators and electrical conductors in the same package has only just recently become available (within the past few months at the time of this writing). In the near future, we plan to fabricate 3D printed probes and test them on the COBRA generator. With successful operation demonstrated at 1 MA, we will then make plans to use these probes on a 20-MA Z experiment. We present our designs for these novel 3D printed micro B-dot packages in Sec. 4.3.

We also mention here that during the course of this project, two new and unexpected techniques were developed that make use of the neutron diagnostics suite on Z. These neutron-based techniques were not developed under this LDRD, but they could influence how we prioritize our efforts to diagnose magnetic flux compression on Z in the future. The first of these two techniques makes use of the ratio of the total number of secondary DT reactions to the total number of primary DD reactions that occurred during the experiment. The total primary and secondary yields used to calculate this ratio are obtained from the data of neutron activation samples. The second technique makes use of the secondary DT neutron energy spectra, which is unfolded from neutron time-of-flight data (i.e., this is essentially neutron spectroscopy). Both of these techniques have been used successfully to infer the degree of magnetization at stagnation in fully integrated MagLIF experiments on Z. These efforts are described in detail in Refs. [17] and [20]. These studies found that the degree of magnetization at stagnation is roughly consistent with that calculated in radiation magnetohydrodynamics simulations (i.e., on the order of 50% of the flux is conserved). These results have demonstrated that flux compression is indeed working in fully integrated MagLIF experiments.

Chapter 2

A description of magnetic flux compression

Magnetic flux compression has been studied previously in several contexts [55–68]. To first order, liner-driven magnetic flux compression can be described as follows. Let $R(t)$ represent the radius of the imploding liner's inner surface, and let $B_z(t)$ represent the magnetic flux density of the axial magnetic field that is being compressed. Prior to the fast ($\sim$ 100 ns) liner implosion, we apply the slow ($\sim$ 3 ms) ABZ pulse. On the long time scale of the ABZ pulse, the initial axial field has time to completely diffuse into the liner and its surrounding electrode structures, providing a uniform seed field, $B_z(0) \sim 10$ T. The total initial flux is then

$$\Phi_z(0) = B_z(0) \times \pi R^2(0). \tag{2.1}$$

With a uniform seed field and the total initial flux established, the Z accelerator is then pulsed, driving the fast liner implosion, which compresses the axial field. We will refer to the case where the liner contains only vacuum (i.e., no fuel or fuel preheating) as 'vacuum flux compression' and to the case with fuel and fuel preheating as 'MagLIF flux compression'. In both cases, magnetic flux compression relies on the concept of flux conservation. For example, first consider the case of vacuum flux compression. As the liner implodes, azimuthally directed electrical current (with current density J_θ) is generated near the liner's inner surface. This azimuthal current generates a dynamic solenoidal field that amplifies the initial seed field by the amount necessary to conserve the total flux trapped inside the liner, i.e., we have

$$\dot{\Phi}_z(t) = 0, \tag{2.2}$$

and thus

$$\Phi_z(t) = \Phi_z(0), \tag{2.3}$$

which implies

$$B_z(0) \times \pi R^2(0) = B_z(t) \times \pi R^2(t), \tag{2.4}$$

and thus

$$B_z(t) = B_z(0) \times \left[\frac{R(0)}{R(t)}\right]^2. \tag{2.5}$$

To support the boundary condition $B_r = 0$ at the liner's inner surface, we must have $J_\theta = J_\theta(z)$, where $J_\theta(z)$ is peaked near the ends of the liner [69, 70]. This $J_\theta(z)$ generates a dynamic self-consistent solenoidal field. The sum of this solenoidal field and the initial seed field gives the total flux-conserved field $B_z(t)$. This is illustrated conceptually in Fig. 2.1.

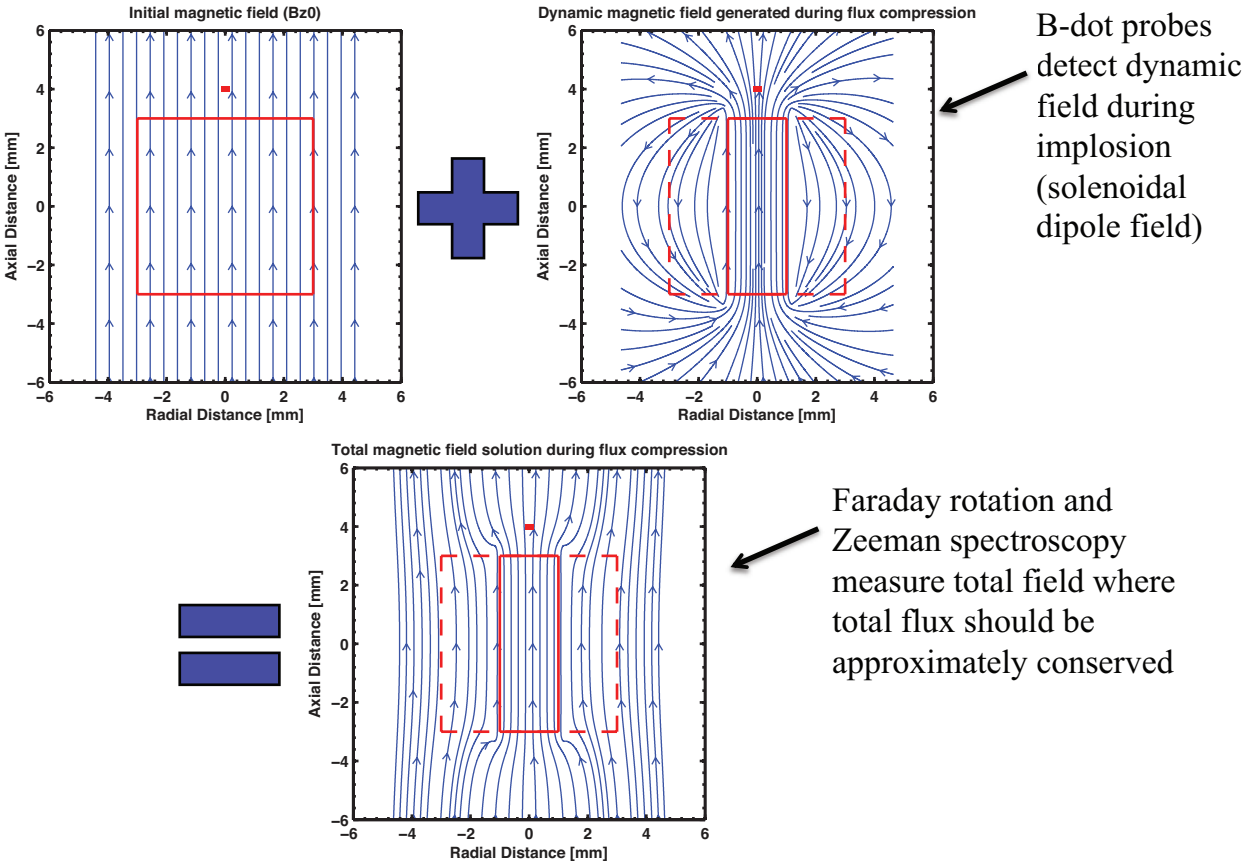

Figure 2.1: Conceptual illustration of magnetic flux compression. The solid red boxes indicate the position and volume occupied by the liner at various times during the implosion. The dashed red boxes indicate the liner's initial position when the liner implosion is in progress (thus the solid red boxes are contained within the dashed red boxes). In the first plot, the liner is in its initial position prior to the implosion. In the second and third plots, the liner is in flight while the implosion proceeds. The sum of the static initial field $B_z(0)$ and the dynamic solenoidal field [due to $J_\theta(z)$ on the liner's inner surface] is the total flux-conserved field $B_z(t)$. The red mark located on axis 1 mm above the top of the liner illustrates where we have placed micro B-dot probes to measure the solenoidal fringe fields associated with flux compression on the Z accelerator.

We note that this $J_\theta(z)$ current distribution likely causes additional localized heating near the ends of the liner during a flux compressing liner implosion. This localized heating could lead to more rapid flux loss near the ends of the liner due to resistive diffusion, and it could have implications for various liner implosion instabilities (i.e., the ends of the liner could become more unstable than the axial midpoint of the liner).

All of the flux compression experiments conducted for this LDRD used a platform developed to study vacuum flux compression (in order to better facilitate various probe development activities). In vacuum flux compression, the only real flux loss mechanism is resistive diffusion into the liner wall. The rate of this diffusion is affected by $J_\theta(z)$ and by the temperature-dependent conductivity of the liner material [since $J_\theta(z)$ heats the liner's inner surface]. By contrast, in MagLIF flux compression, flux loss can be due to a combination of resistive diffusion into the liner wall and temperature driven transport from the hot central fuel into the colder surrounding fuel and liner.

In general, we can describe flux loss in MagLIF as follows. Since hot fuel is involved, temperature gradients in the fuel can drive the transport of magnetic flux from the hot internal parts of the fuel to the cold external parts of the fuel near the liner's inner wall due to the Nernst thermoelectric effect [1, 51–53]. Then, as the liner implosion progresses, the liner's inner surface heats up due to $J_\theta(z)$ and due to the compressed hot fuel. Because of this, the liner's inner surface moves rapidly through many thermodynamic states with varying degrees of electrical conductivity. In some cases the liner's electrical conductivity can drop, enabling enhanced flux loss due to resistive diffusion from the fuel into the liner wall. In other words, the flux transported via the Nernst effect from the hot inner portions of the fuel to the colder surrounding parts of the fuel near the liner's inner surface can then rapidly diffuse into the cold liner wall [52], or it can be transported directly into the liner wall via the Nernst effect.

As shown in Ref. [53], the flux loss from the fuel directly into the liner wall due to the Nernst thermoelectric effect can be described in SI units by

$$\dot{\Phi}_z = \left[-2\pi r \cdot \mathscr{F}(x_e) \cdot \frac{k}{q_e} \frac{\partial T_g}{\partial r} \right]_{r=r_g} \tag{2.6}$$

$$\mathscr{F}(x_e) = \frac{1.5x_e^3 + 3.053x_e}{x_e^4 + 14.79x_e^2 + 3.7703}, \tag{2.7}$$

where r is the radial coordinate, r_g is the radius of the fuel-liner interface, k is the Boltzmann constant, q_e is the charge of an electron, $T_g = T_g(r,t)$ is the fuel temperature, $x_e \equiv \omega_{ce}\tau_{ei}$ is the electron Hall parameter, $\omega_{ce} = q_e B_{zg}/m_e$ is the electron cyclotron frequency, m_e is the mass of an electron, τ_{ei} is the average time between electron-ion collisions, and $\mathscr{F}(x_e)$ gives the so called "Braginskii coefficients" [51].

As an example of the effect that the Nernst mechanism can have on MagLIF, we consider the MagLIF point design presented in Ref. [1]. To do this, we first write Eq. 2.5 as

$$B_z(t) = B_z(0) \times \left[\frac{R(0)}{R(t)} \right]^2 = B_z(0) \times C_R^2(t), \tag{2.8}$$

where $C_R(t) \equiv R(0)/R(t)$ is the implosion convergence ratio. For the MagLIF point design discussed in Ref. [1], $B_z(0) = 30$ T and the maximum convergence ratio, which is obtained at the

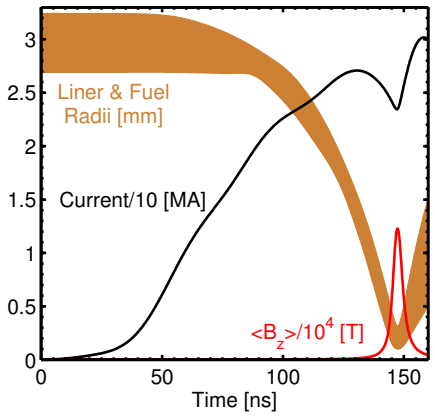

Figure 2.2: Simulation of the MagLIF point design discussed in Ref. [1]. Plotted are the drive current (black), the liner implosion trajectory (brown), and the radially-averaged axial magnetic field (red).

time of stagnation and peak fusion power, is $C_R(t_{stag}) \approx 25$. This means that with no flux loss, $B_z(t_{stag}) \approx 18{,}750$ T. However, as illustrated in Fig. 2.2, which comes from a simulation using the semi-analytic MagLIF model (SAMM) [53], and which included flux loss due to the Nernst effect, we find that the radially-averaged axial field at stagnation is only 12,275 T.

It is also important to note that in vacuum flux compression, within the imploding vacuum region, the axial field's spatial distribution is approximately constant, i.e., $B_z(r,z) \approx const.$ By contrast, in MagLIF flux compression, since the fuel is preheated at the start of the implosion, the axial field is "frozen in" to the fuel, and thus the field moves wherever the fuel density moves. This can be stated using the frozen-in expression $B_z(r)/\rho_g(r) = const. = \bar{B}_z/\bar{\rho}_g$, and thus

$$B_z(r) = \frac{\bar{B}_z}{\bar{\rho}_g}\rho_g(r), \tag{2.9}$$

where the overbars denote radially-averaged quantities and ρ_g is the mass density of the fuel. This frozen-in expression gives a decent first-order approximation for $B_z(r)$; however, it is also important to note that the Nernst effect fundamentally breaks this condition, since magnetic flux is transported independent of the fuel mass (*cf.* Eq. 2.6). Flux transport due to the Nernst effect depends only on $x_e \equiv \omega_{ce}\tau_{ei}$ and the fuel's temperature gradient $\partial_r T_g$.

Chapter 3

Experiments on the Z accelerator

The primary purpose of this LDRD project was to measure flux compressed magnetic fields on Z experiments. This required the development of several new diagnostic methods on Z as well as the design and execution of several Z experiments. The three primary diagnostic techniques investigated during this project were: (1) micro B-dot probes to measure the fringe fields associated with flux compression, (2) streaked visible Zeeman absorption spectroscopy, and (3) fiber-based Faraday rotation. To enable the fielding of these diagnostics on Z experiments, a new platform was developed. This platform, illustrated in Fig. 3.1, consisted of a liner target with custom-made nylon end caps for housing and securing the probes of the three main diagnostics described above.

Under this LDRD project, six shots dedicated to diagnosing magnetic flux compression were executed on the Z accelerator (see Table 3.1). For our first attempts, we designed imploding liner targets that would enable fringe field micro B-dot measurements above the imploding liner as well as streaked visible spectroscopy measurements by collecting light emanating from volume within the imploding liner. Faraday rotation was not attempted until later because the system was still being developed at Los Alamos National Laboratory. For many of these experiments, post-shot reports were written and archived on the MagLIF SharePoint site [71]. Additionally, at the time of this writing, three more shots are planned for November 2015, which is after this LDRD project officially closes.

In order to execute a flux compression shot, a new system had to be developed to supply the seed field $B_z(0)$. The system developed for Z is called Applied B on Z (ABZ), and it is described in detail in Ref. [49]. The initial prototyping and testing of the pulsed coil system (capacitor banks, controllers, coils, supporting hardware, etc.) were completed at the Systems Integration Test Facility (SITF) in the medium bay of building 970 at Sandia National Laboratories in a joint venture between Center 1600 (Pulsed Power Sciences) and Organization 5445 (Electromagnetic Launch Systems). The first Z shot with ABZ was fired on February 28, 2013 (which is after this LDRD project had already commenced).

During the first liner-driven flux compression shots (which were not part of this LDRD project, since diagnosing the flux compressed field was not an objective of the experiments), exciting unexpected results were immediately obtained via 6.151-keV x-ray radiography. Essentially, the inclusion of the ABZ field fundamentally changed the structure of the magneto-Rayleigh-Taylor instability from azimuthally-symmetric ring-like structure when $B_z(0) = 0$ [7, 8] to a 3D helical

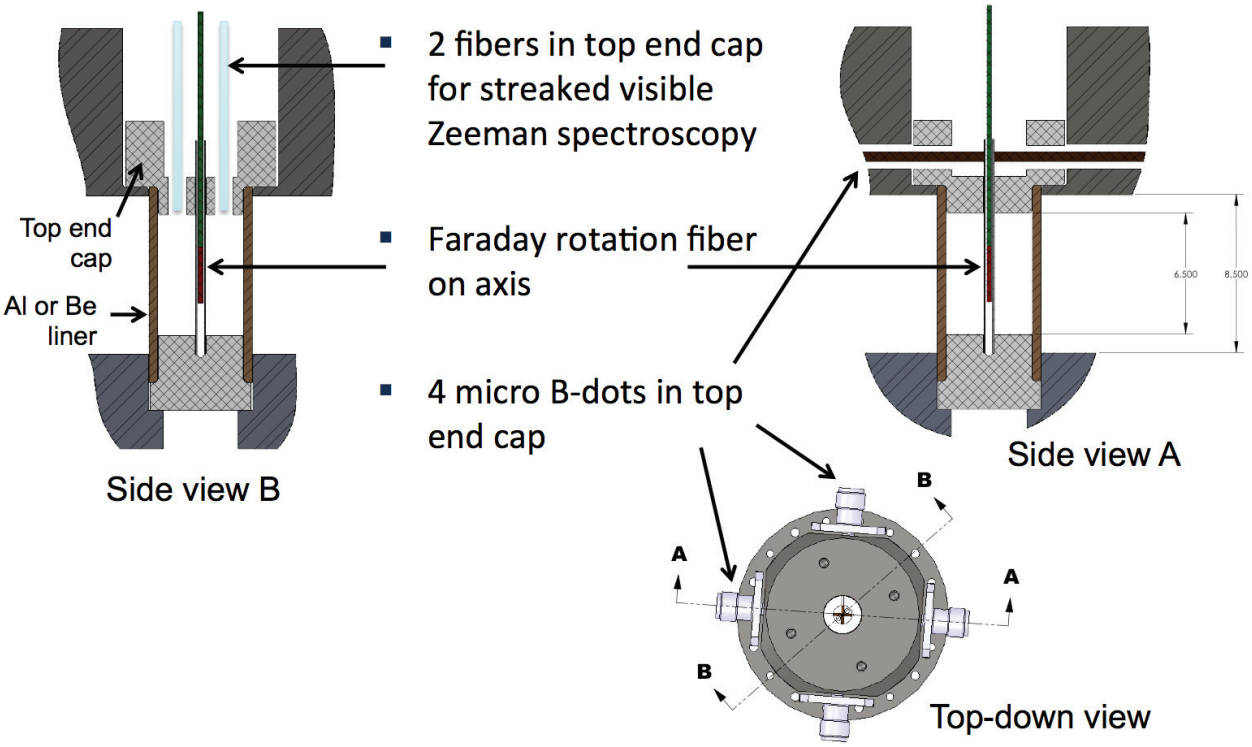

Figure 3.1: Experimental platform developed for diagnosing vacuum magnetic flux compression on the Z pulsed power accelerator. The red region of the on-axis Faraday fiber represents the 3-mm-long terbium (Tb) doped magneto-optical region of the probe.

Table 3.1: Overview of the Z shots designed and executed for this LDRD project. SVS stands for streaked visible spectroscopy (which was used for Zeeman absorption spectroscopy). The '×' symbol for Faraday rotation on shot 2653 indicates that we intended to field the Faraday rotation probe, but the Faraday fiber housed within the target broke at some point prior to the shot. The three TBD shots indicate a future shot series; their experiment dates below are those published on the Z shot schedule at the time of this writing.

Z Shot No.	Date of Experiment	$\mu\dot{B}$	SVS	Faraday	Radiography	VISAR	End Caps
2493	March 20, 2013	✓	✓		✓		Open Al
2494	March 21, 2013	✓	✓		✓		Open Al cushions
2537	July 23, 2013	✓	✓				Open Al cushions
2592	December 12, 2013	✓	✓	✓			Filled nylon cushions
2653	May 16, 2014	✓	✓	×			Filled nylon cushions
2713	September 22, 2014	✓	✓	✓		✓	Filled nylon cushions
TBD	November 11, 2015			✓		✓	Filled S/S conical glide planes
TBD	November 12, 2015			✓		✓	Filled S/S conical glide planes
TBD	November 13, 2015			✓		✓	Filled S/S conical glide planes

structure when $B_z(0)$ = 7–10 T [13, 14]. These results were not predicted by any of our advanced simulation codes, and thus these experiments serve as a good example of why it is important to study magnetic flux compression experimentally to validate our theories and simulation codes.

3.1 Diagnostics development

3.1.1 Micro B-dots: The challenges of using micro B-dot probes for measuring magnetic flux compression directly, and the challenges and use of micro B-dot probes to measure the fringe fields associated with magnetic flux compression on the Z accelerator

The micro B-dot probes used for the fringe field measurements were developed, fabricated, and calibrated at Cornell University [72]. The Cornell micro B-dot probes were fielded previously on Z to measure the $B_\theta(t)$ field within the vacuum filled interior of an imploding liner [8]. In this case, there was no ABZ field, and the B_θ field that was detected was the Z accelerator's drive field that had diffused through the liner wall into the liner's previously vacuum filled interior. These results were presented in detail in Ref. [8] (prior to the start of this LDRD project). These experiments demonstrated that the Cornell micro B-dot probes could be fielded within the vacuum filled interior of an imploding liner and still provide clean electrical signals, detecting only the signals of interest when the physical phenomena of interest commenced; in this case, the probes measured a rise from zero to roughly 20–50 T in about 50 ns. Also, these measurements were shown to be in good agreement with calculations using full radiation magnetohydrodynamics codes. Thus, we became interested in using these probes as a simple, low-cost, low-risk first approach for measuring flux compressed magnetic fields.

Despite these successes measuring $B_\theta(t)$ inside an imploding liner, there are several additional challenges to using a B-dot loop to measure $B_z(t)$ inside a flux compressing liner implosion. The first has to do with the physical size of the probes. Because $B_z(t)$ goes like $[R(0)/R(t)]^2$, the highest fields (i.e., the fields we are most interested in), don't occur until very late in the implosion. For example, if we want to measure the field at $C_R \approx 25$ (the C_R of the MagLIF point design), then $R(t) \approx 100$ μm. This is quite a bit smaller than the smallest B-dot packages made to date (that we are aware of), which are single-ended probes made from a single 0.020" semi-rigid coaxial cable, where $R_{probe} \geq 254$ μm [72].

A second challenge to using a B-dot loop to measure $B_z(t)$ within a flux compressing liner has to do with the natural orientation of the B-dot loop (*cf.* Fig. 3.2). Small B-dot probes are traditionally made from coaxial cable [*cf.* Fig. 3.2(a)]. At one end of the cable, the outer conductor and dielectric are stripped back some distance, exposing the solid inner conductor (which is essentially a thin copper wire). The exposed inner wire is then bent/wrapped back around and soldered to the outer conductor. The exposed wire soldered to the outer conductor now forms the pickup loop of the B-dot probe. The exposed loop and an appreciable length of the 0.020" coaxial cable are then embedded in a dielectric (usually a combination of epoxy and heat shrink tubing) to insulate

the metal components from the voltage potential of the plasma that the probes will be exposed to during an experiment. Note that in using this construction technique in its simplest implementation [Fig. 3.2(a)], the plane of the B-dot loop has a normal component that is always orthogonal to the axis of the semi-rigid coaxial cable. Thus, if we were to place one of these probes inside of an imploding liner, such that the semi-rigid cable ran coaxially with the imploding liner's cylindrical axis of symmetry, then the only field components that we could measure would be $B_r(t)$ and $B_\theta(t)$, since $B_z(t)$ is always orthogonal to the normal of the loop plane. Therefore, the loop planes must be reoriented 90° to enable a $B_z(t)$ measurement.

The reorientation of the loop plane can, however, lead to the vertical standoff issue illustrated in Fig. 3.2(b). Here the loop's vertical standoff, with a partial loop area A_2, makes the probe sensitive to the undesired orthogonal components, $B_r(t)$ and/or $B_\theta(t)$. Below, in Sec. 4.1, we present the "quad-pack" design, which attempts to mitigate this standoff issue by placing two loops with vertical standoffs close to one another, where the loops are wound in the opposite sense for measuring the unwanted orthogonal components, $B_r(t)$ and/or $B_\theta(t)$, and are wound in the same sense for measuring $B_z(t)$. With this configuration, the two probes will give the same result if $B_z(t)$ is the only component present; if a common orthogonal component is present, then the two signals will diverge in proportion to the strength of the orthogonal component. With precisely controlled loop areas, and by approximately collocating the two probe loops, the average of the two signals can be taken to approximate $B_z(t)$ (i.e., to reject the unwanted orthogonal component).

One way to eliminate the standoff issue all together is illustrated in Fig. 3.2(c). Here the idea is to split the outer conductor of the coaxial cable, pull the center conductor and the insulating dielectric through the split, loop the center conductor back around and solder the end of the center conductor to the outer conductor; once this is done, the split in the outer conductor can be closed and sealed shut with solder. This is essentially the method employed at Cornell to fabricate some novel micro B-dot probes that could be used to measure $B_z(t)$ inside an imploding liner [73].

Below, in Sec. 4.2, we present some experimental results where the quad-pack design was tested relative to these novel Cornell probes at Cornell's COBRA pulsed-power facility. With either of these off-the-shelf coaxial-cable-based probe designs, the overall size of the package is even larger than the minimum size discussed above ($R_{probe} \geq 254$ μm), which is already too large for our intended application. Therefore, in Sec. 4.3, we present another novel design that is conceptually similar to that shown in Fig. 3.2(c), but which could be fabricated using new multi-material 3D printing technology to obtain very small package dimensions. However, even with this new 3D printing capability, the package dimensions will still be larger than desired for our intended application.

A third challenge to using a B-dot loop to measure $B_z(t)$ inside of a flux compressing liner has to do with loop sensitivity and voltage breakdown. From differentiating Eq. 2.5, we find that

$$\dot{B}_z(t) = -2B_z(0)R^2(0)\frac{\dot{R}(t)}{R^3(t)}. \tag{3.1}$$

For the MagLIF point design, the peak implosion velocity is $\dot{R} \approx 80$ km/s, which occurs near the minimum radius $R \approx 100$ μm, and thus $\dot{B}_z$ values exceeding 1000 T/ns are expected. The loop

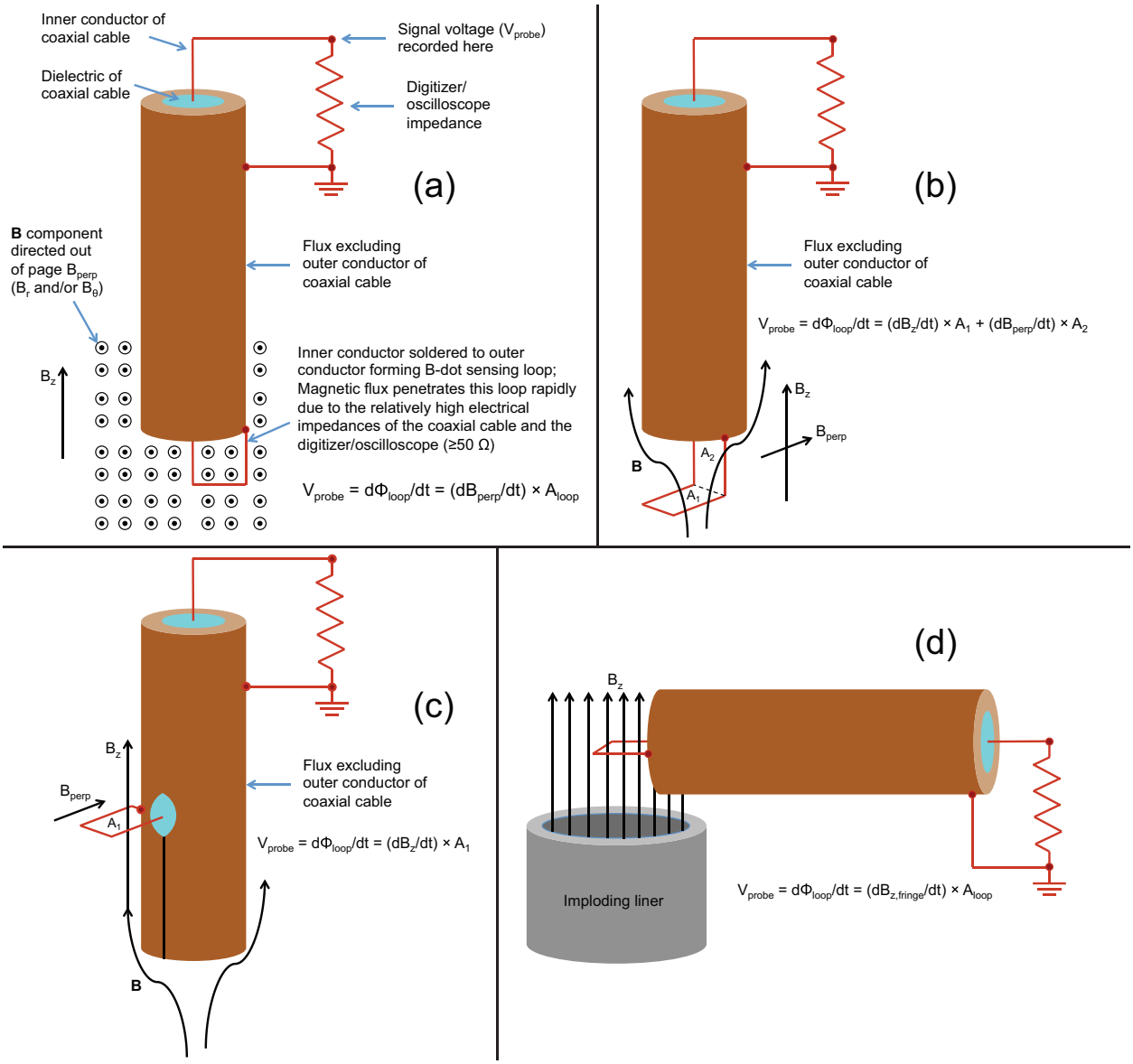

Figure 3.2: Various construction and fielding configurations for single-ended coaxial-cable-based micro B-dot probes. (a) Standard loop construction enabling measurements of $B_\theta(t)$ and/or $B_r(t)$ inside of an imploding liner. This is the configuration that was used in Ref. [8] to measure $B_\theta(t)$ inside of an imploding liner on Z. (b) An approach to reorienting the plane of the micro B-dot loop to enable $B_z(t)$ measurements inside of an imploding liner. As indicated by the illustration, this approach gives rise to a vertical standoff issue, where the probe is sensitive not only to the desired $B_z(t)$ field, but also to the unwanted perpendicular components $B_\theta(t)$ and/or $B_r(t)$. A mitigation strategy for the standoff issue is provided below in Sec. 4.1. (c) An approach to reorienting the plane of the micro B-dot loop to enable $B_z(t)$ measurements inside of an imploding liner while eliminating the vertical standoff issue. This technique has been used at Cornell to construct some novel micro B-dot probes [73], and it is the basis for the novel 3D printed probe design discussed below in Sec. 4.3. In (b) and (c), the coaxial cable's outer conductor is flux excluding to the B_z field because the outer conductor, with its high conductivity, supports azimuthal current densities J_θ along its outer surface. (d) Standard loop construction enabling measurements of $B_z(t)$ in the fringe field region above an imploding liner. This is the fielding configuration that was used for the Z experiments of this LDRD project. We fielded four of these probes per shot and paired them off ('+' probes with '−' probes), and thus we effectively fielded two differential pairs per shot.

voltage induced in the B-dot probe, which must be supported by the semi-rigid coaxial cable, is approximately

$$V_{probe}(t) = \dot{\Phi}_{loop}(t) = \dot{B}_z(t) \cdot A_{loop}, \tag{3.2}$$

where A_{loop} is the area of the probe's pickup loop. Since the 0.020" semi-rigid coaxial cables can support ~ 1 kV, we find that the probe's loop area must be less than 10^{-9} m^2 (this is a radius of 18 μm for a circular loop). To our knowledge, the smallest loop radii made to date using conventional methods are ~ 100 μm [72]; if these probes were to sense such rapidly increasing fields, the voltage would exceed 100 kV, which is much too high for the semi-rigid coaxial cable to support.

The challenges listed above, when taken together, do have a silver lining. The imploding liner will slam into the probe, destroying the probe and the measurement, at the probe radius $R_{probe} \geq 254$ μm. The silver lining is that the implosion velocity $\dot{R}$ is smaller and the liner radius R is larger than they would be at stagnation if the probe were not present, and thus the induced voltages in the probe are smaller. For example, if for practical reasons a probe cannot be made smaller than 1 mm in radius, then for the case of the MagLIF point design, when $R \approx 1$ mm, we have $\dot{B}_z \approx 30$ T/ns. Therefore, given the 1-kV cable limitation, the maximum tolerable loop radius could be increased from 18 μm to 100 μm, which is more feasible to fabricate by conventional means.

Despite the challenges, we have nevertheless pursued various research and development activities towards finding novel ways to fabricate micro B-dot packages that would be capable of measuring flux compressed fields inside of an imploding liner directly. We will refer to these packages as "true B_z-dot probes". The various activities to develop these packages are described below in Chapter 4. The various approaches attempted involve making the loops out of traces on a printed circuit board as well as printing the entire package using a new multi-material 3D printing capability that has only just recently become available (within the past few months at the time of this writing).

Since true B_z-dot probe development is still in its infancy, we decided to start with a simpler first approach for the Z accelerator experiments of this LDRD project. For these experiments, we simply fed standard Cornell micro B-dot probes radially inward and above the top of the imploding liner such that the probe loops hovered nearly on axis just above the top of the imploding liner [see Figs. 2.1, 3.1, and 3.2(d)]. The micro B-dots probes were oriented such that the $B_z(t)$ field was normal to the loop plane [see Fig. 3.2(d)]. In this way, we could measure $B_z(t)$, but only in the fringe field region above the top of the imploding liner. At first glance, this seems like a good way to measure $B_z(t)$. For example, the probe does not perturb the liner implosion. However, above the imploding liner, even in a ideal cylindrical implosion, the B_z fringe field falls of approximately as $1/(\Delta z)^3$, where Δz is the distance from the top of the imploding liner to the position of the micro B-dot loop (see Fig. 2.1). This means that, even in an ideal cylindrical geometry, there is a large uncertainty in estimating $B_z(t)$ down inside of an imploding liner based on measurements made Δz above the liner. In practice, this uncertainty is large even when Δz is kept very small and well characterized.

To better understand how $B_z(t)$ a distance Δz above the liner relates to $B_z(t)$ down inside the

liner, a simple field solver was implemented in SAMM [53]. In order to generate a field solution, the axial distribution of the azimuthal current density along the liner's inner surface, $J_\theta(z)$, first had to be found such that flux is conserved and $B_r(t) = 0$ everywhere along the liner's inner surface. To find $J_\theta(z)$, we followed the prescription laid out in Ref. [70]. With $J_\theta(z,t)$ in hand, the fields $B_r(r,z,t)$ and $B_z(r,z,t)$ can be readily calculated from the Biot-Savart law or, due to the cylindrical symmetry, using elliptical integral solutions for circular current-carrying loops [74]. We implemented both methods and found that the method using the elliptical integral solutions for current loops was far superior in terms of both efficiency and numerical accuracy. This field solver was used to generate the plots shown in Fig. 2.1, for example.

Prior to an experiment on Z, we would use this field solver to rapidly evaluate the expected voltage responses from micro B-dot probes with given loop areas placed at given heights above the top of the imploding liner. This helped us to set the dynamic range on digitizing oscilloscopes prior to an experiment and also to understand the recorded signal histories after an experiment.

In Fig. 3.3, we present an example of how we used this tool to better understand the response of the probes over the course of an implosion as well as how the measured signals relate to the flux compressed $B_z(t)$ down inside the imploding liner. As can be seen from Fig. 3.3, one benefit of placing the probes above the imploding liner is that the field strength is much lower, due to the $1/(\Delta z)^3$ fall off in the fringing field region. This drastically reduces the induced voltage in the micro B-dot probes, making it very unlikely that the induced voltage would exceed the 1-kV threshold of the semi-rigid coaxial cable.

The simple field solver tool also helped us to understand the characteristic waveform shape that we should expect from a flux compression fringe field measurement (second plot from the top in Fig. 3.3). This waveform can be explained as follows. Early in the implosion, due to flux compression, $B_z(t)$ begins to increase at the location of the probe, thereby increasing the total flux penetrating the loop of the probe, and thus the voltage response is in the positive direction. As the implosion advances to a substantial convergence ratio (i.e., $C_R \approx 5$), the ratio h/R (the ratio of the liner length to the liner radius) increases significantly. The large h/R ratio causes the dynamic fringing field above the top of the liner to fan out in the radial direction more rapidly as a function of z. Thus, the total flux linking the B-dot loop begins to decrease, causing the voltage to swing negative. This negative swing is more rapid than the initial positive swing because the implosion advances/accelerates more rapidly later in the implosion, when C_R and h/R begin to increase much more rapidly and nonlinearly. This negative swing continuous until the liner bounces at stagnation. After bounce, the liner radius begins to increase again, thus reversing the fringe field fan-out process and increasing the flux linking the B-dot loop; therefore, the voltage swings rapidly positive.

We also used the simple field solver to quickly assess how uncertainties in the probes' axial positioning could affect the voltage responses (second plot from the top in Fig. 3.3). Figure 3.3 demonstrates the overall difficulty of using this method to assess $B_z(t)$ down inside the imploding liner, especially at high convergence ratios.

In general, when fielding single-ended micro B-dot probes on Z, we prefer to field two probes of opposite polarity (of opposite loop winding direction) in nearly the same location. We then

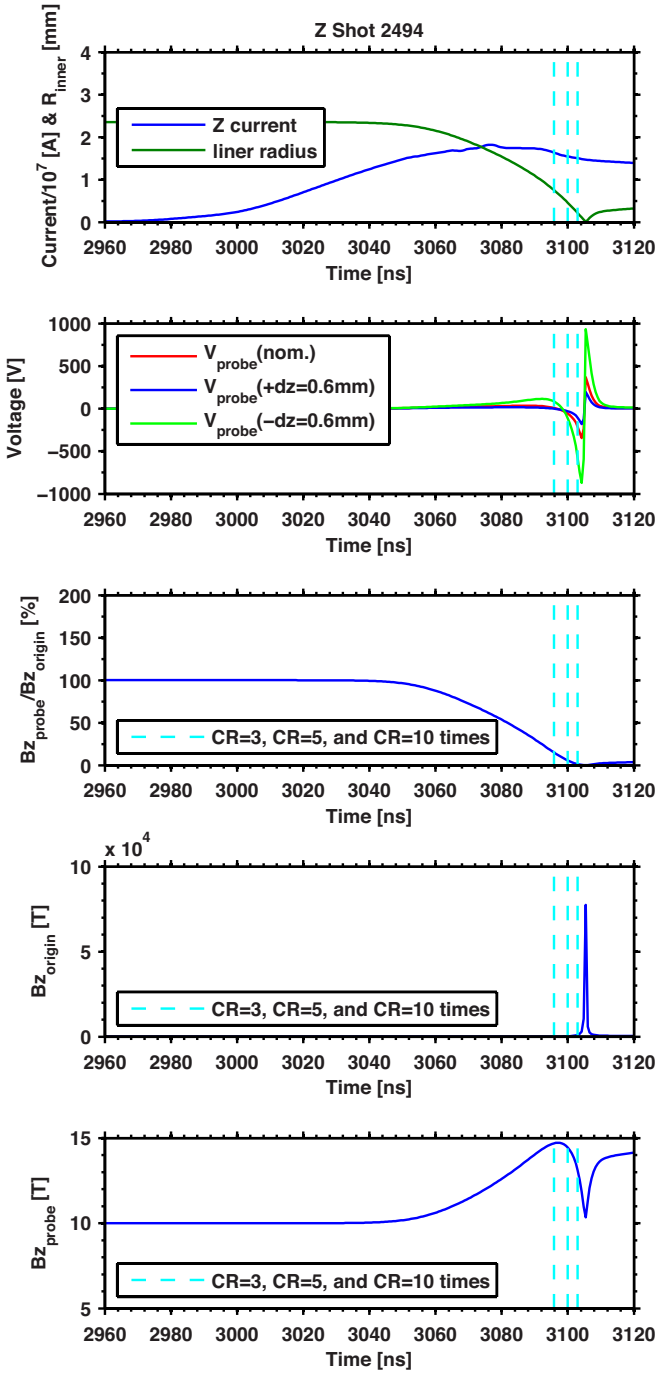

Figure 3.3: An example of using the simple field solver tool, coupled to the SAMM code, that was developed to understand fringe field micro B-dot voltage responses as well as how these voltage responses relate to the flux compressed $B_z(t)$ field down inside the heart (origin) of the imploding liner. The dashed vertical lines indicate the times when convergence ratios of interest occur, i.e., when C_R = 3, 5, and 10 occur. The second plot from the top shows how we used this tool to quickly assess how uncertainties in the probes axial positioning could affect the voltage responses. This figure demonstrates the overall difficulty of using this method to assess $B_z(t)$ down inside the imploding liner, especially at high convergence ratios.

average the two signals together in post-processing (after multiplying the negative probe's signal by -1). In this way, we can hope to reduce the common-mode noise of our measurement. Two probes of opposite polarity that measure the same field in the same location form a differential pair.

When fielding fringe-field micro B-dot probes above the top of an imploding liner on Z, we reduce the risk of all our probes being destroyed by an axially propagating implosion instability and/or pressure wave by fielding two differential pairs simultaneously at two slightly different heights. Two differential pairs means that, in total, we field four micro B-dot probes per shot (see top-down view in Fig. 3.1). To obtain a better signal to noise ratio, we field one pair at a lower but riskier height. To reduce the risk of losing both pairs to an implosion instability, we field the second pair at a slightly elevated height (which of course reduces the signal to noise ratio as well). Typical standoff heights are $\Delta z = 1$–3 mm from the top of the imploding liner to the location of the probes.

3.1.2 Streaked visible spectroscopy (SVS): SVS for measuring Zeeman-split absorption features and inferring the associated flux-compressed magnetic field on Z

For this LDRD project, the Z facility's streaked visible spectroscopy (SVS) diagnostic was used to look for Zeeman splitting in neutral sodium (Na) absorption lines near 5890 Å (a doublet).[1] The development of this technique for Na absorption is described in detail in Ref. [75]. The amount of Zeeman splitting gives a measure of the magnetic field strength in regions where the background continuum is being absorbed. For our flux compression experiments, sodium chloride (NaCl) was deposited on the liner's inner surface by applying a salt water solution to the liner's inner surface and then allowing the water to evaporate, leaving behind the deposited NaCl. All of our experiments used liners with low initial aspect ratios (i.e., $A_{R0} = 6$); thus, with the Z accelerator in short pulse mode (i.e., 0–20 MA in 100 ns), a shockwave is driven radially inward through the liner's wall prior to the liner's inner surface ever moving (this shockwave phenomenon is demonstrated experimentally in Ref. [8]). When this shockwave reaches the liner's inner surface, it breaks out into the liner's initially vacuum filled interior, distributing a very low density plasma throughout the interior volume of the liner. This low density plasma carries with it the NaCl that was deposited along the liner's inner surface. This low density plasma also sources the background continuum needed for the Zeeman absorption spectroscopy measurement. The light (consisting of the continuum with the absorption features) is then collected using two fibers mounted in the top end cap (see Fig. 3.1).[2]

The fact that this measurement is based on a neutral line (at least in this particular implementation of the technique) is one of the fundamental limitations of this measurement. This is because

[1] Later in this LDRD, we searched unsuccessfully for Barium (Ba) lines near 4554, 4934, and 6150 Å.

[2] On Z shots 2493, 2494, and 2537, we fielded a lens-coupled SVS setup, where the lens was mounted below the target and was attached to a fixture that connected to the Z accelerator's lower magnetically-insulated transmission line. An illustration of this setup is provide in Appendix A. This system collected too much background light to be useful. This background light was probably emitted from the double post-hole convolute structure on Z. For this reason, we switched to the target-mounted fiber optic setup shown in Fig. 3.1.

the neutral Na population quickly diminishes as the Na is easily ionized in these experiments. Finding absorption (or emission) lines from higher ionization states, perhaps even from materials other than Na [e.g., Barium (Ba) lines near 4554, 4934, and 6150 Å], could in principle extend this technique's applicability.

3.1.3 Faraday rotation: A fiber-based Faraday rotation diagnostic for directly measuring flux-compressed magnetic fields inside of an imploding liner on Z

The Faraday effect is a magneto-optical phenomenon that causes the plane of polarization of linearly polarized light to rotate by an amount that is proportional to the magnetic field strength in the direction of the light's propagation when the light's propagation is in a birefringent medium. In plasma physics, this medium can be the plasma itself; however, to use the plasma itself as the medium to diagnose the magnetic field embedded in the plasma requires knowledge of the plasma's density, length, and uniformity [76]. Knowing all of these plasma conditions simultaneously can be exceedingly challenging. Thus, an alternative method is to use a fiber-based Faraday rotation technique.

The fiber-based Faraday rotation technique is illustrated in Fig. 3.4. Here, **E** is the electric field vector of the linearly polarized light. This light is propagating parallel to the direction of a strong quasi-static background magnetic field **B**, which one would like to diagnose. By placing a uniform, well-ordered, birefringent medium (e.g., magneto-optical fiber) with a known length d along the light's propagation path, the plane of polarization can be rotated by an angle β. The degree of rotation through this magneto-optical fiber is quantified by a Verdet constant $\mathscr{V}$, where

$$\beta = \mathscr{V} B d \tag{3.3}$$

is the governing equation. This approach has been used to measure magnetic fields of up to 1100 T in experiments using multi-microsecond explosive flux compression generators [60].

To pursue the development of a fiber-based Faraday rotation diagnostic for use at the Z facility, a collaboration was initiated between Center 1600 at Sandia and the P-24 Plasma Physics group at Los Alamos National Laboratory. The initial design work and bench testing of the design were conducted at Los Alamos and later presented at the Diagnostics User Group Meeting held at Lawrence Livermore National Laboratory on May 21–23, 2013.

The basic concept of the Faraday rotation probe is illustrated in Fig. 3.5(a). The concept makes use of a 3-mm-long terbium (Tb) doped fiber and a dielectric reflecting mirror. This 3-mm-long Tb-doped region is the only region in the fiberoptic system that is substantially magneto-active. The light passes through this region twice due to the dielectric mirror. The double pass through this region doubles the rotation angle (i.e., it does not reverse the rotation). The 3-mm length of this region is sufficiently long to provide a good signal to noise ratio (i.e., a healthy rotation angle that is easily resolvable) by sampling a reasonable length of a presumably uniform magnetic field. The 3-mm length is sufficiently short to avoid sampling the magnetic field near the ends of the liner,

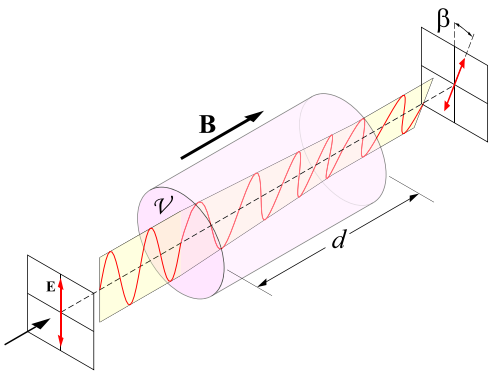

Figure 3.4: Illustration of the Faraday Effect [77]. Here, **E** is the electric field vector of the linearly polarized light and **B** is the magnetic field that one would like to diagnose. The plane of polarization is rotated by an angle β after the light propagates a distance d through the cylindrical magneto-optical fiber with Verdet constant $\mathscr{V}$.

where end-effect implosion instabilities (*cf.* Sec. 3.2) could lead to nonuniformity in the magnetic field. Some photographs of the design's components and their testing at Los Alamos are presented in Figs. 3.5(b)–3.5(d). These components were then brought to Sandia and integrated into the Z facility. The first Z shot conducted with this new diagnostic was Z shot 2592, which was taken on December 12, 2013.

The Faraday rotation diagnostic system was constructed using commercial off-the-shelf telecommunication fiber components. Polarization maintaining (PM) fiber was used to avoid the drift and unpredictable polarization states that can occur when using single mode (SM) fiber in the presence of vibrations, curvature of the fiber, or small movements. Angle polished, keyed FC/APC connectors were used throughout the system to reduce back reflections. Narrow keys were specified to reduce incompatibility issues with other fiber connectors. We used Panda type PM fiber for patch cords between components. This has a single mode core diameter of 9 μm, a cladding diameter of 125 μm, and a buffer diameter of 250 μm. At telecommunications wavelengths ($\lambda = 1550$ nm), these components are readily available and fairly inexpensive. We used an IPG 2-W diode laser which required attenuation down to 100 mW. The attenuated laser output was nominally polarized and required some conditioning to stabilize the polarization.

Figure 3.6 shows a schematic of the light path. For this setup, the laser was coupled to a free space polarization discriminator (of thin film type) to reduce the drift of the polarization state of the laser and the attenuator. The measured extinction ratio was on the order of 20 dB. This moderately pure polarization state was passed through a polarization rotator consisting of a half wave plate and a quarter wave plate. This allowed for easy characterization of the system behavior with either S or P polarizations, or some combination of both, as input light signals. (Note that fully deterministic polarization control is available in all-fiber-based solutions from suppliers like Thorlabs, but these all-fiber-based solutions are more expensive than the free-space solution implemented for this LDRD project.) The free space to fiber coupler was a Thorlabs fiber bench with aspheric fiber port optics (PAF-X-11-C, NA=0.22, focal length = 11 mm, mode field diameter = 10 μm) that allows 5 degrees of freedom for position and orientation. A fiber Polarization Maintaining Optical Circulator (Agiltron OCPM-30C11A133, 1550 nm) was used as a directional coupler to pass the

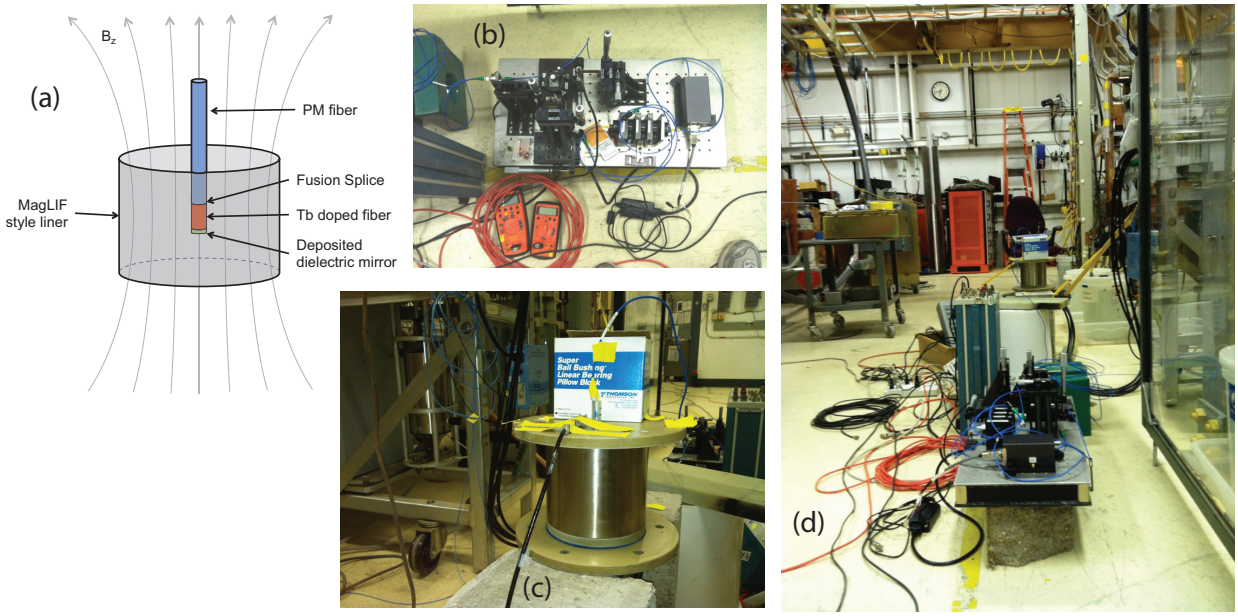

Figure 3.5: (a) Conceptual illustration of the Tb-doped Faraday rotation probe. (c)–(d) Photographs of the bench testing conducted at Los Alamos National Laboratory. (b) The optical board with various components. (c) The solenoid coil that the Tb-doped magneto-optical fiber and a reference B-dot probe were placed inside of for testing and calibration. (d) The overall testing and calibration setup.

selected S polarization in the forward direction only (i.e., from port 1 to port 2). This part has its key aligned to the slow axis and only works for slow axis polarization. The light injected into port 1 is shunted to port 2 and thus to a polarization splitter/combiner. The polarization splitter/combiner receives the light on its slow axis port and then passes this light through to its combiner port. The combiner port can pass either S or P polarization, and it is connected to a 200-cm-long section of PM fiber. Through this PM fiber, the S-polarized light is sent to the Faraday probe inside of the imploding liner. Here, the light makes a first pass through the Tb-doped magneto-optic region of the probe, then reflects off of the dielectric mirror, and then makes a second pass through the Tb-doped region. The reflected and doubly-rotated light then returns back to the combiner port of the combiner/splitter component. Upon receiving the reflected and Faraday rotated light, the combiner port sends the S polarization back to the circulator. The circulator then sends the S-polarized light from port 2 to port 3 and onwards to a photodetector ($\parallel$ PD). Simultaneously, the combiner port on the splitter/combiner sends the P polarization directly to a photodetector ($\perp$ PD).

The Faraday active material is a 3-mm-long section of Tb doped fiber (65% Tb by weight). This Tb doped section is fusion spliced to the end of the PM fiber. AdValue Photonics furnished the Tb doped fiber and performed the fusion splicing. The Tb doped fiber is difficult to splice and requires considerable experience to get a good result. The fusion splice requires a programmed and precisely controlled time and heat profile. Substantial information can be found in the PhD thesis and papers of L. Sun [78–81].

The free end of the Tb dobed fiber had a dielectric mirror applied by Lattice Electro Optics at their coatings facility in Fullerton, California. The mirror reflectivity is $\mathscr{R} > 50\%$ at $\lambda = 1550$ nm

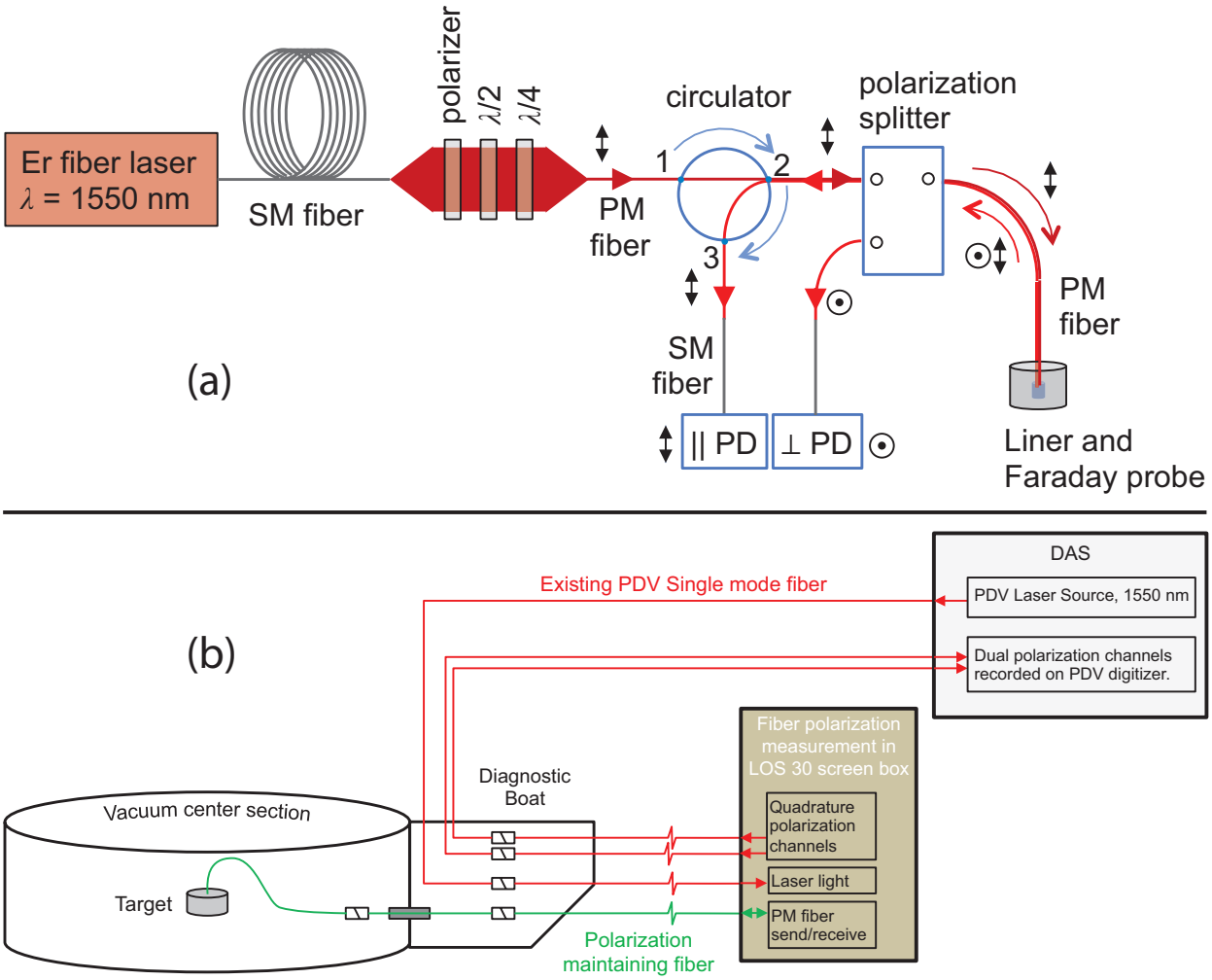

Figure 3.6: (a) Schematic of the Faraday rotation diagnostic system. (b) Schematic of the Faraday rotation diagnostic system integrated into the Z facility.

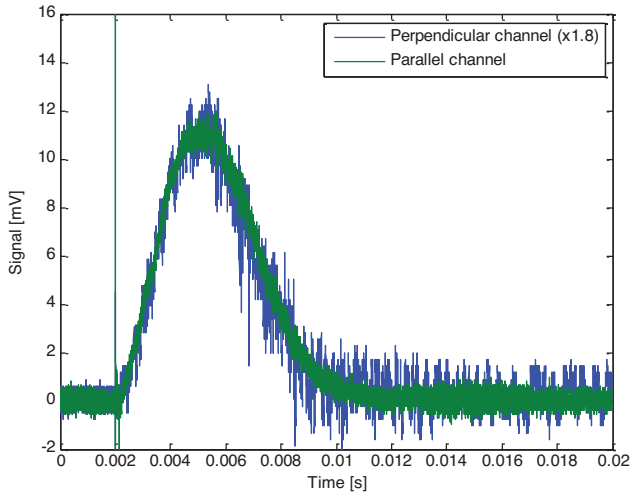

Figure 3.7: Faraday probe calibration data taken at the Systems Integration Test Facility (SITF) at Sandia National Laboratories.

and $\mathscr{R} > 20\%$ at $\lambda = 632$ nm. The reason we used a dielectric mirror instead of a metal coating is because of our application's large dB_z/dt induced voltages. These large voltages would drive large eddy currents in a metallic mirror because of the high electrical conductivity of metal. These large eddy currents would generate sufficient ohmic heating to vaporize the mirror.

The first probes acquired for this LDRD project were initially tested and calibrated at Los Alamos National Laboratory. These probes, as well as subsequent probes acquired by Sandia, were later calibrated at the Systems Integration Test Facility (SITF) in the medium bay of building 970 at Sandia. Figure 3.7 shows the results of cross calibrating the two polarization channels.

When fielding the Faraday diagnostic on Z, we needed to ensure that the diagnostic's recording instrumentation would be fast enough to resolve the polarization oscillations. To this end, SAMM simulations were run to better understand how fast the polarization would be oscillating as a function of time, liner convergence, and flux compressed magnetic field strength. Results from an example of this exercise are shown in Fig. 3.8. To record the fastest oscillating signals expected, while simultaneously being able to record the entire 3-ms-long ABZ pulse on the same record [for an *in situ* Faraday probe calibration using the ABZ supplied $B_z(0)$ as a reference field], we utilized the fast digitizing oscilloscope of the Photon Doppler Velocimetry (PDV) diagnostic system at the Z facility, which is maintained by the Dynamic Material Properties (DMP) research group at Sandia (Organization 1646).

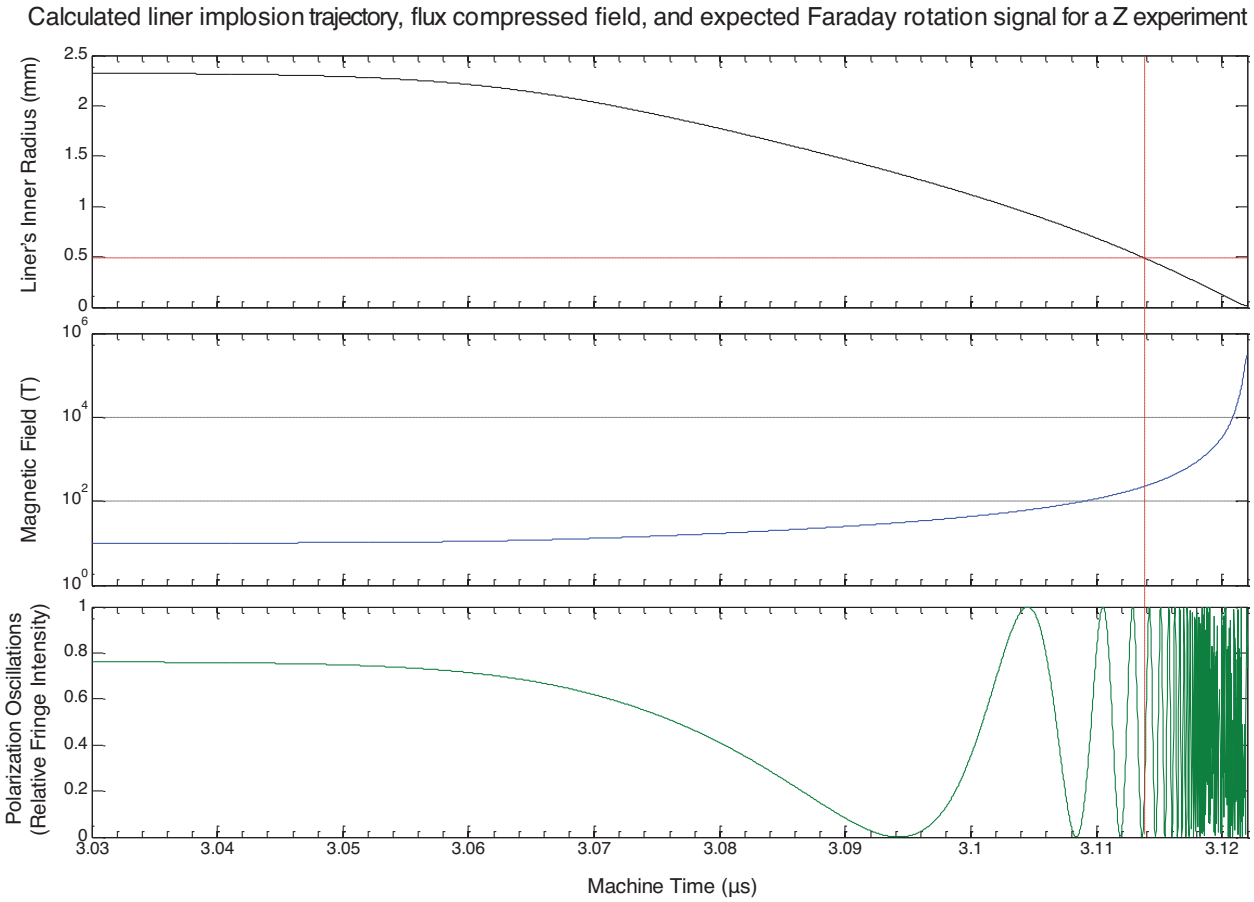

Figure 3.8: Results from a SAMM simulation to better understand how fast the polarization would be oscillating as a function of time, liner convergence, and flux compressed magnetic field strength. The horizontal red line indicates the outer radius of the Faraday probe and the vertical red lines indicate the time when the liner's inner surface first impacts the Faraday probe.

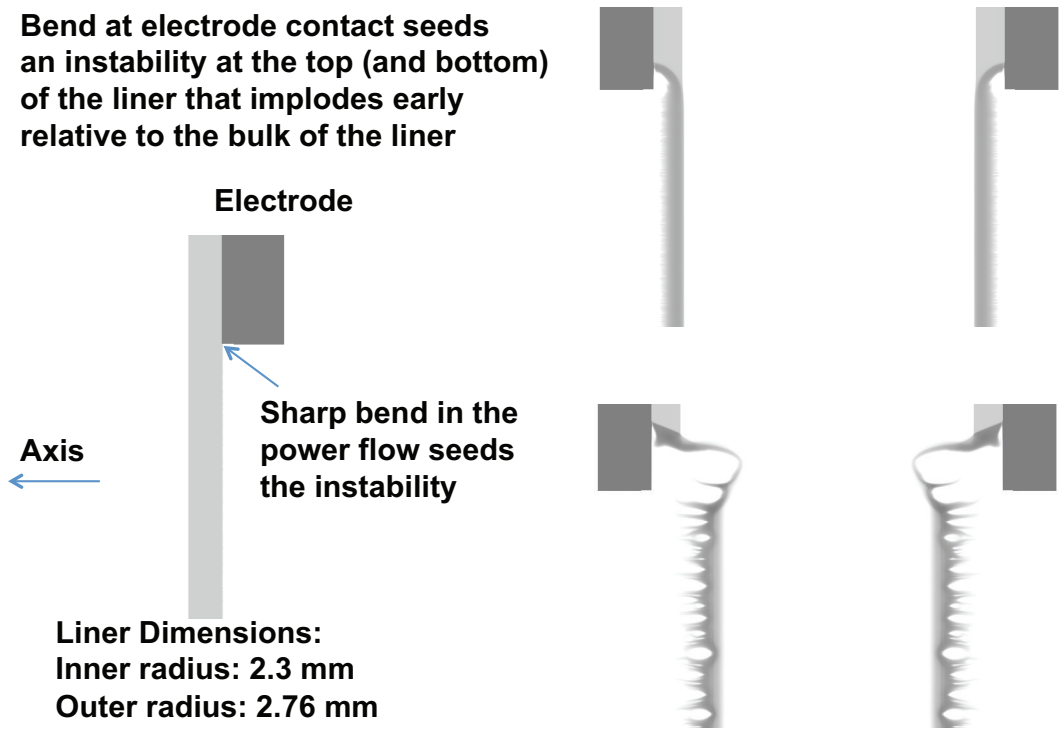

Figure 3.9: GORGON 2D simulation results illustrating an end-effect instability.

3.2 Liner implosion design work to improve implosion stability and thus improve compatibility for probe measurements of magnetic flux compression

All of the previously mentioned efforts to relate micro B-dot fringe field responses measured above the liners to $B_z(t)$ down inside the imploding liners assumed an ideal cylindrical geometry. However, liners do not have ideal cylindrical geometries as they implode, especially near the tops and bottoms of the liners. This is because of various end-effect instabilities (e.g., the "wall instability"). End-effect instabilities were first identified as potentially problematic for MagLIF liners in Ref. [8], though others had previously observed them [82, 83] and developed mitigation strategies such as conical electrode surfaces (referred to as "glide planes") [84–86].

In Fig. 3.9, we present simulation results to illustrate an end-effect instability. These simulations used the GORGON radiation magnetohydrodynamics code [87]. Note that this instability expands radially inward as well as axially upward from the upper corner formed by the joint between the outer surface of the liner and the bottom surface of the top electrode (which is the anode surface of the Z accelerator). Thus a certain amount of vertical standoff from the top of the liner to the position of the micro B-dot probe is required in order for the micro B-dot to survive the implosion and make the desired measurement.

In an attempt to keep the imploding flux-compressing liner as ideally cylindrical as possible,

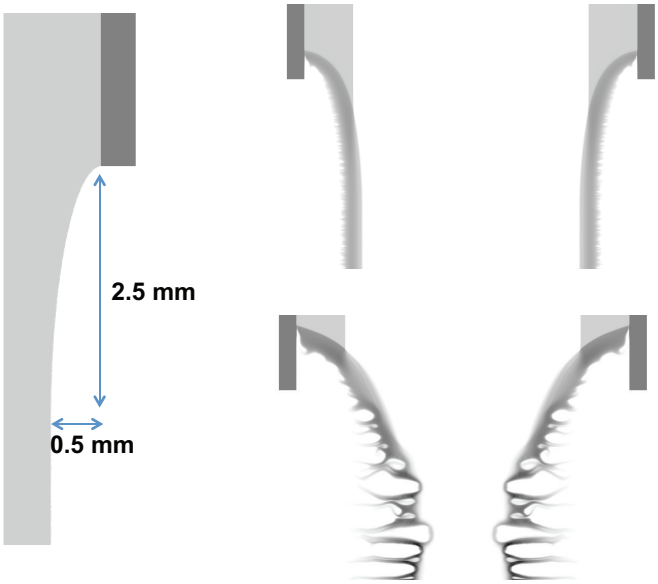

Figure 3.10: GORGON 2D simulation of a "thick-end" design for mitigating end-effect instabilities. This design looked at the effects of thickening the ends of the liner. This design could work, but would require a large Δz between the approximately cylindrical region of the implosion and the undisturbed region far above the liner where one might consider placing a probe.

while simultaneously minimizing the Δz necessary to keep the probes safely above end-effect instabilities, much design work was done using the GORGON code in both 2D and 3D. This design work was challenged by the fact that we wanted to keep the top of the liner's interior as open as possible to enable the micro B-dot fringe field measurements. That is, in order to make the fringe field measurements, either vacuum or dielectric must be used in order to allow the field lines to move into the region where the probe loops reside; if metal is used instead of vacuum or dielectric, then the the field lines will be line-tied (frozen-in) to the top electrode, and thus the fringe field probes will not detect any changes to the field above the imploding liner. This requirement essentially ruled out the use of metallic glide planes and forced us to consider other mitigation strategies.

In Fig. 3.10, we present one approach to mitigating end-effect instabilities. This approach uses thicker/tapered liner walls near the ends of the liner to hold back the instability. This strategy works reasonably well as long as the radius of curvature is large enough (i.e., a very gradual thickening). The problem with this approach is that the axial distance between the approximately cylindrical portion of the implosion and the undisturbed region above the implosion (where one might consider putting a probe) is quite large; thus, Δz would be quite large.

In Fig. 3.11, we present another approach to mitigating end-effect instabilities. This design uses the higher density aluminum "cushion" to hold back the instability as the instability breaks through the lower density beryllium liner. This is the design that we ultimately chose for some of our first flux compression experiments on the Z accelerator (shots 2494 and 2537). It is important to note that the "cushion" design, which was developed under this LDRD project, was later incorporated into the target design of our fully-integrated MagLIF experiments [16, 18]. Thus, the

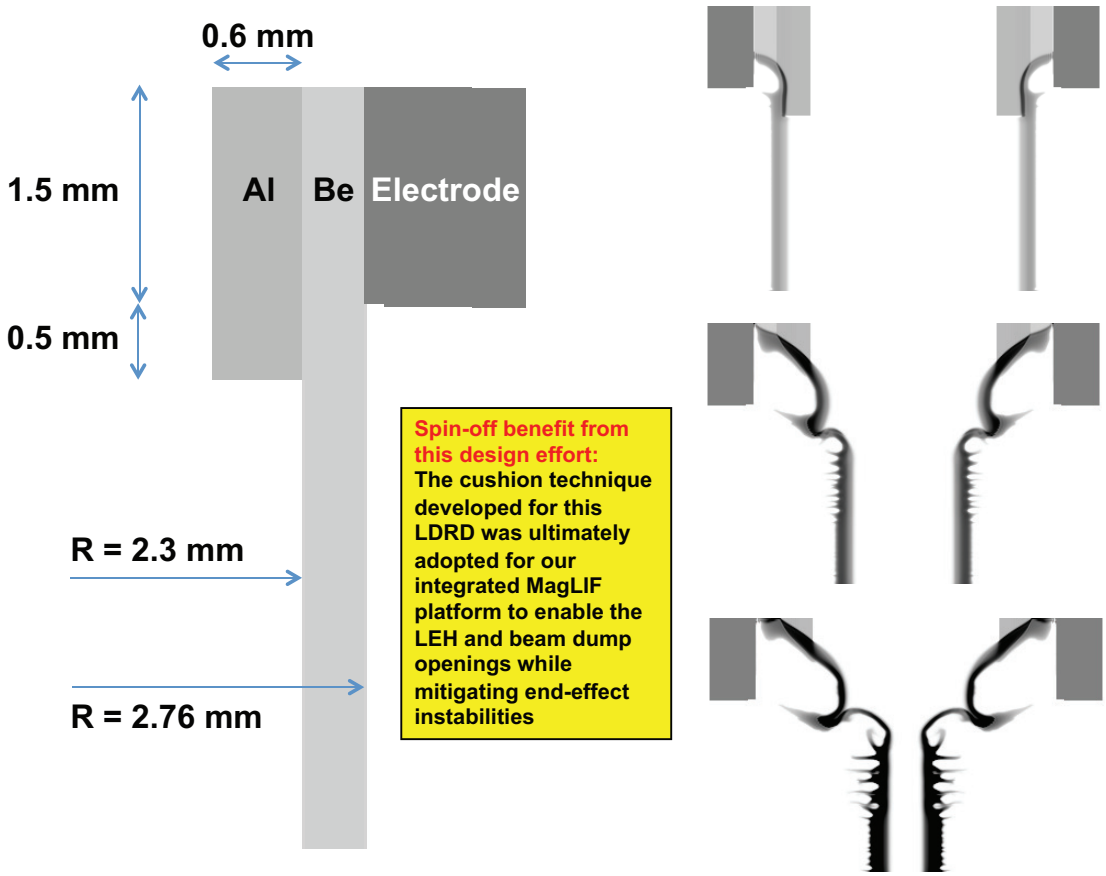

Figure 3.11: GORGON 2D simulation of a "cushion" design for mitigating end-effect instabilities. This design uses the higher density aluminum (Al) "cushion" to hold back the instability as the instability breaks through the lower density beryllium (Be) liner. This is the design that we ultimately chose for some of our first flux compression experiments on the Z accelerator (shots 2494 and 2537).

cushion development represents a spinoff benefit from this LDRD project, which is due to all the liner dynamics studies that went into designing, executing, and analyzing these flux compression experiments.

Another design option that was investigated early on in this project was to use a very much over-massed liner, such that the liner would implode well after peak current. Here, a very large liner [$R_{outer}(0) = 5.2$ mm] with a very low initial aspect ratio ($A_{R0} \equiv R_{outer}(0)/[R_{outer}(0) - R_{inner}(0)] = 5.2$) was used. The idea here is that you use the fast Z pulse to impart some momentum into the liner and then let it coast into stagnation. The reason for doing this is to preserve the ideal cylindrical geometry by using a very thick and robust liner while also avoiding driving instability growth while the liner moves inward. An example of the design work done for this (in this case using the ALEGRA radiation-magnetohydrodynamics code [88, 89]) is presented in Fig. 3.12.

During the experiment where this liner was fielded (Z shot 2493), the micro B-dot probes failed prior to the start of the implosion. At the time of the experiment, this failure was a mystery, so we ceased using this target in future experiments. However, with what we know now, it could very well be that the shock launched in the top electrode, which propagates upward, could have destroyed

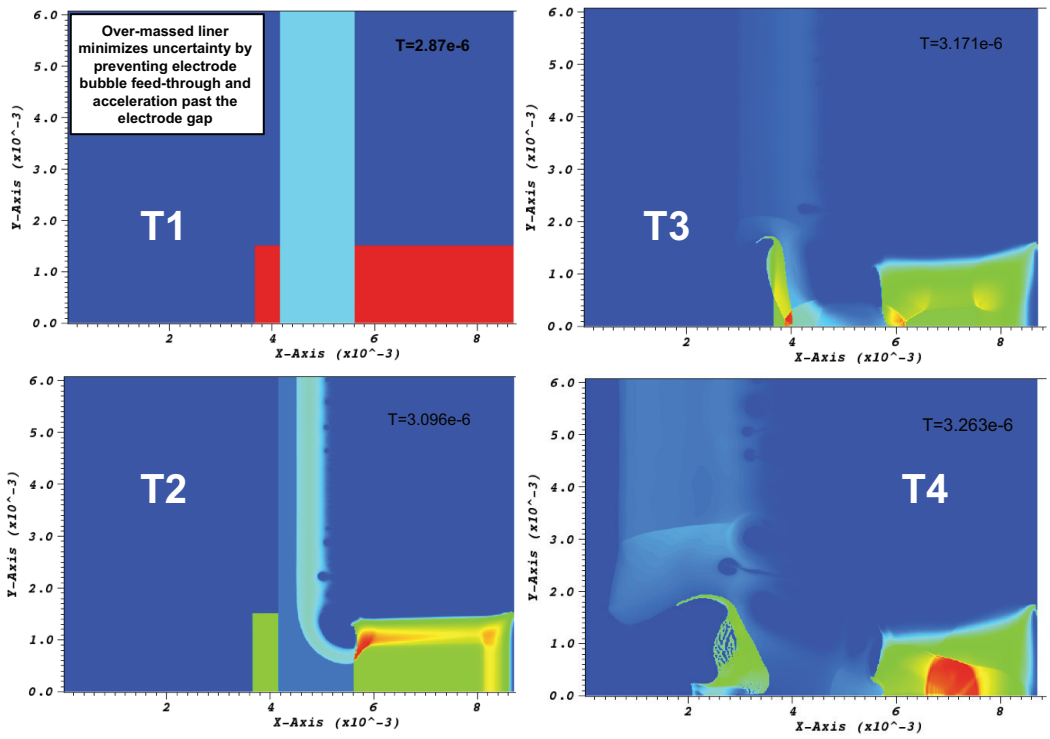

Figure 3.12: ALEGRA 2D simulation of a liner design that was intentionally "over-massed" to preserve an ideal cylindrical geometry during the implosion. This liner was designed to coast to the cylindrical axis of symmetry after having some momentum imparted to it during the fast Z pulse. The lack of drive pressure during the implosion preserves the cylindrical geometry by avoiding driving instabilities like end-effect instabilities. This design was tested on Z shot 2493.

the probes well before any significant motion of the highly over-massed liner commenced.

Despite the premature loss of the micro B-dot probes on shot 2493, we did obtain two nice radiographs of the implosion, which did appear to be stable. Another success for this shot was that this was the first time that we applied a thin (85-nm thick) platinum (Pt) coating to the liner's inner surface. This was done using atomic layer deposition, and we did this to enhance the imaging contrast of the liner's inner surface in the radiographs.

The Pt layer that was deposited for radiographic contrast enhancement worked very well on shot 2493, and thus this development represents another spinoff benefit from this LDRD project, which is again due to all the liner dynamics studies that went into designing, executing, and analyzing these experiments. For more details on this and other shots, including the radiography results, see the post-shot reports archived on the MagLIF SharePoint cite [71].

3.3 Early experimental results

3.3.1 Micro B-dot measurements on Z shot 2537

Our first shot that recorded unambiguous data from micro B-dot probes fielded above the top of a flux compressing liner was shot 2537. In Fig. 3.13, we present a description of the liner target as well as the data that was recorded by the upper differential pair. In the target description illustration, at least one of the micro B-dot probes from both the upper and lower pairs can be seen. From the voltage data plotted, it is clear that the waveforms from the experiment do not agree with the simple vacuum solenoid field solution from the SAMM simulation. Post-shot GORGON simulations suggest that the signals don't agree with the vacuum solenoid field solution because a plasma jet forms on axis, which advects B_z into the probe region continuously and rapidly, thus giving a continuously increasing voltage.[3] These results nevertheless showed that we could cleanly measure an increase in $B_z(t)$ from 10 T to >30 T above the top of an imploding liner on Z; the voltages associated with this rise are more than sufficient to measure the fringe fields associated with magnetic flux compression throughout the implosion, as long as we could remove the contaminating signal caused by the low-density plasma jet on axis.

To remove the possibility of an on-axis jet interacting with the micro B-dot probes, we stopped using open cushion configurations; instead, we switched to completely filled nylon end caps (see Fig. 3.1), which simultaneously served as instability cushions.[4] GORGON design simulations

[3] At one point, there was a competing hypothesis that perhaps the metallic load hardware surrounding the imploding liner was affecting the dynamic fields that the micro B-dots were sensitive to. GORGON simulations were then run to test the effect of the load hardware on the dynamic fields. The results, presented in Appendix B, confirmed that the load hardware was likely not the culprit for the anonymously large fringe field signals presented in Fig. 3.13.

[4] We note here that another target design consisted of a liner completely filled with nylon. The idea was to remove any ambiguity caused by low density plasmas injected into the liner's interior by completely filling it with solid, low-density dielectric. The low mass of the nylon fill would allow the liner to implode fairly unimpeded. Unfortunately, this target broke during assembly and thus was never tested. Nevertheless, this target could have been successful and therefore we document it in Appendix C.

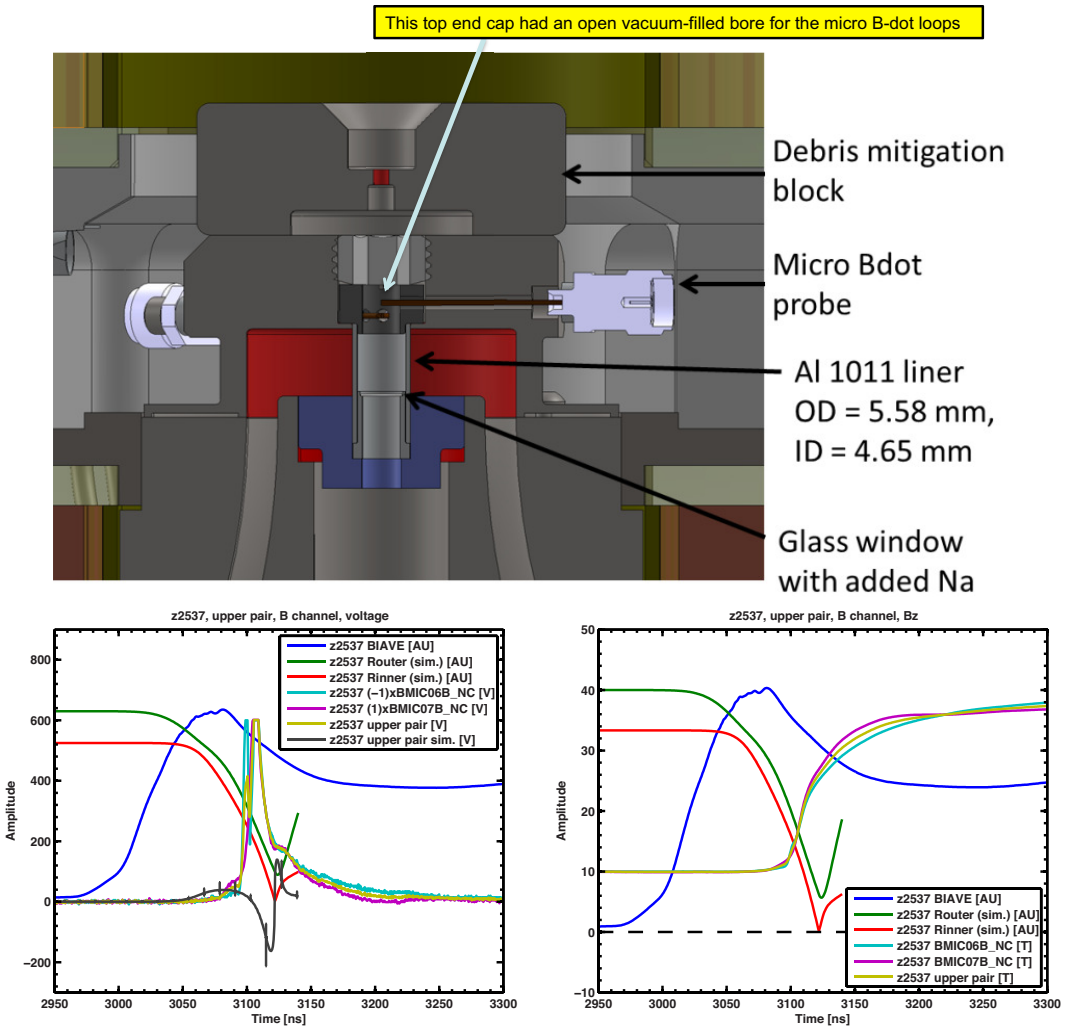

Figure 3.13: A description of the target for Z shot 2537 and the resulting micro B-dot probe data. The peak of the voltage and the shape of the voltage waveform were much different than what was expected based on the simple solenoidal field solution in the SAMM calculation. Post-shot GORGON simulations suggest that the signals don't agree with the vacuum solenoid field solution because a plasma jet forms on axis, which advects B_z into the probe region rapidly.

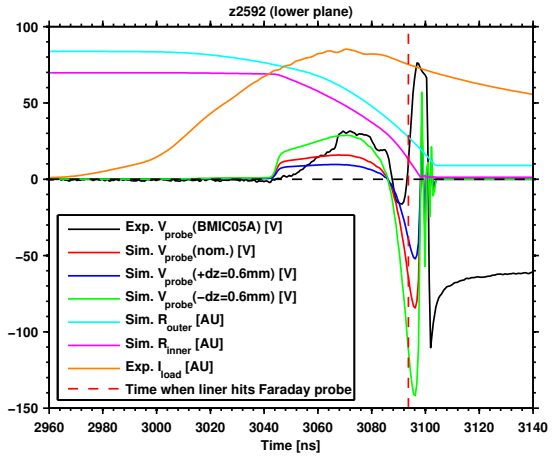

Figure 3.14: The single-ended voltage from one of the two micro B-dot probes of the lower differential pair on Z shot 2592 (its differential pair partner failed early in the shot). Here the waveform looks much more like what is expected from the simple solenoidal field solver tool (in contrast to the micro B-dot data shown in Fig. 3.13 for shot 2537, where the experimental data did not look like what was expected from the solenoidal field solver tool). We believe that the better agreement here for shot 2592 is because the on-axis Faraday probe and the filled dielectric end cap eliminated the possibility of an on-axis plasma jet interacting with the micro B-dot probes. Also note that the experimental voltage waveform swings positive due to bounce sooner than in the simulation. However, this is likely because the liner bounces sooner in the experiment due to hitting the on-axis Faraday probe. The presence of the Faraday probe was not accounted for in the simulation.

suggested that the radially continuous nylon fill would be of sufficient inertial mass to hold back the end-effect instabilities. The timing for the decision to switch to filled nylon end caps/cushions was fortuitous, because after shot 2537, the fiber-based Faraday rotation probe became available for use on Z, but required a target-mounted fixture to hold the probe in place on axis within the liner target; the filled nylon end caps served this purpose well.

3.3.2 Micro B-dot measurements on Z shot 2592

Our first test of the platform shown in Fig. 3.1 was Z shot 2592. On this shot, many of the micro B-dot probes failed; however, one single-ended probe from the lower differential pair survived (its differential pair partner was one of the probes that failed). The signal recorded by this probe is shown in Fig. 3.14. Here we see a waveform that looks much more like what is expected from the simple field solver tool. We believe that the better agreement is because the on-axis Faraday probe and the filled dielectric end cap eliminated the possibility of an on-axis plasma jet interacting with the probes. Note that, late in the implosion, after the negative voltage spike, the experimental voltage waveform swings positive due to bounce sooner than in the simulation. However, this is likely because the liner bounces sooner in the experiment due to hitting the on-axis Faraday probe. The presence of the Faraday probe was not accounted for in the simulation.

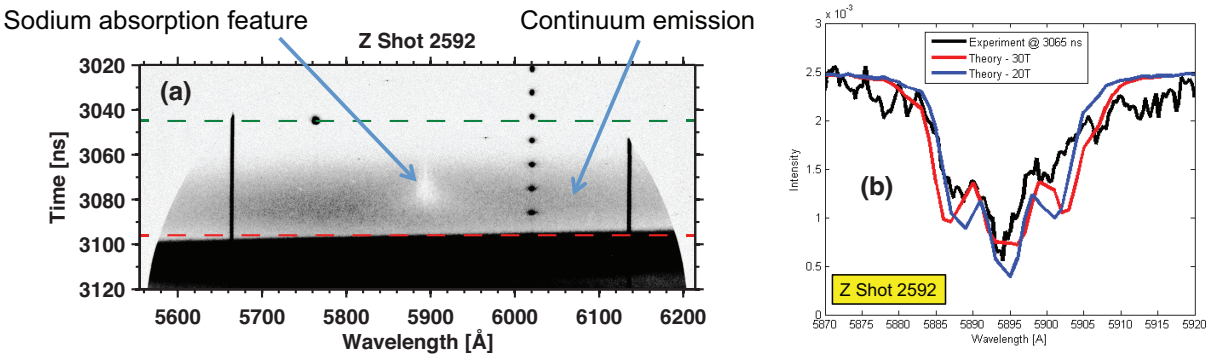

Figure 3.15: Streaked visible spectroscopy (SVS) data collected on Z shot 2592. (a) The streaked image. The green dashed line is the time of shock breakout from the liner wall. The red dashed line is the time when the liner hits the Faraday rotation probe. (b) A lineout through the streaked image at $t = 3065$ ns and simulated lineouts for $B_z = 20$ T and 30 T. The agreement between the simulated and experimental lineouts indicates that the flux compressed B_z field in the experiment was in the range of 20–30 T at $t = 3065$ ns.

3.3.3 SVS measurements on Z shot 2592

On Z shot 2592, we obtained good SVS data from the two light collecting fibers mounted in the top end cap of the liner target (see Fig. 3.1).[5] Here, the SVS diagnostic was configured to look for Zeeman splitting in neutral sodium (Na) absorption lines near 5890 Å (a doublet). The results of this measurement are presented in Fig. 3.15. In the streaked image [Fig. 3.15(a)], a white bell-shaped feature is present; this is the sodium absorption feature. One can also see the dark continuum source that appears shortly after the liner shockwave breaks out from the liner's inner surface and enables the absorption measurement. Later, when the liner hits the Faraday rotation probe, a very dark continuum is observed. Well before the liner hits the Faraday probe, the signal from the sodium absorption feature disappears. This is because the absorption feature is due to neutral sodium, and sodium becomes at least partially ionized well before the liner hits the Faraday probe. The fact that this measurement is based on a neutral line (at least in this particular implementation) is one of the fundamental limitations of this measurement. Nevertheless, as can be seen from the decent agreement between the experimental and simulation lineouts plotted in Fig. 3.15(b), this technique was able to measure a flux compressed field of about 20–30 T, where $B_z(0) = 10$ T. Finding absorption (or emission) lines from higher ionization states, perhaps even from materials other than Na [e.g., Barium (Ba) lines near 4554, 4934, and 6150 Å], could in principle extend this technique's applicability.

[5] On Z shots 2493, 2494, and 2537, we fielded a lens-coupled SVS setup, where the lens was mounted below the target and was attached to a fixture that connected to the Z accelerator's lower magnetically-insulated transmission line. An illustration of this setup is provide in Appendix A. This system collected too much background light to be useful. This background light was probably emitted from the double post-hole convolute structure on Z. For this reason, we switched to the target-mounted fiber optic setup shown in Fig. 3.1.

3.3.4 SVS measurements on Z shots 2592, 2653, and 2713

The absorption feature present in the SVS data of Z shot 2592 was originally thought to be due to the Na deposited on the liner's inner surface; however, it was later realized that a significant amount of Na is contained in the glass tube that houses the Faraday rotation fiber, and thus it is possible that the Na absorption feature observed in the streaked image [Fig. 3.15(a)] was due to sodium sourced by this glass tube. To eliminate this possibility, the future Z shots 2653 and 2713 were designed using a glass tube that contained essentially no Na. For these shots, Ba was also deposited on the liner's inner surface. These shots, however, recorded no Na or Ba absorption features. For Z shot 2713, the absence of absorption features is understandable since this experiment was designed for use with the Z accelerator in long pulse mode to enable a larger liner and thus more room for implosion convergence before the liner hit the Faraday probe. It turns out that, with the larger liner and with the Z accelerator in long pulse mode, a shockwave never develops in the liner wall (i.e., this is shockless liner compression [6]), and thus one might not expect the Na or Ba deposited on the liner's inner surface to break away from the liner's inner surface and deposit themselves throughout the liner's interior volume. This long-pulse-driven shockless compression speculation does not, however, explain the absence of Na and Ba absorption features on Z shot 2653. Thus, it could simply be that the source of Na on Z shot 2592 was really from the glass tube that housed the Faraday fiber, rather than from the Na deposited on the liner's inner surface. Unfortunately, this question remains unresolved at this time.

3.3.5 Faraday rotation and other measurements on Z shots 2592 and 2653

Z shot 2592 was the first attempt to measure flux compression directly using the fiber-based Faraday rotation diagnostic. The data return from this shot was inconclusive. During *in situ* pre-shot calibrations using pulses supplied by the ABZ system (i.e., the target was loaded in Z and ABZ was pulsed, but the Z accelerator itself was not pulsed), the signal from the returned laser light got progressively worse on each ABZ pulse. It remains unclear at this time what caused the successive degradation, but the leading hypothesis at this time is that the laser intensity was too high, which essentially "fried" some portion of the magneto-optical region of the probe. On our next attempt, Z shot 2653, the probe was damaged at some point prior to its complete installation into the Z accelerator, as there was no laser light returned upon first attempt. We fired this shot anyway to obtain SVS and micro B-dot data. As mentioned above, the SVS data failed to return an absorption feature. Moreover, the micro B-dot probes returned signals that were confusing and difficult to explain in terms of the expected solenoidal fringe fields; these data remain unexplained.

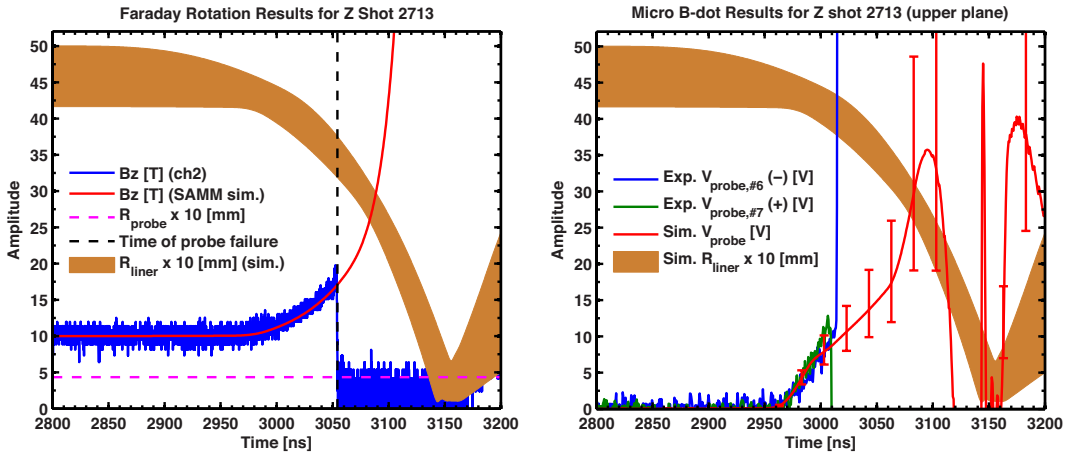

Figure 3.16: Faraday rotation data and fringe-field micro B-dot data obtained on Z shot 2713. SAMM simulation data are shown for comparison and for a timing reference. The single-ended measurements from the two micro B-dot probes that comprise the upper differential pair are shown. The agreement between the two single-ended measurements indicates very little common-mode noise. The error bars shown for the simulated micro B-dot voltage is due to the uncertainty in the axial positioning of the micro B-dot probes above the liner. Note that both of the upper micro B-dot probes fail at about the same time, which is shortly after the lower pair (not shown) failed. Also note that the Faraday rotation measurement failed shortly after the micro B-dot measurements. These relative timings for probe failures provide supporting evidence for the possible failure mechanism described in the text (i.e., an axially-propagating magnetic bubble/pressure wave that first crushes the micro B-dot probes and then races down the micro B-dot feedthrough channels, destroying the on-axis Faraday rotation probe; this failure mechanism will hopefully be eliminated in future experiments using the new design discussed below in Sec. 3.5).

3.4 Latest experimental results: Z shot 2713

3.4.1 Faraday rotation and micro B-dot measurements on Z shot 2713

The first successful shot with the new fiber-based Faraday rotation diagnostic was Z shot 2713. This shot also returned good micro B-dot data that agreed with what would be expected from solenoidal fringe fields. Both the Faraday rotation data and the micro B-dot data are shown in Fig. 3.16. The agreement between the experiment and the SAMM simulation is remarkable for approximately 50 ns; then, suddenly, the signals from both the Faraday diagnostic and the micro B-dot probes are lost. This presented quite a mystery for some time and is still not completely resolved. However, the leading hypothesis for why the probes suddenly failed has to do with the mating between the liner's outer surface and the load hardware electrodes.

The Z shot 2713 target, mounted in the electrode hardware, is shown in Fig. 3.17. The top and bottom nylon end caps are glued into the top and bottom ends of the liner, respectively. The liner target (liner plus end caps) is then slipped into the top electrode (anode) from above. In this case, the top electrode also formed the azimuthally continuous solid aluminum return-current can. This return-current structure was used to enable load current VISAR measurements.

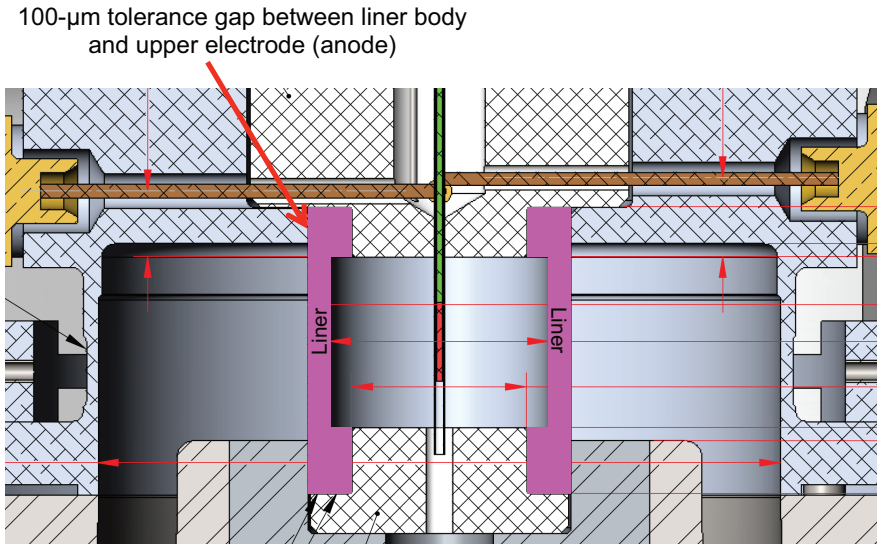

Figure 3.17: The Z shot 2713 liner target mounted in surrounding electrode hardware [anode (top) and cathode (bottom)]. Also shown are two micro B-dot probes (one from each of the differential pair heights fielded above the liner) and the Faraday rotation fiber fielded on axis. The red region of the on-axis Faraday fiber represented the 3-mm-long terbium (Tb) doped magneto-optical region of the probe.

Upon a post-shot investigation of the design, it was found that there existed a joint with a 100-μm tolerance gap between the liner's outer surface and the top electrode (i.e., the electrode that the liner slips into from above when being inserted into the anode return-current structure). This gap likely allowed a magnetic bubble to propagate up into the nylon end-cap material, crushing the micro B-dot cables. Upon reaching the micro B-dot cables, the bubble is then free to propagate down the micro B-dot feed-through channels, crushing the Faraday fiber on axis at a slightly later time. Indeed, looking at the data shown in Fig. 3.16, we find that the micro B-dot probes died slightly before the Faraday rotation probe. Moreover, the micro B-dot signals from the lower differential pair (not shown) were found to have died slightly before the upper pair. Thus, the relative timing of the various probe failures is consistent with this hypothesis. Additionally, post-shot simulations using the ALEGRA code to model the effect of this tolerance gap have indeed found that this gap could contribute to the premature probe failures observed on Z shot 2713.

3.4.2 SVS measurements on Z shot 2713

Z shot 2713 failed to return absorption features in the SVS data. However, due to the larger liner dimensions and the Z accelerator's long pulse operation, a shockwave is not expected to have formed. Thus, we do not expect the Na or Ba deposited on the liner's inner surface to have significantly distributed themselves throughout the liner's interior volume. That is, the observed null result is not necessarily surprising.

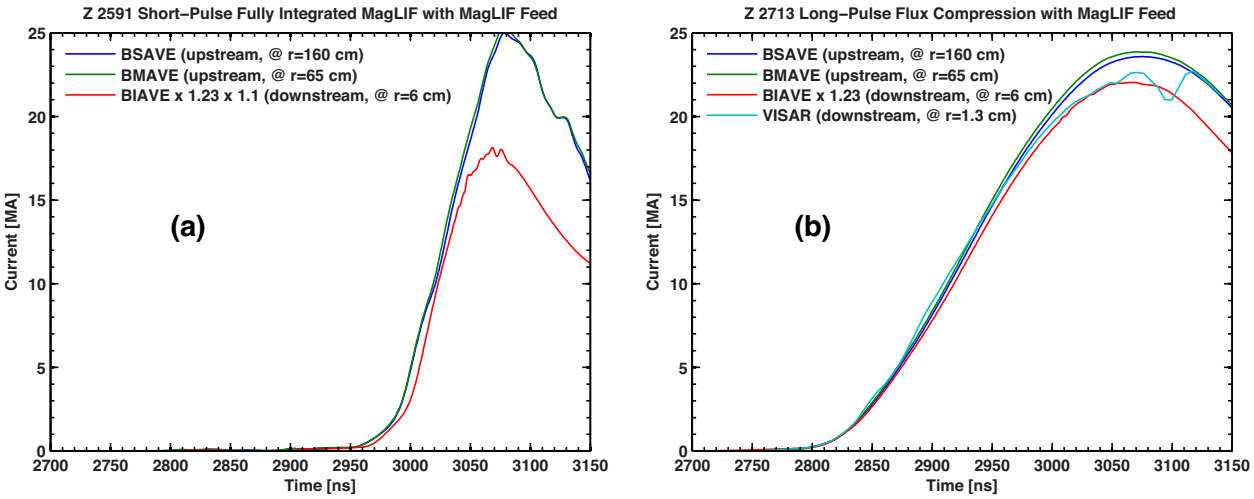

Figure 3.18: (a) Upstream and downstream current pulses measured/inferred for Z shot 2591 (a short-pulse fully integrated MagLIF shot using the standard MagLIF feed and a liner with an outer radius of 2.79 mm [16]). (b) Upstream and downstream current pulses measured on Z shot 2713 (a long-pulse flux compression shot using the standard MagLIF feed and a liner with an outer radius of 5 mm). Comparing the two shots, the significantly smaller difference between the upstream and downstream current on shot 2713 indicates significantly lower current loss on shot 2713. Here, "upstream" and "downstream" is with respect to the post-hole convolute region on Z. Thus, the current loss that we are referring to here presumably occurs in the post-hole convolute region.

3.4.3 Load current measurements on Z shot 2713

A spinoff benefit from this LDRD project was the demonstration that, relative to standard short-pulse operation on Z, higher peak drive currents can be delivered through the standard MagLIF power feed when larger liner radii are used and the Z accelerator is operated in long-pulse mode. This was demonstrated for the first time on Z shot 2713 (see Fig. 3.18).

3.5 New design for flux compression experiments scheduled for November of 2015

Because of the suspected problems caused by the joint between the liner's outer surface and the top electrode on Z shot 2713, we have redesigned the target to make the liner monolithic with the upper electrode. This new design is shown in Fig. 3.19. In this design, we also make use of solid conical stainless steel (S/S) end caps, which serve as "glide planes" to mitigate various end-effect instabilities.

For the design shown in Fig. 3.19, we decided to drop the fringe field micro B-dot measurements as well as the SVS measurements. This was done to remove any unnecessary risk to meeting our primary objective for these experiments, which is to measure a rise from 10 T (or 20 T)

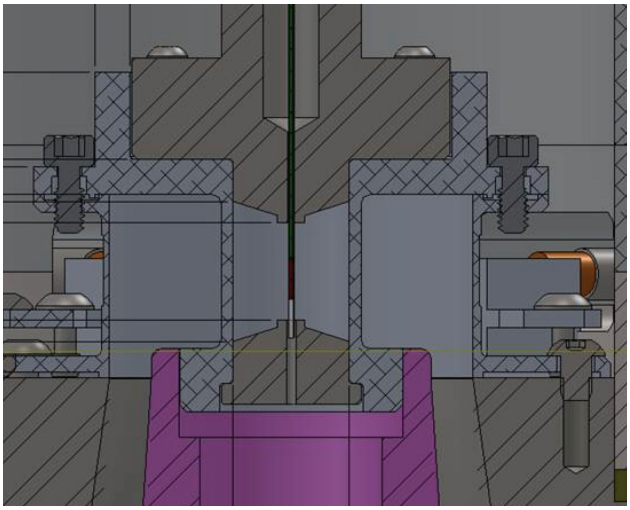

Figure 3.19: The new liner target design that will be tested on Z in November of 2015. This design attempts to maximize the robustness of the Faraday rotation measurement.

to $\sim$1000 T in under 100 ns, directly, using the Faraday rotation diagnostic. The thought is that the monolithic liner-electrode structure combined with the solid S/S conical end caps should be sufficient to stave off any pressure waves from prematurely crushing the Faraday rotation fiber on axis.

These design choices were fleshed out through a series of design simulations using the ALEGRA code (Fig. 3.20). In these simulation results, a very stable liner implosion has been achieved and the end-effect instabilities have been kept well away from where the Faraday fiber would be located on axis. The result of this very stable implosion is a very uniform flux compressed B_z field on axis at stagnation. This compressed B_z field reaches approximately 1000 T just before the liner impacts the Faraday probe.

Three shots are scheduled for testing this design on the Z accelerator in November of 2015. For the first shot, we will request $B_z(0) = 10$ T. Depending on our success with $B_z(0) = 10$ T, we may attempt $B_z(0) = 20$ T on the second or third shots.

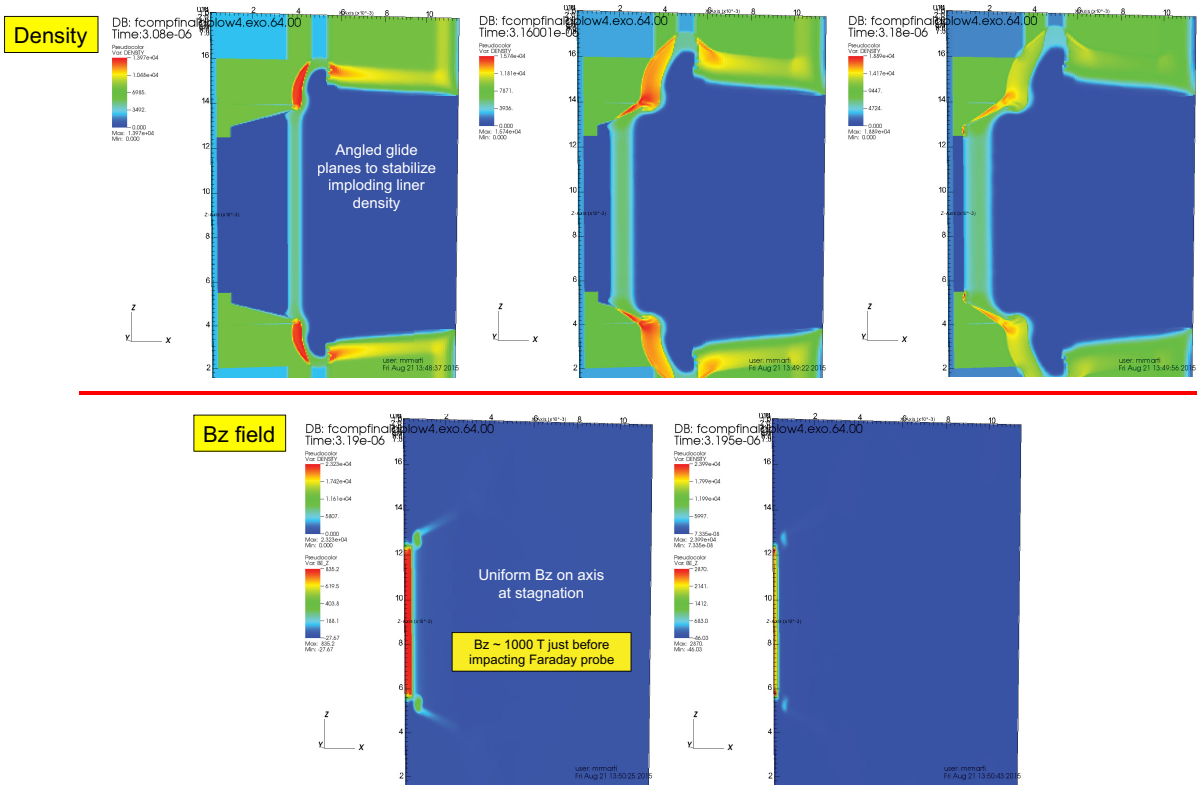

Figure 3.20: ALEGRA 2D simulation of the new liner target design shown in Fig. 3.19. This design attempts to maximize the robustness of the Faraday rotation measurement and will be tested on Z in November of 2015.

Chapter 4

Micro B-dot package development and experiments on the COBRA facility

As discussed above, in Sec. 3.1.1, we have pursued various research and development activities into finding novel ways to fabricate "true B_z-dot probes" [i.e., micro B-dot packages that would be capable of directly measuring $B_z(t)$ inside of an imploding liner]. The various approaches investigated involve making the loops out of traces on a printed circuit board (i.e., the "quad-pack" design of Secs. 4.1 and 4.2 below) as well as printing the entire package using a new multi-material 3D printing capability that has only just recently become available (within the past few months at the time of this writing) (Sec. 4.3 below).

Both the quad-pack design and the 3D printing design were based on the desire to make a true differential measurement, where the positive and negative signals of a differential pair physically share the same B-dot sensing loop (see Fig. 4.1). Differential probes have the advantage of better common-mode noise rejection. For example, in the harsh environment of the Z accelerator, high-energy particles can bombard the probes and deposit electrical charge (and thus a non-zero bias voltage) on the conductors. This can cause the signal voltages and/or the ground voltages (i.e., the reference points for the signal voltages) to drift. However, in a true differential measurement, the drift is the same on both the positive and negative channels, and thus the difference between the two channels (i.e., the differential measurement) is preserved. Another benefit of a true differential measurement is that it cuts the voltage per signal cable in half, which could be important as $\dot{\Phi}_{loop}$ voltages approach the signal cable threshold voltage of roughly 1 kV.

The down side to differential probes is that they require twice the number of signal cables, which need to be routed to twice as many digitizer/oscilloscope channels. Also, a differential probe could be sensitive to inadvertent inductive voltage pickup in any ground loops formed between its two signal cables anywhere along the signal path from the probe to the digitizer/oscilloscope.

4.1 Design and fabrication of the "quad-pack" micro B-dot package

As mentioned above, the "quad-pack" was designed to be a true differential probe (*cf.* Fig. 4.1). However, as in the discussion pertaining to Fig. 3.2 above, the sensing loop illustrated in Fig. 4.1

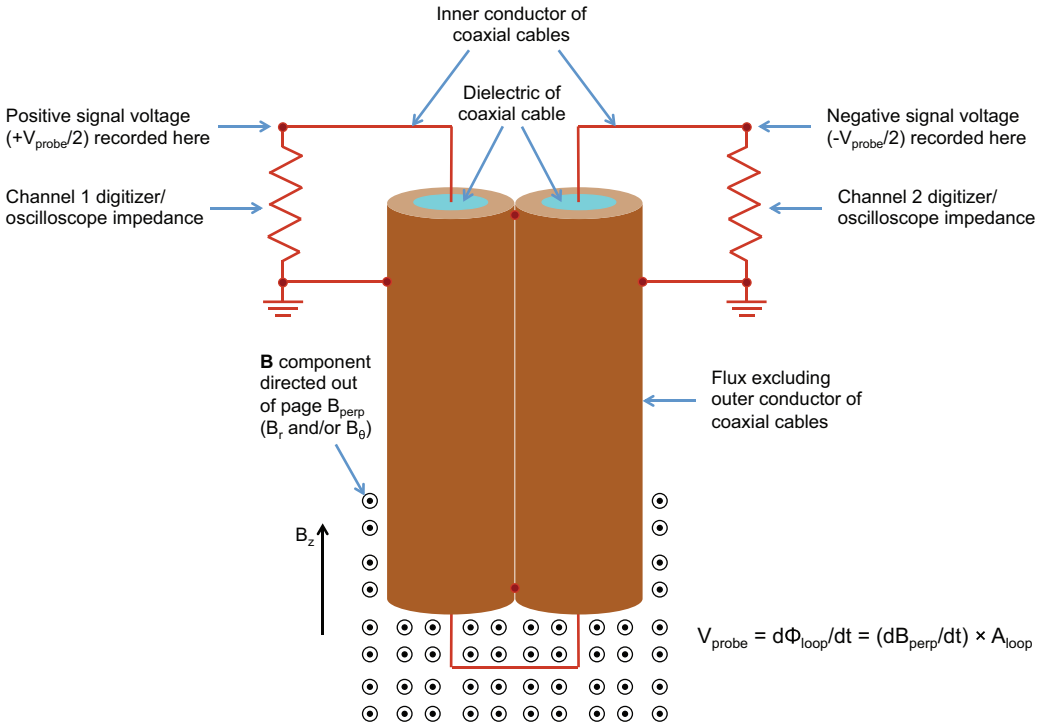

Figure 4.1: Standard true differential probe construction using coaxial cables. This particular implementation is not conducive to measurements of $B_z(t)$ inside of an imploding liner [only $B_\theta(t)$ and/or $B_r(t)$ could be measured reasonably well inside of an imploding liner with this configuration].

must be reoriented by 90° to sense $B_z(t)$ down inside of an imploding liner. However, this leads to the vertical standoff issue described in Fig. 3.2(b). To mitigate the standoff issue, the quad-pack design puts two true differential probes, with loops reoriented by 90° to sense $B_z(t)$, back-to-back and thus in close proximity to each another, as shown in Fig. 4.2. (Thus, in this design, four coaxial cables are bundled together in a "quad-package". The overall package size increases by only 20% in going from two coaxial cables to four, since the packing efficiency of four cables is higher than that of two.) Because the two differential pairs are in close proximity to each other, they together form a differential pair that can "reject" the unwanted, cross-cutting orthogonal components B_r and/or B_θ (which are represented by B_{perp} in Fig. 4.2). That is, by taking the full differential voltage of pair A and averaging it with the full differential voltage of pair B, we can obtain a measurement of $B_z(t)$ that is less contaminated by the cross-cutting components B_r and/or B_θ.

Despite this design's ability to reject common, unwanted, cross-cutting components, there is a further subtly of this design that we must address. The flux-excluding outer conductors of the four coaxial cables (which are soldered together) cause the B_z field that we are trying to measure to bend around the outer conductors. Thus, B_z is transformed into B_r in the vertical standoff region. This B_r penetrates the vertical standoff portions of the two loops and causes the full differential voltages to increase, in the same way, in both pairs A and B. This means that, effectively, the vertical standoffs increase the two probes' sensitivities to B_z. However, this increase in sensitivity to B_z is not necessarily dependent on the length of the vertical standoff. To understand the increase in sensitivity, we need to consider the number of B_z field lines that exist in the unperturbed portion

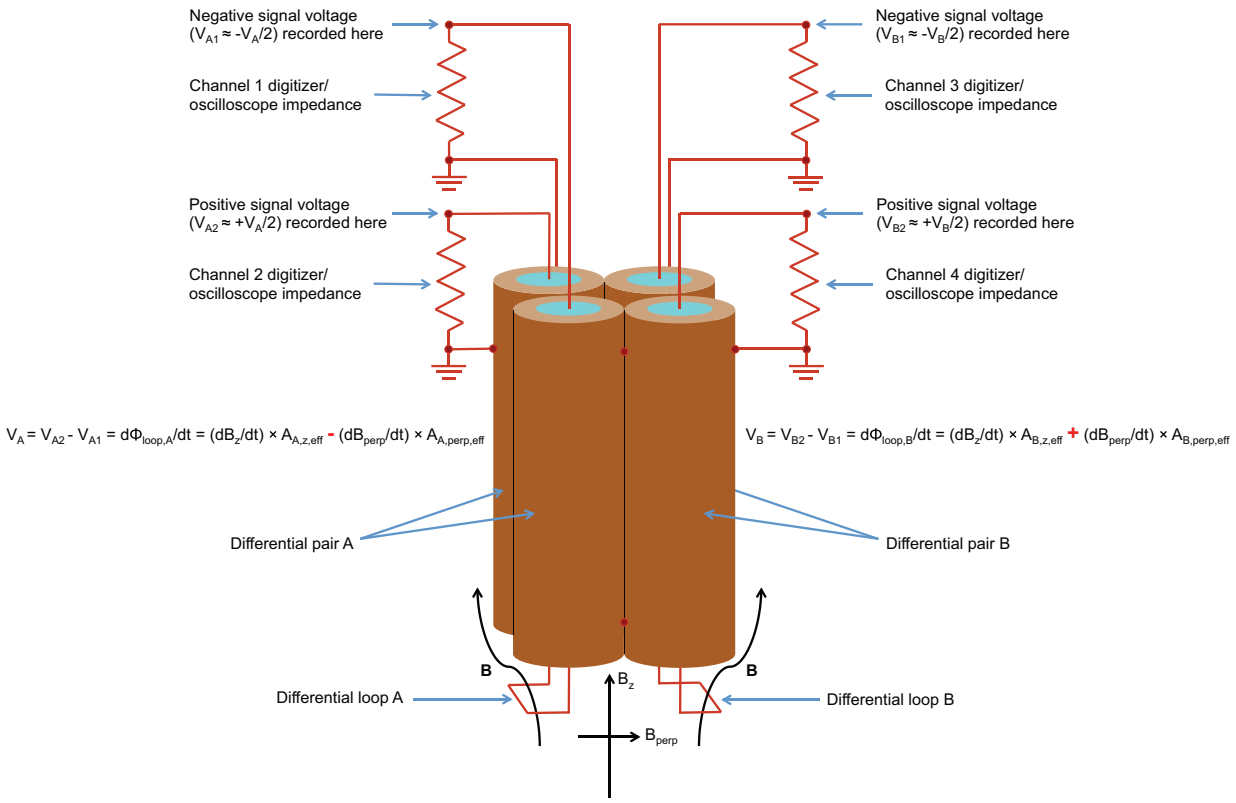

Figure 4.2: Conceptual illustration of the quad-pack design.

of the field, well below the flux excluding coaxial cables, which penetrate either the B_z sensing portion of the loop or the B_r sensing (vertical standoff) portion of the loop. With perfect cylindrical symmetry, the B-field fans out radially (transforming from B_z to B_r) as the field lines approach the coaxial cables from below. Because of the overall cylindrical symmetry, this fanout around the outer conductors of the four coaxial cables is symmetric about the quad-pack's overall axis of symmetry. Thus, with this assumption of perfect cylindrical symmetry, the increase in the effective area of each differential pair's loop sensitivity to B_z due to the vertical standoff is represented by the two partially-transparent yellow-shaded triangular regions in Fig. 4.3.

A SolidWorks model of the quad-pack design was constructed (see Figs. 4.4 and 4.5). The direct B_z sensing portion of the quad-pack loops were constructed from printed-circuit-board (PCB) traces laid out to make two 200-μm $\times$ 200-μm square/U-shaped loops. The traces run along the bottom surface of the PCB and connect to four vias (i.e., electrically conducting through-holes that run from the PCB's bottom surface to its top surface). The center conductors from the four 0.020" (508-μm) outer-diameter semi-rigid coaxial cables were inserted into and soldered to the vias, thus establishing an electrical connection between the center conductors and the loop traces. The quad-packs were assembled at Sandia's Systems Integration Test Facility (SITF) in the medium bay of building 970 by members of Organization 5445 (Electromagnetic Launch Systems). The various scale sizes involved with this assembly procedure are illustrated in Fig. 4.6.

Fabrication of the thin PCBs turned out to be more challenging than expected [90]. Two lo-

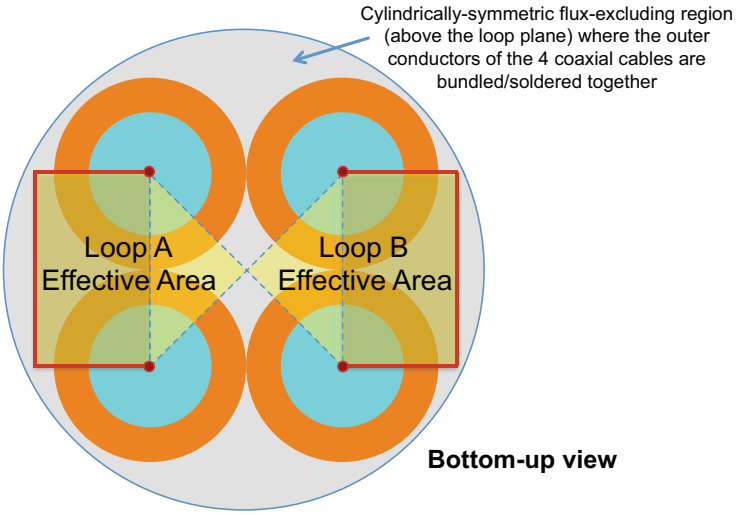

Figure 4.3: Conceptual illustration showing the effective loop areas that are sensitive to $B_z(t)$ assuming a perfectly symmetric radial fanout of the B field as the field lines approach the flux excluding region from below.

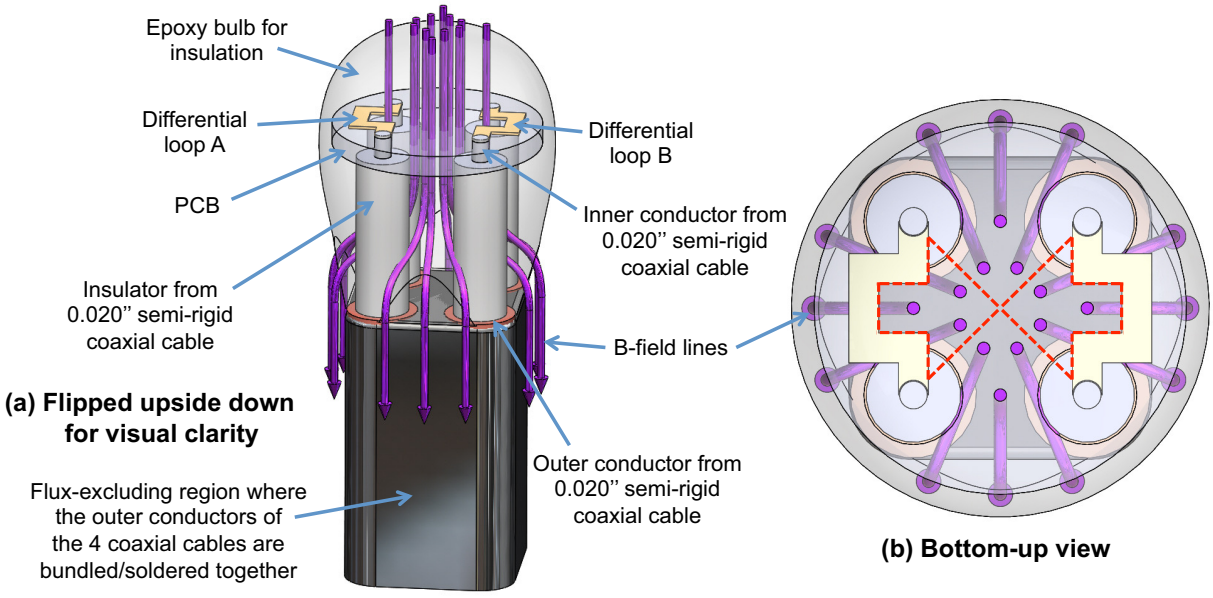

Figure 4.4: Graphics from the SolidWorks model of the quad-pack design. The magnetic field lines (purple arrows) are visual aids for understanding the conceptual operation of the quad-pack and the areas of the probe that are sensitive to $B_z(t)$. The PCB is partially transparent for illustrative purposes. In (b), the two regions within the dashed red lines represent the areas of the two differential loops that are effectively sensitive to $B_z(t)$, assuming a symmetric radial fanout of the B-field around the flux excluding region. In practice, the probes are calibrated relative to a known reference to find the true sensitivity to $B_z(t)$.

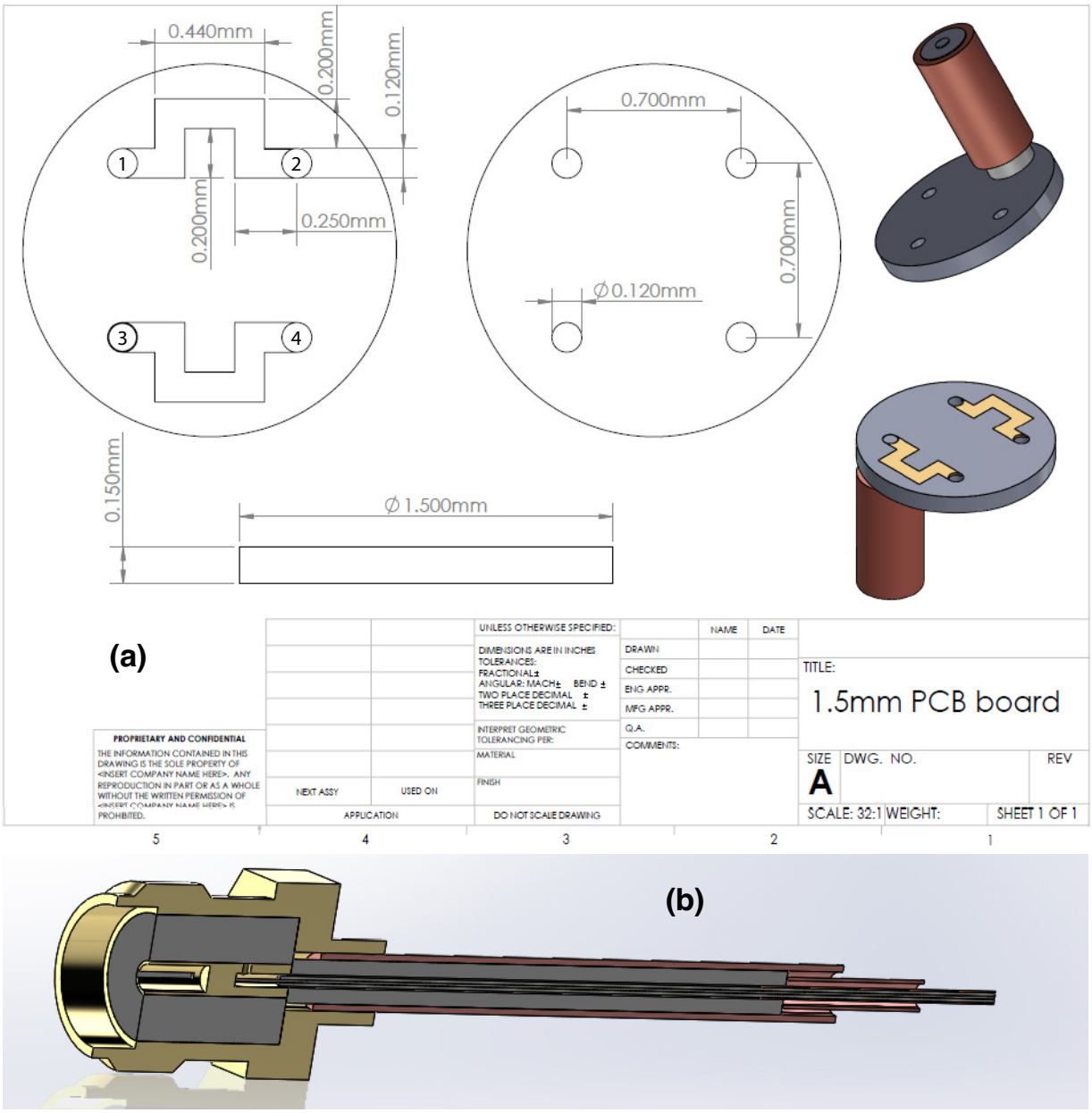

Figure 4.5: (a) Engineering drawing for the printed circuit board (PCB) component of the quad-pack micro B_z-dot design. Here the signal numbering convention (1–4) is also indicated. (b) SolidWorks model graphics illustrating the careful attention paid to proper SMA connectorization for the quad-pack design.

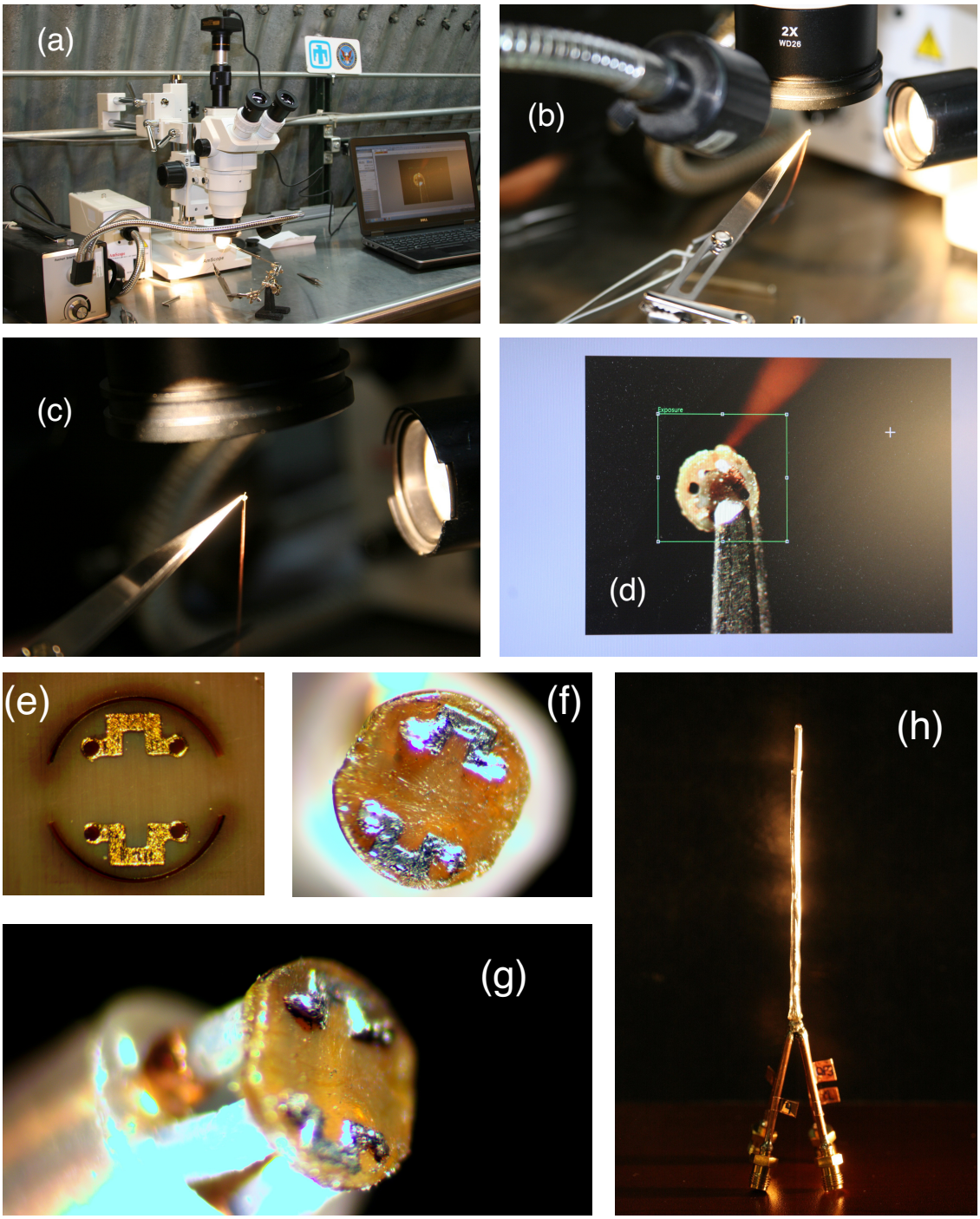

Figure 4.6: Photographs of the various scale sizes involved with quad-pack assembly. (a) Tweezers holding an 0.020" semi-rigid coaxial cable soldered to a quad-pack PCB under the microscope that was purchased to enable quad-pack assembly. (b) That in (a) zoomed in. (c) That in (b) zoomed in. (d) That in (c) zoomed in. In (d), the poor quality of the PCB traces and vias that resulted from earlier PCB fabrication attempts at local shops is apparent. (e) The much improved PCB trace and via quality obtained from Sierra Circuits Proto Express in California. (f) That in (e) after solder has been applied to assemble the quad-pack. (g) Slightly rotated view of that in (f) for perspective. (h) Full view of a completed quad-pack assembly.

cal shops were unable to deliver satisfactory results; however, these shops did help us identify a specialized company in California (Sierra Circuits Proto Express) that was able to deliver very clean PCB traces and laser-drilled vias at specified dimensions. In the end, each quad-pack PCB was a Kapton single layer flex board with a diameter of 1.5 mm, a thickness of 0.006" (152 μm), and an electroless nickel-gold finish. The laser-drilled vias were 0.005" (127 μm) in diameter. Nickel-gold traces were selected because of their ability to tolerate the heat of laser drilling.

4.2 Testing of the "quad-pack" at Cornell University's COBRA facility

A total of eight quad-packs were fabricated (referred to as QBERT-1–QBERT-8). These probes were calibrated and tested at Cornell University's Laboratory of Plasma Studies. The calibration was done on a small pulser using a reference B-dot probe. The full-scale quad-pack testing was done on the COBRA pulsed-power facility (0–1 MA in 100 ns) [54], where we performed five experiments: COBRA shots 3704–3709, which were conducted over the four-day period of September 8–11, 2015.

Photographs of the experimental setups are presented in Figs. 4.7–4.11. To generate a reasonably uniform, large, fast-rising axial magnetic field ($\sim$0–100 T in 100 ns), we used an "Ω" coil as the load (Figs. 4.7–4.10), which helped to keep the inductive loading on COBRA to a reasonable level. The Ω coils were placed across COBRA's anode-cathode cap. The field-sensing probe loops were positioned as close to the center of the coils as possible, both axially and radially within the coils. The coil axial lengths were 6–6.5 mm. The coil inner diameters were 6.2–6.44 mm. The coil input gaps were 2.75–3.2 mm. On shot 3706 (Fig. 4.8), we added a 3.5-mm vertical extension to the bottom of the Ω coil, thus the coil resembled that of an old fashioned keyhole (we referred to this as the "keyhole" coil). On COBRA shot 3709 (Fig. 4.11), we attempted a power-feed-gap physics experiment, where instead of using an Ω or keyhole coil, we used a roughly planar power-feed-like load, which was terminated with two 254-μm-diameter aluminum wires. The two vaporizing/exploding wires were used to provide a radiation/plasma source that could potentially alter the power flow in the feed gap and/or alter the probe performance. All of the coils/loads were made from $\sim$1-mm-thick sheet metal.

On COBRA shots 3704 (QBERT-2) and 3705 (QBERT-5), the quad-packs were tested on their own (see Fig. 4.7). On COBRA shot 3706, a standard Cornell micro B-dot probe was introduced just outside one end of the coil to measure fringe fields [in a form similar to that illustrated in Fig. 3.2(d)] while QBERT-8 measured the axial field inside of the coil (see Fig. 4.8). On COBRA shots 3707 (QBERT-7) and 3708 (QBERT-4), both a novel Cornell true B_z-dot probe [similar to that illustrated in Fig. 3.2(c)] and a quad-pack were fielded to measure the axial field inside of the coil (see Figs. 4.9 and 4.10). On COBRA shot 3709 (i.e., the power-feed-gap physics experiment), we used QBERT-6 and a standard Cornell micro B-dot probe to measure the fields within the power delivery region (see Fig. 4.11).

The results of the COBRA experiments are presented in Figs. 4.12 and 4.13. In each figure, the

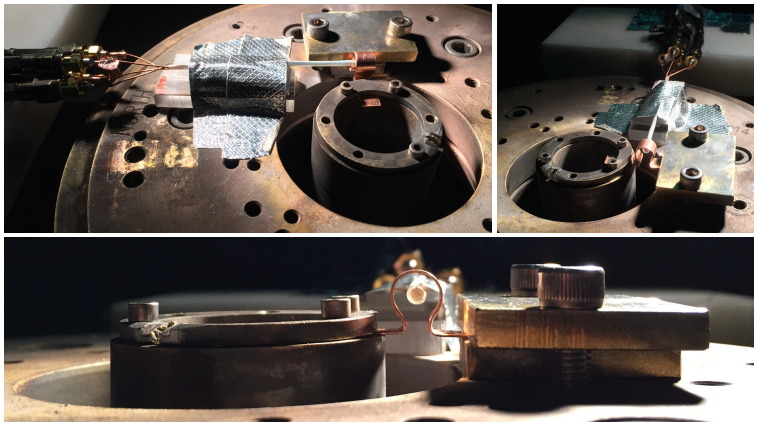

Figure 4.7: Photographs of the experimental setup for COBRA shot 3705. (The 3704 setup was similar.)

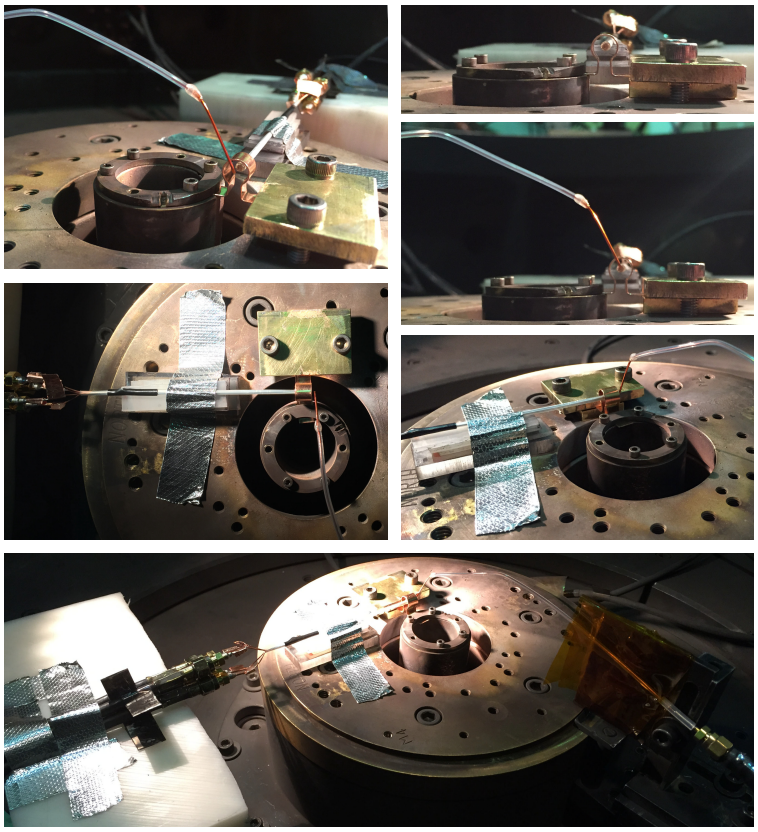

Figure 4.8: Photographs of the experimental setup for COBRA shot 3706.

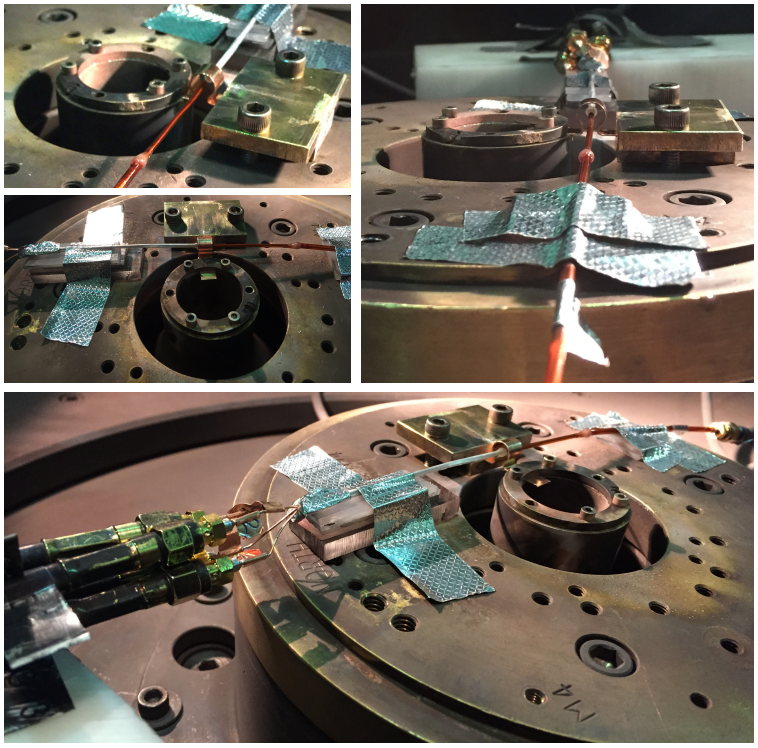

Figure 4.9: Photographs of the experimental setup for COBRA shot 3707.

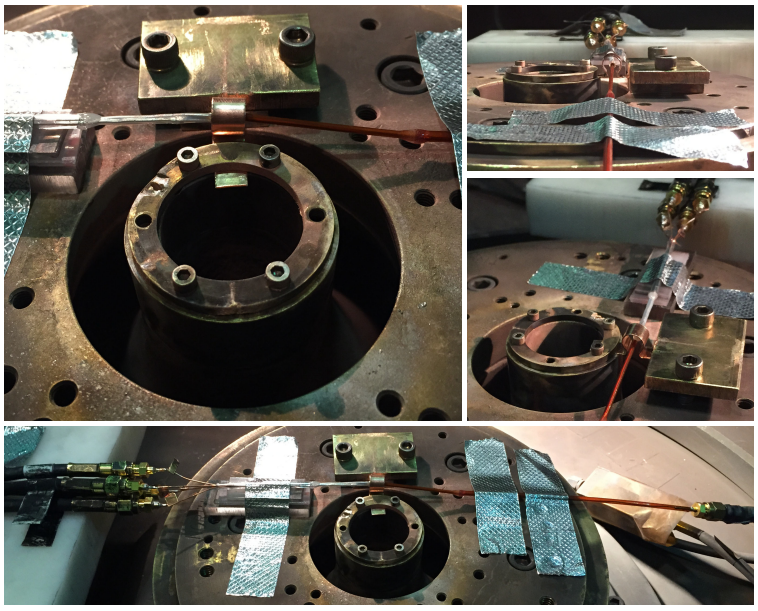

Figure 4.10: Photographs of the experimental setup for COBRA shot 3708.

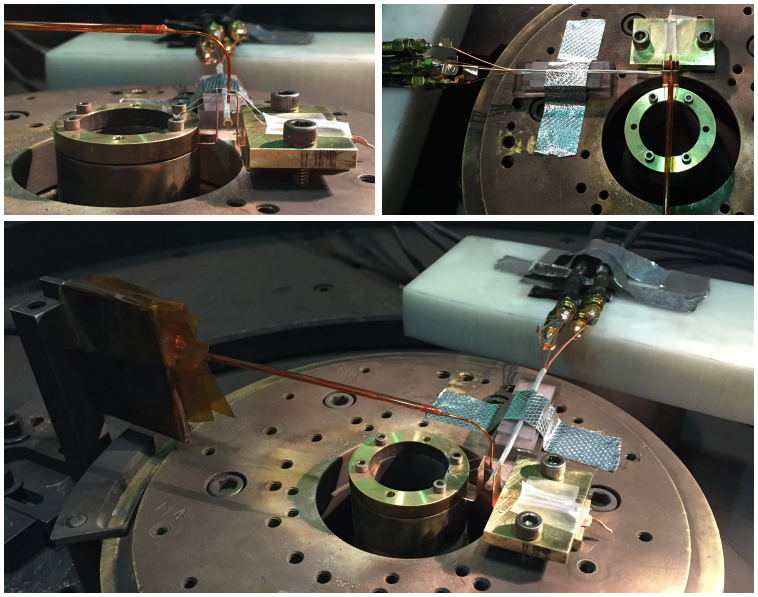

Figure 4.11: Photographs of the experimental setup for COBRA shot 3709.

raw signal voltages are presented in the left column, and the time-integrated signals are presented in the right column. The error bars indicate the spread between the two differential pairs of the quad-packs. Large error bars indicate large cross-cutting (non-axial) field components and possibly other non-ideal behavior. In general, the waveform shapes of the axial fields measured by the quad-packs agree well with the waveform shapes of the COBRA load current measured by a Rogowski coil and the waveform shapes of the fields measured by the Cornell micro B-dot probes. Notably, excellent quad-pack results were obtained on shots 3704 and 3707. For shots 3705, 3706, 3708, and 3709, the non-ideal behavior observed could have been the result of plasmas in and around the various load coils tested. These plasmas were observed both axially and side-on using time-gated XUV pinhole camera imaging (see Fig. 4.14)

4.3 Design of a novel differential micro B-dot package to be fabricated using new multi-material 3D printing technology

A new and exciting development in the world of additive manufacturing is the ability to 3D print multi-material packages.[1] This is true for at least one company at the time of this writing: EoPlex in San Jose, California. As shown in Fig. 4.15, EoPlex is capable of printing both electrical conductors and electrical insulators together in the same package. This capability is potentially game changing for micro B-dot probe fabrication.

[1]This multi-material capability has only just recently become available (within the past few months at the time of this writing).

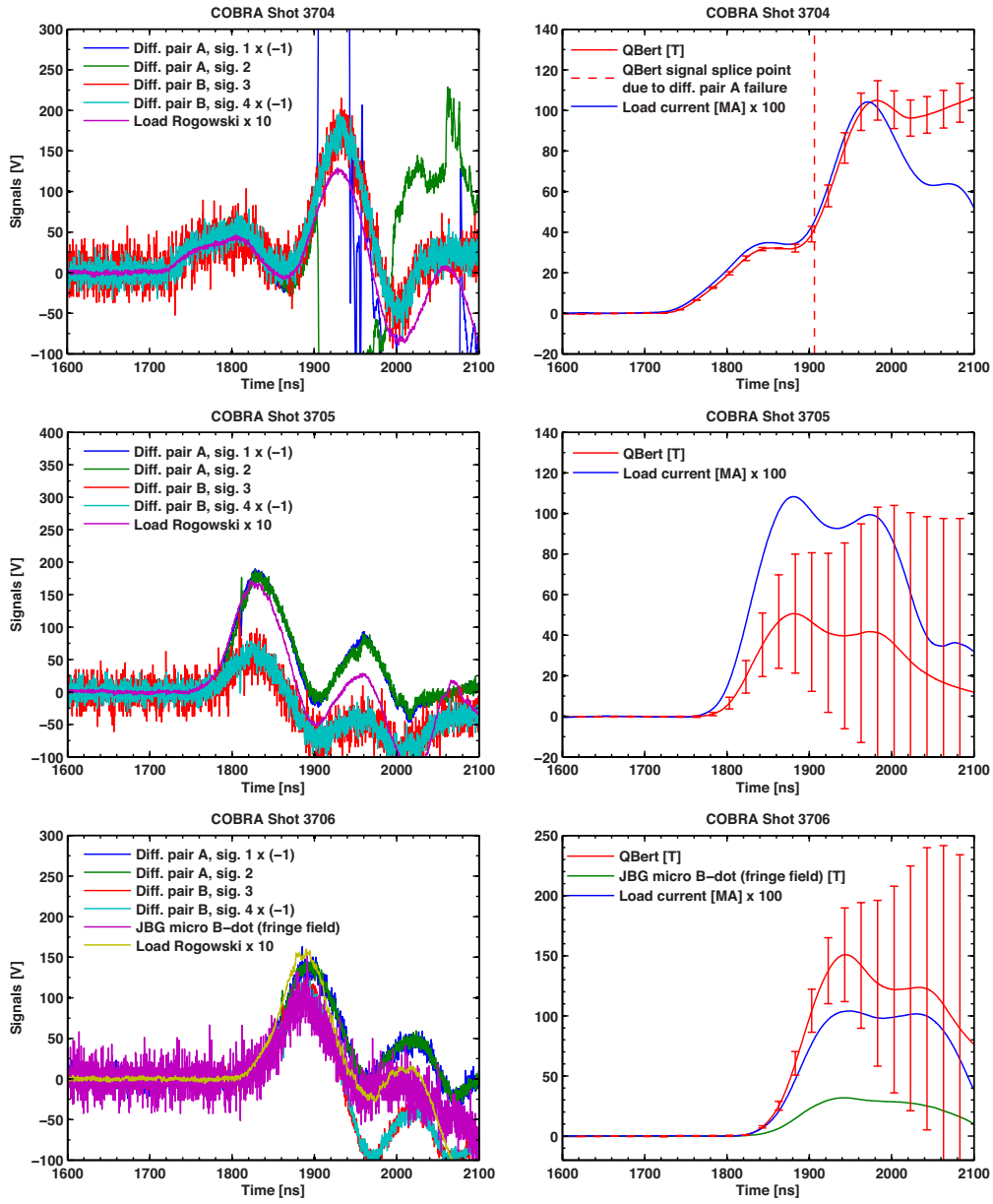

Figure 4.12: Experimental data collected for COBRA shots 3704–3706. The raw signal voltages are presented in the left column. The time-integrated signals are presented in the right column. The error bars indicate the spread between the two differential pairs of the quad-packs. Large error bars indicate large cross-cutting (non-axial) field components and possibly other non-ideal behavior. On shot 3704, quad-pack differential pair A failed at $t = 1906$ ns; after $t = 1906$ ns, a constant ratio of differential pair A to differential pair B was assumed (which is the ratio of the two pairs at $t = 1906$ ns) to generate the mean axial field plotted. In general, the waveform shapes of the axial fields measured by the quad-packs agree well with the waveform shapes of the COBRA load current measured by a Rogowski coil and, on shot 3706, the waveform shape of the fringe field measured by a standard Cornell micro B-dot probe. Notably, excellent quad-pack results were obtained on shot 3704.

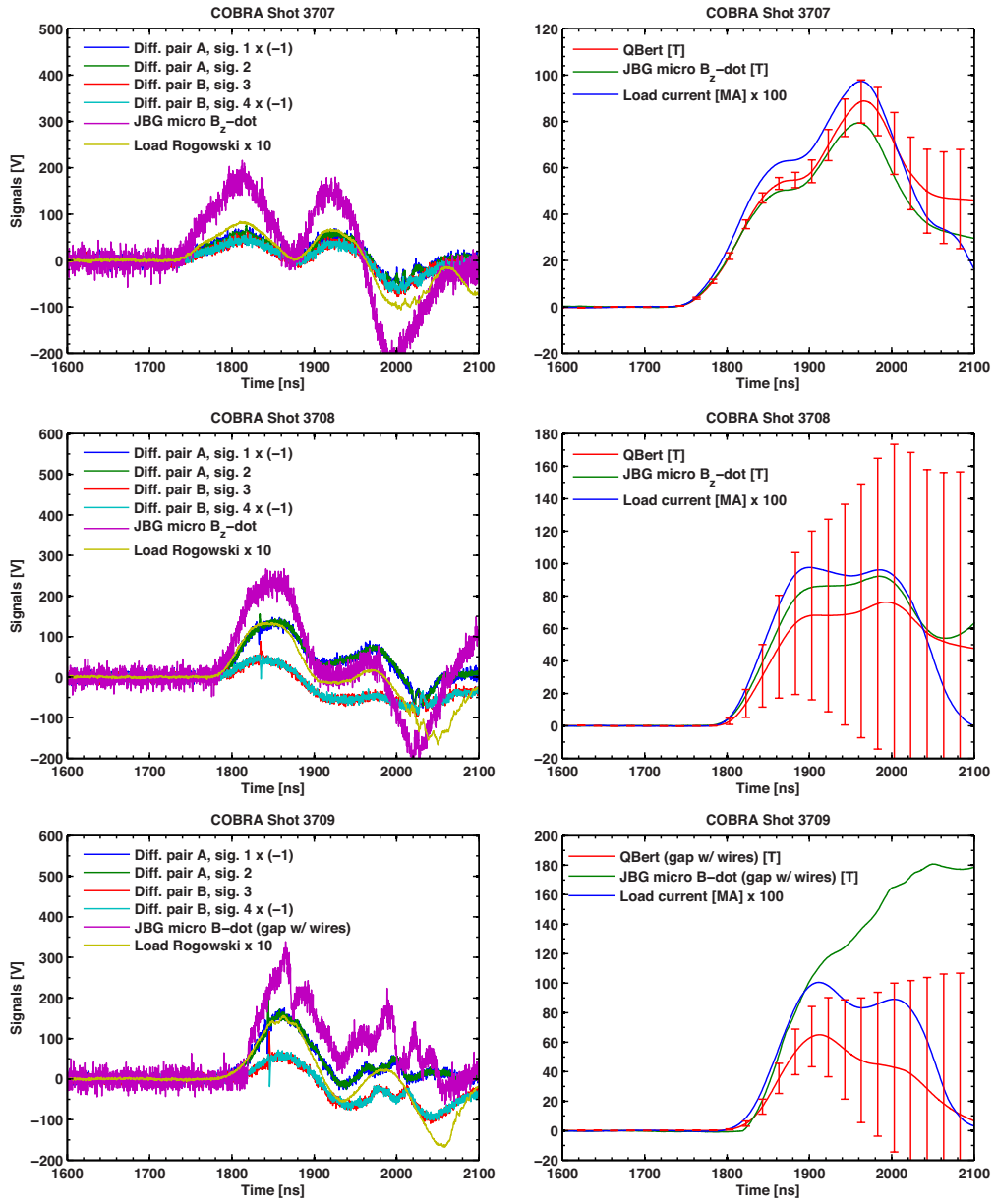

Figure 4.13: Experimental data collected for COBRA shots 3707–3709. The raw signal voltages are presented in the left column. The time-integrated signals are presented in the right column. The error bars indicate the spread between the two differential pairs of the quad-packs. Large error bars indicate large cross-cutting (non-axial) field components and possibly other non-ideal behavior. In general, the waveform shapes of the axial fields measured by the quad-packs agree well with the waveform shapes of the COBRA load current measured by a Rogowski coil and the waveform shapes of the fields measured by Cornell micro B-dot probes. Notably, excellent quad-pack results were obtained on shot 3707.

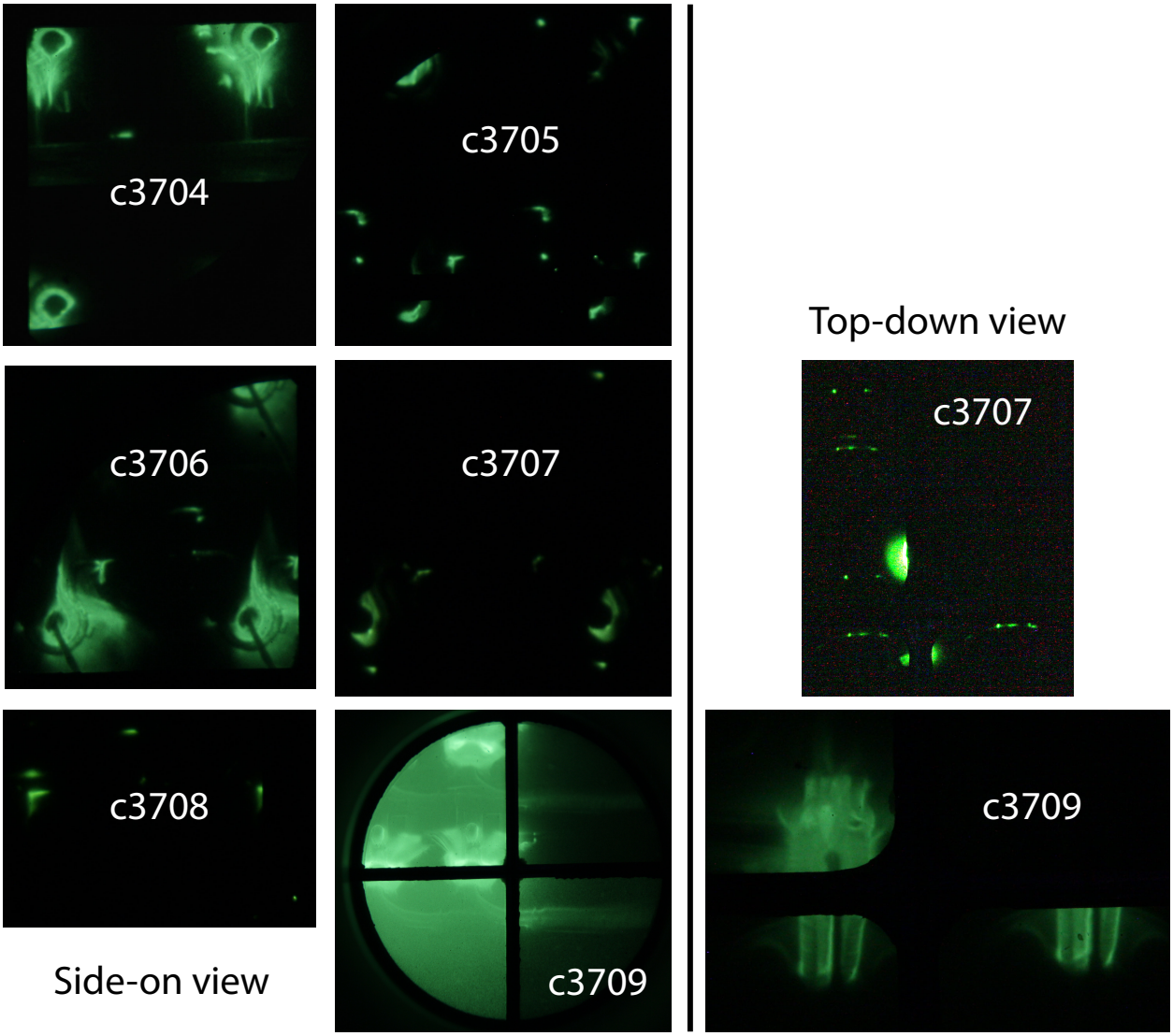

Figure 4.14: Four-frame, time-gated XUV pinhole camera images taken during the COBRA experiments. Both side-on and axial views were obtained, though the axial views were often problematic due to obstructions and/or other technical difficulties. These images reveal the presence of plasmas in and around the various load coils tested. These plasmas could have been the culprit for some of the non-ideal behavior observed in the quad-pack data.

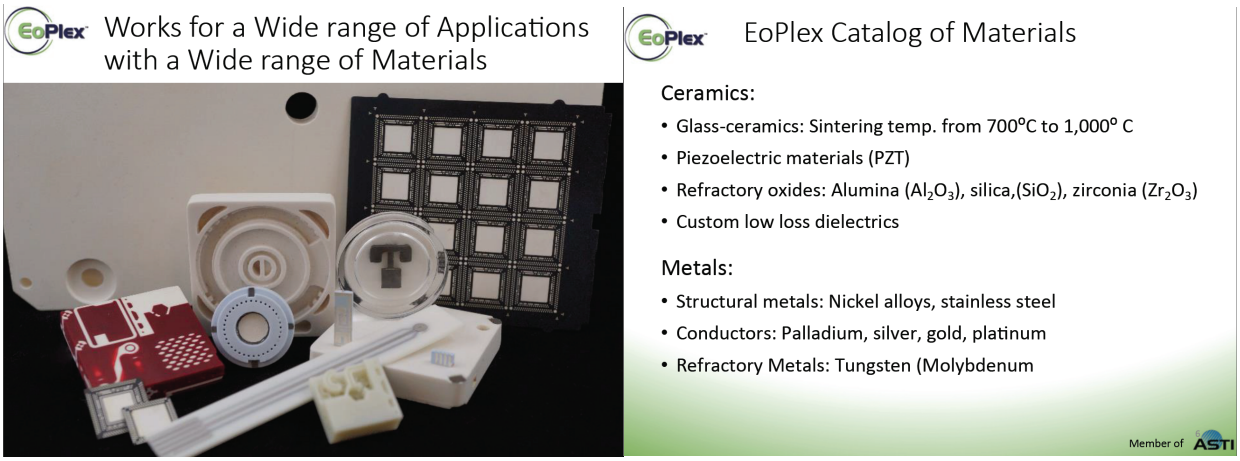

Figure 4.15: Multi-material 3D printing capabilities at EoPlex in San Jose, California.

With this new capability in mind, a novel differential micro B-dot package has been designed (Fig. 4.16). This work is the result of a collaboration between Sandia Organizations 1688 (High Energy Density Experiments) and 1718 (Microsystems Integration). The breakthrough, which 3D printing this probe will enable, is that a very small window/port can be made in the flux-excluding outer conductor, which the B_z-dot sensing loop formed by the inner conductor can then pass through to sense the B_z field outside of the flux-excluded region. The grounded flux excluder and the two leads of the inner conductor are then connected to a printed circuit board, which supports connecting traces and mounting footprints for two standard SMA connectors. Because the flux excluder extends for a long distance above and below the B_z-dot sensing loop, the B_z field will be compressed up against the outer surface of the flux excluder in a nominally uniform and unperturbed manner (i.e., $B_r \approx B_\theta \approx 0$). Also, the loop plane can be precisely controlled to be sensitive only to B_z. That is, this design does not suffer from the vertical standoff issues that the quad-pack design (Secs. 4.1 and 4.2) has to manage. Thus, unlike the quad-pack design, this design does not require dual differential pairs to cancel unwanted B_r and/or B_θ components, and therefore, relative to the quad-pack design, this design requires half the number of signal cables and digitizer/oscilloscope channels.

The design presented in Fig. 4.16 is only one possibility. Another possibility is printing a high-performing single-ended version. Relative to the differential version, the benefits of a single-ended version include requiring half the number of signal cables and digitizer/oscilloscope channels. Also, the differential version could be sensitive to inadvertent inductive voltage pickup in any ground loops formed between its two signal cables anywhere along the signal path from the probe to the digitizer/oscilloscope—this might not be as big of a concern for the single-ended version because there is only one signal cable; however, even for single-ended probes, ground loops could still be a concern. The benefits of the differential version include automatic rejection of common-mode noise, which can come from sources like high-energy particles depositing charge (and thus bias voltage) on the conductors; common-mode rejection is a potentially important consideration for fielding these types of probes in harsh environments like those found on the Z accelerator. Another benefit of the differential implementation is that it cuts the voltage per signal cable in half, which could be important as $\dot{\Phi}_{loop}$ voltages approach the signal cable threshold voltage of roughly

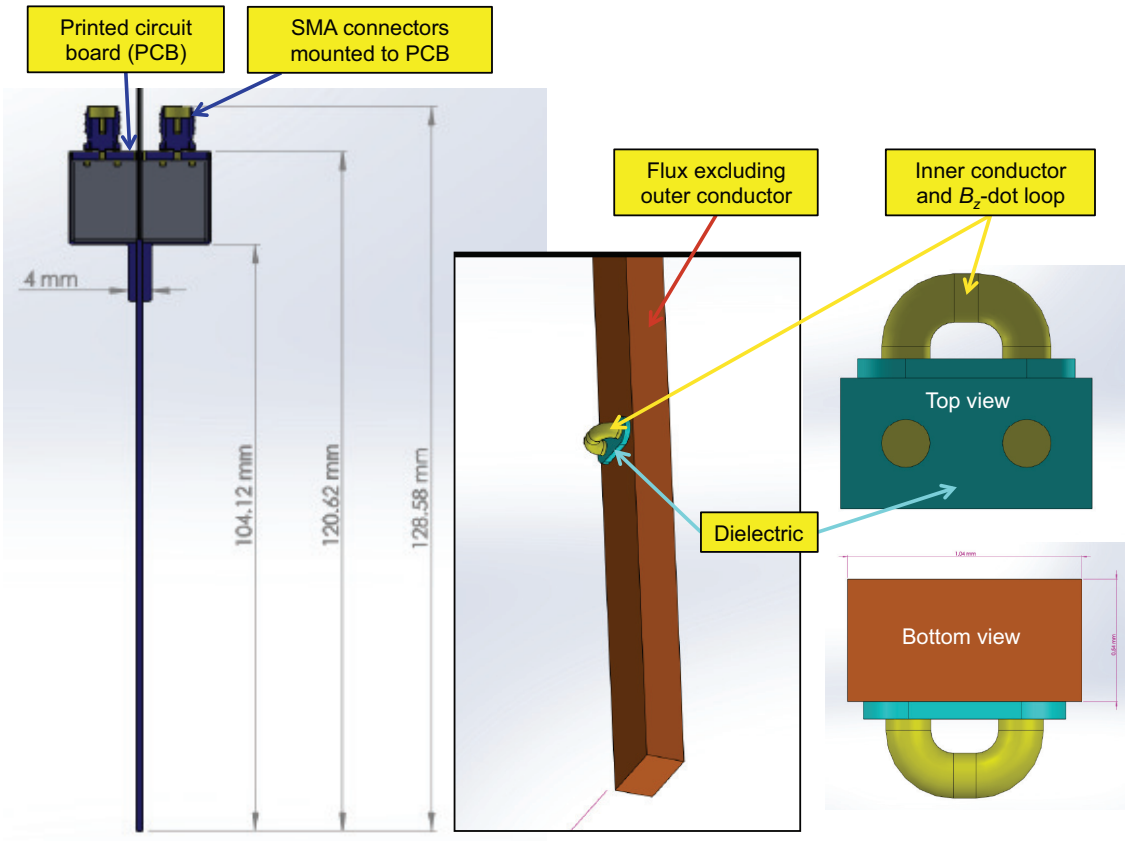

Figure 4.16: The design of a novel differential micro B-dot package to be fabricated using new multi-material 3D printing technology.

1 kV.

To further isolate the system from potential noise sources, both the differential and the single-ended versions could be enclosed in an additional outer conductor [i.e., an additional (possibly floating) flux excluder, again with a port for the B_z-dot sensing loop to pass through]. This additional flux excluder would be the third conductor (and the outermost conductor), and thus this structure would be an implementation of a triaxial system. The downside of a triaxial system is that the overall package size would increase slightly, thus we would be trading available liner convergence (prior to probe impact) for noise rejection. All of these implementations have pros and cons, therefore experimental testing is required.

Our plans for the near future include securing additional funding to 3D print these various probe implementations. We will then test the printed probes on the COBRA facility. If any of these implementations look promising on CORBA, then we will make arrangements to test them on a full-scale flux compression experiment on Z. At the time of this writing, however, the EoPlex company is down for retooling for the next several months (i.e., after a short research and development run to demonstrate proof of principle, they are now retooling to go into full-scale production mode). Once the EoPlex production facility is online, we will make arrangements to begin fabricating and testing these novel micro B_z-dot probe packages.

Chapter 5

Conclusion

This LDRD project has resulted in a number of significant accomplishments:

1. We have developed an experimental platform that supports up to three independent probe-based diagnostic techniques for measuring vacuum flux compression on Z; the diagnostic techniques developed include:
   (a) Micro B-dot probes for measuring the dynamic fringe fields above an imploding liner;
   (b) Streaked visible Zeeman absorption spectroscopy for measuring the fields inside of an imploding liner;
   (c) Fiber-based Faraday rotation for measuring the fields inside of an imploding liner.
2. We have conceived of two novel approaches for fabricating noise-rejecting micro B_z-dot probe packages; these approaches, which could eventually be used for measuring flux compression fields inside of an imploding liner on Z, include:
   (a) The quad-pack design with differential pickup loops fabricated on printed circuit boards (these have been fabricated at Sandia and tested at Cornell's COBRA facility);
   (b) Differential and single-ended micro B_z-dot probe packages to be fabricated using new multi-material 3D printing capabilities (i.e., metals and dielectrics can be printed together in the same packages at EoPlex's facility once the company's retooling is completed; this retooling should be completed within a few months from the time of this writing).
3. We have executed a substantial amount of liner implosion design work using the GORGON and ALEGRA simulation codes to ensure compatibility of diagnostics with implosion instabilities; two spinoff benefits from this experimental design work include:
   (a) The development of the "cushion" end caps, which have been incorporated into the fully-integrated MagLIF platform due to their ability to mitigate end-effect instabilities;
   (b) The use of atomic layer deposition to apply a thin (85-nm thick) platinum (Pt) coating to the liner's inner surface to enhance the contrast of the liner's inner surface in radiographic images.
4. We have developed new field solvers and synthetic diagnostics for the simulation codes.

5. We have demonstrated that, relative to standard short-pulse operation on Z, higher peak drive currents can be delivered through the standard MagLIF power feed when larger liner radii are used and the Z accelerator is operated in long-pulse mode; this demonstration is a spinoff benefit from this LDRD project.

Additionally, for neutron producing experiments with hot plasma gradients (e.g., fully integrated MagLIF experiments on Z), we are now able to leverage two new flux compression measurement techniques, which were developed outside the purview (but within the timeframe) of this LDRD project. These techniques use the data from the Z facility's neutron diagnostics suite to assess flux losses. For MagLIF flux compression, the flux losses are likely due to a combination of the Nernst thermoelectric effect and resistive diffusion.

Finally, we are very much looking forward to seeing the outcome of the final vacuum flux compression experiments on Z, which are three shots scheduled for November of 2015. We are also very much looking forward to eventually fabricating and testing the novel 3D printed micro B_z-dot probe packages that have been conceived of and designed under this LDRD project.

References

[1] S. A. Slutz, M. C. Herrmann, R. A. Vesey, A. B. Sefkow, D. B. Sinars, D. C. Rovang, K. J. Peterson, and M. E. Cuneo. Pulsed-power-driven cylindrical liner implosions of laser preheated fuel magnetized with an axial field. *Phys. Plasmas*, 17(5):056303, 2010.

[2] Stephen A. Slutz and Roger A. Vesey. High-gain magnetized inertial fusion. *Phys. Rev. Lett.*, 108:025003, Jan 2012.

[3] D. B. Sinars, S. A. Slutz, M. C. Herrmann, R. D. McBride, M. E. Cuneo, K. J. Peterson, R. A. Vesey, C. Nakhleh, B. E. Blue, K. Killebrew, D. Schroen, K. Tomlinson, A. D. Edens, M. R. Lopez, I. C. Smith, J. Shores, V. Bigman, G. R. Bennett, B. W. Atherton, M. Savage, W. A. Stygar, G. T. Leifeste, and J. L. Porter. Measurements of magneto-Rayleigh-Taylor instability growth during the implosion of initially solid Al tubes driven by the 20-MA, 100-ns Z facility. *Phys. Rev. Lett.*, 105(18):185001, Oct 2010.

[4] D. B. Sinars, S. A. Slutz, M. C. Herrmann, R. D. McBride, M. E. Cuneo, C. A. Jennings, J. P. Chittenden, A. L. Velikovich, K. J. Peterson, R. A. Vesey, C. Nakhleh, E. M. Waisman, B. E. Blue, K. Killebrew, D. Schroen, K. Tomlinson, A. D. Edens, M. R. Lopez, I. C. Smith, J. Shores, V. Bigman, G. R. Bennett, B. W. Atherton, M. Savage, W. A. Stygar, G. T. Leifeste, and J. L. Porter. Measurements of magneto-Rayleigh-Taylor instability growth during the implosion of initially solid metal liners. *Phys. Plasmas*, 18(5):056301, 2011.

[5] M. E. Cuneo, M. C. Herrmann, D. B. Sinars, S. A. Slutz, W. A. Stygar, R. A. Vesey, A. B. Sefkow, G. A. Rochau, G. A. Chandler, J. E. Bailey, J. L. Porter, R. D. McBride, D. C. Rovang, M. G. Mazarakis, E. P. Yu, D. C. Lamppa, K. J. Peterson, C. Nakhleh, S. B. Hansen, A. J. Lopez, M. E. Savage, C. A. Jennings, M. R. Martin, R. W. Lemke, B. W. Atherton, I. C. Smith, P. K. Rambo, M. Jones, M. R. Lopez, P. J. Christenson, M. A. Sweeney, B. Jones, L. A. McPherson, E. Harding, M. R. Gomez, P. F. Knapp, T. J. Awe, R. J. Leeper, C. L. Ruiz, G. W. Cooper, K. D. Hahn, J. McKenney, A. C. Owen, G. R. McKee, G. T. Leifeste, D. J. Ampleford, E. M. Waisman, A. Harvey-Thompson, R. J. Kaye, M. H. Hess, S. E. Rosenthal, and M. K. Matzen. Magnetically driven implosions for inertial confinement fusion at Sandia National Laboratories. *IEEE Trans. Plasma Sci.*, 40(12):3222–3245, Dec 2012.

[6] M. R. Martin, R. W. Lemke, R. D. McBride, J.-P. Davis, D. H. Dolan, M. D. Knudson, K. R. Cochrane, D. B. Sinars, I. C. Smith, M. Savage, W. A. Stygar, K. Killebrew, D. G. Flicker, and M. C. Herrmann. Solid liner implosions on Z for producing multi-megabar, shockless compressions. *Phys. Plasmas*, 19(5):056310, 2012.

[7] R. D. McBride, S. A. Slutz, C. A. Jennings, D. B. Sinars, M. E. Cuneo, M. C. Herrmann, R. W. Lemke, M. R. Martin, R. A. Vesey, K. J. Peterson, A. B. Sefkow, C. Nakhleh, B. E. Blue, K. Killebrew, D. Schroen, T. J. Rogers, A. Laspe, M. R. Lopez, I. C. Smith, B. W.

Atherton, M. Savage, W. A. Stygar, and J. L. Porter. Penetrating radiography of imploding and stagnating beryllium liners on the *Z* accelerator. *Phys. Rev. Lett.*, 109:135004, Sep 2012.

[8] R. D. McBride, M. R. Martin, R. W. Lemke, J. B. Greenly, C. A. Jennings, D. C. Rovang, D. B. Sinars, M. E. Cuneo, M. C. Herrmann, S. A. Slutz, C. W. Nakhleh, D. D. Ryutov, J.-P. Davis, D. G. Flicker, B. E. Blue, K. Tomlinson, D. Schroen, R. M. Stamm, G. E. Smith, J. K. Moore, T. J. Rogers, G. K. Robertson, R. J. Kamm, I. C. Smith, M. Savage, W. A. Stygar, G. A. Rochau, M. Jones, M. R. Lopez, J. L. Porter, and M. K. Matzen. Beryllium liner implosion experiments on the Z accelerator in preparation for magnetized liner inertial fusion. *Phys. Plasmas*, 20(5):056309, 2013.

[9] D. H. Dolan, R. W. Lemke, R. D. McBride, M. R. Martin, E. Harding, D. G. Dalton, B. E. Blue, and S. S. Walker. Tracking an imploding cylinder with photonic doppler velocimetry. *Rev. Sci. Instrum.*, 84(5):055102, 2013.

[10] Kyle J. Peterson, Daniel B. Sinars, Edmund P. Yu, Mark C. Herrmann, Michael E. Cuneo, Stephen A. Slutz, Ian C. Smith, Briggs W. Atherton, Marcus D. Knudson, and Charles Nakhleh. Electrothermal instability growth in magnetically driven pulsed power liners. *Phys. Plasmas*, 19(9):092701, 2012.

[11] Kyle J. Peterson, Edmund P. Yu, Daniel B. Sinars, Michael E. Cuneo, Stephen A. Slutz, Joseph M. Koning, Michael M. Marinak, Charles Nakhleh, and Mark C. Herrmann. Simulations of electrothermal instability growth in solid aluminum rods. *Phys. Plasmas*, 20(5):056305, 2013.

[12] Kyle J. Peterson, Thomas J. Awe, Edmund P. Yu, Daniel B. Sinars, Ella S. Field, Michael E. Cuneo, Mark C. Herrmann, Mark Savage, Diana Schroen, Kurt Tomlinson, and Charles Nakhleh. Electrothermal instability mitigation by using thick dielectric coatings on magnetically imploded conductors. *Phys. Rev. Lett.*, 112:135002, Apr 2014.

[13] T. J. Awe, R. D. McBride, C. A. Jennings, D. C. Lamppa, M. R. Martin, D. C. Rovang, S. A. Slutz, M. E. Cuneo, A. C. Owen, D. B. Sinars, K. Tomlinson, M. R. Gomez, S. B. Hansen, M. C. Herrmann, J. L. McKenney, C. Nakhleh, G. K. Robertson, G. A. Rochau, M. E. Savage, D. G. Schroen, and W. A. Stygar. Observations of modified three-dimensional instability structure for imploding z-pinch liners that are premagnetized with an axial field. *Phys. Rev. Lett.*, 111:235005, Dec 2013.

[14] T. J. Awe, C. A. Jennings, R. D. McBride, M. E. Cuneo, D. C. Lamppa, M. R. Martin, D. C. Rovang, D. B. Sinars, S. A. Slutz, A. C. Owen, K. Tomlinson, M. R. Gomez, S. B. Hansen, M. C. Herrmann, M. C. Jones, J. L. McKenney, G. K. Robertson, G. A. Rochau, M. E. Savage, D. G. Schroen, and W. A. Stygar. Modified helix-like instability structure on imploding z-pinch liners that are pre-imposed with a uniform axial magnetic field. *Phys. Plasmas*, 21(5):056303, 2014.

[15] A. B. Sefkow, S. A. Slutz, J. M. Koning, M. M. Marinak, K. J. Peterson, D. B. Sinars, and R. A. Vesey. Design of magnetized liner inertial fusion experiments using the Z facility. *Phys. Plasmas*, 21(7):072711, 2014.

[16] M. R. Gomez, S. A. Slutz, A. B. Sefkow, D. B. Sinars, K. D. Hahn, S. B. Hansen, E. C. Harding, P. F. Knapp, P. F. Schmit, C. A. Jennings, T. J. Awe, M. Geissel, D. C. Rovang, G. A. Chandler, G. W. Cooper, M. E. Cuneo, A. J. Harvey-Thompson, M. C. Herrmann, M. H. Hess, O. Johns, D. C. Lamppa, M. R. Martin, R. D. McBride, K. J. Peterson, J. L. Porter, G. K. Robertson, G. A. Rochau, C. L. Ruiz, M. E. Savage, I. C. Smith, W. A. Stygar, and R. A. Vesey. Experimental demonstration of fusion-relevant conditions in magnetized liner inertial fusion. *Phys. Rev. Lett.*, 113:155003, Oct 2014.

[17] P. F. Schmit, P. F. Knapp, S. B. Hansen, M. R. Gomez, K. D. Hahn, D. B. Sinars, K. J. Peterson, S. A. Slutz, A. B. Sefkow, T. J. Awe, E. Harding, C. A. Jennings, G. A. Chandler, G. W. Cooper, M. E. Cuneo, M. Geissel, A. J. Harvey-Thompson, M. C. Herrmann, M. H. Hess, O. Johns, D. C. Lamppa, M. R. Martin, R. D. McBride, J. L. Porter, G. K. Robertson, G. A. Rochau, D. C. Rovang, C. L. Ruiz, M. E. Savage, I. C. Smith, W. A. Stygar, and R. A. Vesey. Understanding fuel magnetization and mix using secondary nuclear reactions in magneto-inertial fusion. *Phys. Rev. Lett.*, 113:155004, Oct 2014.

[18] M. R. Gomez, S. A. Slutz, A. B. Sefkow, K. D. Hahn, S. B. Hansen, P. F. Knapp, P. F. Schmit, C. L. Ruiz, D. B. Sinars, E. C. Harding, C. A. Jennings, T. J. Awe, M. Geissel, D. C. Rovang, I. C. Smith, G. A. Chandler, G. W. Cooper, M. E. Cuneo, A. J. Harvey-Thompson, M. C. Herrmann, M. H. Hess, D. C. Lamppa, M. R. Martin, R. D. McBride, K. J. Peterson, J. L. Porter, G. A. Rochau, M. E. Savage, D. G. Schroen, W. A. Stygar, and R. A. Vesey. Demonstration of thermonuclear conditions in magnetized liner inertial fusion experiments. *Phys. Plasmas*, 22(5):056306, 2015.

[19] S. B. Hansen, M. R. Gomez, A. B. Sefkow, S. A. Slutz, D. B. Sinars, K. D. Hahn, E. C. Harding, P. F. Knapp, P. F. Schmit, T. J. Awe, R. D. McBride, C. A. Jennings, M. Geissel, A. J. Harvey-Thompson, K. J. Peterson, D. C. Rovang, G. A. Chandler, G. W. Cooper, M. E. Cuneo, M. C. Herrmann, M. H. Hess, O. Johns, D. C. Lamppa, M. R. Martin, J. L. Porter, G. K. Robertson, G. A. Rochau, C. L. Ruiz, M. E. Savage, I. C. Smith, W. A. Stygar, R. A. Vesey, B. E. Blue, D. Ryutov, D. G. Schroen, and K. Tomlinson. Diagnosing magnetized liner inertial fusion experiments on Z. *Physics of Plasmas*, 22(5):056313, 2015.

[20] P. F. Knapp, P. F. Schmit, S. B. Hansen, M. R. Gomez, K. D. Hahn, D. B. Sinars, K. J. Peterson, S. A. Slutz, A. B. Sefkow, T. J. Awe, E. Harding, C. A. Jennings, M. P. Desjarlais, G. A. Chandler, G. W. Cooper, M. E. Cuneo, M. Geissel, A. J. Harvey-Thompson, J. L. Porter, G. A. Rochau, D. C. Rovang, C. L. Ruiz, M. E. Savage, I. C. Smith, W. A. Stygar, and M. C. Herrmann. Effects of magnetization on fusion product trapping and secondary neutron spectra. *Phys. of Plasmas*, 22(5):056312, 2015.

[21] D. V. Rose, D. R. Welch, E. A. Madrid, C. L. Miller, R. E. Clark, W. A. Stygar, M. E. Savage, G. A. Rochau, J. E. Bailey, T. J. Nash, M. E. Sceiford, K. W. Struve, P. A. Corcoran, and B. A. Whitney. Three-dimensional electromagnetic model of the pulsed-power *Z*-pinch accelerator. *Phys. Rev. ST Accel. Beams*, 13(1):010402, 2010.

[22] M. E. Savage, K. R. LeChien, M. R. Lopez, B. S. Stoltzfus, W. A. Stygar, D. S. Artery, J. A. Lott, and P. A. Corcoran. In *Proceedings of the 18th International Pulsed Power Conference, Chicago, Illinois*, pages 983–990. IEEE, 2011.

[23] Y. B. Khariton, V. N. Mokhov, V. K. Chernyshev, and V. B. Yakubov. *Usp. Fiziol. Nauk.*, 120:706, 1976.

[24] Y. B. Khariton, V. N. Mokhov, V. K. Chernyshev, and V. B. Yakubov. *Sov. Phys. Usp.*, 19(12):1032, 1976.

[25] V. N. Mokhov *et al. Sov. Phys. Dokl.*, 24:557, 1979.

[26] M. A. Sweeney and A. V. Farnsworth, Jr. High-gain, low-intensity ICF targets for a charged-particle beam fusion driver. *Nuclear Fusion*, 21(1):41, 1981.

[27] I. R. Lindemuth and M. M. Widner. Magnetohydrodynamic behavior of thermonuclear fuel in a preconditioned electron beam imploded target. *Phys. Fluids*, 24(4):746–753, 1981.

[28] I. R. Lindemuth and R. C. Kirkpatrick. Parameter space for magnetized fuel targets in inertial confinement fusion. *Nuclear Fusion*, 23(3):263, 1983.

[29] R. D. Jones and W. C. Mead. The physics of burn in magnetized deuterium-tritium plasmas: spherical geometry. *Nuclear Fusion*, 26(2):127, 1986.

[30] Akira Hasegawa, Hiroyuki Daido, Masayuki Fujita, Kunioki Mima, Masakatsu Murakami, Sadao Nakai, Katsunobu Nishihara, Kiyohisa Terai, and Chiyoe Yamanaka. Magnetically insulated inertial fusion: A new approach to controlled thermonuclear fusion. *Phys. Rev. Lett.*, 56:139–142, Jan 1986.

[31] I. R. Lindemuth, R. E. Reinovsky, R. E. Chrien, J. M. Christian, C. A. Ekdahl, J. H. Goforth, R. C. Haight, G. Idzorek, N. S. King, R. C. Kirkpatrick, R. E. Larson, G. L. Morgan, B. W. Olinger, H. Oona, P. T. Sheehey, J. S. Shlachter, R. C. Smith, L. R. Veeser, B. J. Warthen, S. M. Younger, V. K. Chernyshev, V. N. Mokhov, A. N. Demin, Y. N. Dolin, S. F. Garanin, V. A. Ivanov, V. P. Korchagin, O. D. Mikhailov, I. V. Morozov, S. V. Pak, E. S. Pavlovskii, N. Y. Seleznev, A. N. Skobelev, G. I. Volkov, and V. A. Yakubov. Target plasma formation for magnetic compression/magnetized target fusion. *Phys. Rev. Lett.*, 75:1953–1956, 1995.

[32] R. C. Kirkpatrick, I. R. Lindemuth, and M. S. Ward. *Fusion Technol.*, 27:201, 1995.

[33] J. H. Degnan, M. L. Alme, B. S. Austin, J. D. Beason, S. K. Coffey, D. G. Gale, J. D. Graham, J. J. Havranek, T. W. Hussey, G. F. Kiuttu, B. B. Kreh, F. M. Lehr, R. A. Lewis, D. E. Lileikis, D. Morgan, C. A. Outten, R. E. Peterkin, D. Platts, N. F. Roderick, E. L. Ruden, U. Shumlak, G. A. Smith, W. Sommars, and P. J. Turchi. Compression of plasma to megabar range using imploding liner. *Phys. Rev. Lett.*, 82:2681–2684, 1999.

[34] R. E. Siemon, I. R. Lindemuth, and K. F. Shoenberg. *Comm. Plasma Phys. Control. Fusion*, 18:363, 1999.

[35] M. M. Basko, A. J. Kemp, and J. Meyer ter Vehn. Ignition conditions for magnetized target fusion in cylindrical geometry. *Nuclear Fusion*, 40(1):59, 2000.

[36] A. J. Kemp, M. M. Basko, and J. Meyer ter Vehn. Ignition conditions for magnetically insulated tamped ICF targets in cylindrical geometry. *Nuclear Fusion*, 41(2):235, 2001.

[37] D. D. Ryutov and R. E. Siemon. *Comm. Plasma Phys. Control. Fusion*, 20:185, 2001.

[38] A. J. Kemp, M. M. Basko, and J. Meyer ter Vehn. Implosion and ignition of magnetized cylindrical targets driven by heavy-ion beams. *Nuclear Fusion*, 43(1):16, 2003.

[39] T. P. Intrator, J. Y. Park, J. H. Degnan, I Furno, C. Grabowski, S. C. Hsu, E. L. Ruden, P. G. Sanchez, J. M. Taccetti, M. Tuszewski, W. J. Waganaar, G. A. Wurden, S. Y. Zhang, and Zhehui Wang. A high-density field reversed configuration plasma for magnetized target fusion. *IEEE Trans. Plasma Sci.*, 32(1):152–160, Feb 2004.

[40] S. F. Garanin, V. I. Mamyshev, and V. B. Yakubov. Update on MAGO progress. In *2006 IEEE international conference on megagauss magnetic field generation and related topics*, pages 37–46, Nov 2006.

[41] John Nuckolls, Lowell Wood, Albert Thiessen, and George Zimmerman. Laser compression of matter to super-high densities: Thermonuclear (CTR) applications. *Nature*, 239(5368):139–142, Sep 1972.

[42] John Lindl. Development of the indirect-drive approach to inertial confinement fusion and the target physics basis for ignition and gain. *Phys. Plasmas*, 2(11):3933–4024, 1995.

[43] L. J. Perkins, R. Betti, K. N. LaFortune, and W. H. Williams. Shock ignition: A new approach to high gain inertial confinement fusion on the National Ignition Facility. *Phys. Rev. Lett.*, 103:045004, Jul 2009.

[44] N. B. Meezan, L. J. Atherton, E. J. Bond, D. A. Callahan, E. L. Dewald, S. Dixit, E. G. Dzenitis, M. J. Edwards, C. A. Haynam, D. E. Hinkel, O. S. Jones, O. Landen, R. A. London, P. A. Michel, J. D. Moody, J. L. Milovich, M. B. Schneider, C. A. Thomas, R. P. J. Town, A. L. Warrick, S. V. Weber, K. Widmann, S. H. Glenzer, L. J. Suter, B. J. MacGowan, J. L. Kline, G. A. Kyrala, and A. Nikroo. Erratum: National Ignition Campaign Hohlraum energetics [phys. plasmas17, 056304 (2010)]. *Phys. Plasmas*, 17(10):109901, 2010.

[45] O. A. Hurricane, D. A. Callahan, D. T. Casey, P. M. Celliers, C. Cerjan, E. L. Dewald, T. R. Dittrich, T. Doppner, D. E. Hinkel, L. F. Berzak Hopkins, J. L. Kline, S. Le Pape, T. Ma, A. G. MacPhee, J. L. Milovich, A. Pak, H. S. Park, P. K. Patel, B. A. Remington, J. D. Salmonson, P. T. Springer, and R. Tommasini. Fuel gain exceeding unity in an inertially confined fusion implosion. *Nature*, 506(7488):343–348, Feb 2014.

[46] Rolf Landshoff. Transport phenomena in a completely ionized gas in presence of a magnetic field. *Phys. Rev.*, 76:904–909, Oct 1949.

[47] D. D. Ryutov, M. S. Derzon, and M. K. Matzen. The physics of fast z pinches. *Rev. Mod. Phys.*, 72:167–223, Jan 2000.

[48] Patrick K. Rambo, Ian C. Smith, John L. Porter, Jr., Michael J. Hurst, C. Shane Speas, Richard G. Adams, Antonio J. Garcia, Ellis Dawson, Benjamin D. Thurston, Colleen Wakefield, Jeff W. Kellogg, Michael J. Slattery, Harry C. Ives, III, Robin S. Broyles, John A. Caird, Alvin C. Erlandson, James E. Murray, William C. Behrendt, Norman D. Neilsen, and

Joseph M. Narduzzi. Z-Beamlet: A multikilojoule, terawatt-class laser system. *Appl. Optics*, 44:2421–2430, 2005.

[49] D. C. Rovang, D. C. Lamppa, M. E. Cuneo, A. C. Owen, J. McKenney, D. W. Johnson, S. Radovich, R. J. Kaye, R. D. McBride, C. S. Alexander, T. J. Awe, S. A. Slutz, A. B. Sefkow, T. A. Haill, P. A. Jones, J. W. Argo, D. G. Dalton, G. K. Robertson, E. M. Waisman, D. B. Sinars, J. Meissner, M. Milhous, D. N. Nguyen, and C. H. Mielke. Pulsed-coil magnet systems for applying uniform 10–30 T fields to centimeter-scale targets on sandia's Z facility. *Rev. Sci. Instrum.*, 85(12):124701, 2014.

[50] G. B. Zimmerman and W. L. Kruer. *Comments Plasma Phys. Controlled Fusion*, 2:51, 1975.

[51] S. I. Braginskii. *Reviews of Plasma Physics*, volume 1. Consultants Bureau, New York, 1965.

[52] A. L. Velikovich, J. L. Giuliani, and S. T. Zalesak. Magnetic flux and heat losses by diffusive, advective, and Nernst effects in magnetized liner inertial fusion-like plasma. *Phys. Plasmas*, 22(4):042702, 2015.

[53] Ryan D. McBride and Stephen A. Slutz. A semi-analytic model of magnetized liner inertial fusion. *Phys. Plasmas*, 22(5):052708, 2015.

[54] J. B. Greenly, J. D. Douglas, D. A. Hammer, B. R. Kusse, S. C. Glidden, and H. D. Sanders. *Rev. Sci. Instrum.*, 79:073501, 2008.

[55] F. S. Felber, M. A. Liberman, and A. L. Velikovich. Methods for producing ultrahigh magnetic fields. *Applied Physics Letters*, 46(11):1042–1044, 1985.

[56] R. B. Baksht, A. L. Velikovich, B. A. Kablambaev, M. A. Liberman, A. V. Luchinskii, and N. A. Ratakhin. *Sov. Phys. Tech. Phys.*, 32:145, 1987.

[57] F. S. Felber, F. J. Wessel, N. C. Wild, H. U. Rahman, A. Fisher, C. M. Fowler, M. A. Liberman, and A. L. Velikovich. Ultrahigh magnetic fields produced in a gaspuff z pinch. *Journal of Applied Physics*, 64(8):3831–3844, 1988.

[58] F. S. Felber, M. M. Malley, F. J. Wessel, M. K. Matzen, M. A. Palmer, R. B. Spielman, M. A. Liberman, and A. L. Velikovich. Compression of ultrahigh magnetic fields in a gaspuff z pinch. *Phys. Fluids*, 31(7):2053–2056, 1988.

[59] S. A. Sorokin and S. A. Chaikovsky. Implosion of gas-puff liners with an initial axial magnetic field. *AIP Conference Proceedings*, 195(1):438–444, 1989.

[60] L.R. Veeser, P.J. Rodriguez, B.R. Marshall, W. Lewis, and O.M. Tatsenko. Optical magnetic field diagnostics for the MC1 flux compression generator experiments. In *Pulsed Power Conference, 1995. Digest of Technical Papers., Tenth IEEE International*, volume 2, pages 1058–1062 vol.2, July 1995.

[61] R. K. Appartaim and A. E. Dangor. Large magnetic fields generated by z-pinch flux compression. *Journal of Applied Physics*, 84(8):4170–4175, 1998.

[62] G.G. Zukakishvili, K.N. Mitrofanov, E.V. Grabovskii, and G.M. Oleinik. Measurements of the axial magnetic field during the implosion of wire arrays in the Angara-5-1 facility. *Plasma Physics Reports*, 31(8):652–664, 2005.

[63] O. V. Gotchev, P. Y. Chang, J. P. Knauer, D. D. Meyerhofer, O. Polomarov, J. Frenje, C. K. Li, M. J.-E. Manuel, R. D. Petrasso, J. R. Rygg, F. H. Séguin, and R. Betti. Laser-driven magnetic-flux compression in high-energy-density plasmas. *Phys. Rev. Lett.*, 103:215004, Nov 2009.

[64] O. V. Gotchev, J. P. Knauer, P. Y. Chang, N. W. Jang, M. J. Shoup, D. D. Meyerhofer, and R. Betti. Seeding magnetic fields for laser-driven flux compression in high-energy-density plasmas. *Rev. Sci. Instrum.*, 80(4):043504, 2009.

[65] Franklin S. Felber, Eduardo M. Waisman, and Michael G. Mazarakis. Combined flux compression and plasma opening switch on the Saturn pulsed power generator. *Phys. Rev. Lett.*, 104:185001, May 2010.

[66] J. P. Knauer, O. V. Gotchev, P. Y. Chang, D. D. Meyerhofer, O. Polomarov, R. Betti, J. A. Frenje, C. K. Li, M. J.-E. Manuel, R. D. Petrasso, J. R. Rygg, and F. H. Sguin. Compressing magnetic fields with high-energy lasers. *Phys. Plasmas*, 17(5):056318, 2010.

[67] S.A. Sorokin. High-magnetic-field generation by magnetic flux compression in imploding plasma liners. *Plasma Science, IEEE Transactions on*, 38(8):1723–1725, Aug 2010.

[68] P. Y. Chang, G. Fiksel, M. Hohenberger, J. P. Knauer, R. Betti, F. J. Marshall, D. D. Meyerhofer, F. H. Séguin, and R. D. Petrasso. Fusion yield enhancement in magnetized laser-driven implosions. *Phys. Rev. Lett.*, 107:035006, Jul 2011.

[69] H. Knoepfel. *Pulsed High Magnetic Fields*. North-Holland Publishing Company, Amsterdam, 1970.

[70] Graziella Bardotti, Bruno Bertotti, and Laura Gianolio. Magnetic configuration of a cylinder with infinite conductivity. *Journal of Mathematical Physics*, 5(10):1387–1390, 1964.

[71] Post-shot reports for MagLIF-related experiments on the Z pulsed-power accelerator. `https://sharepoint.sandia.gov/sites/maglif`.

[72] John Greenly, Matthew Martin, Isaac Blesener, David Chalenski, Patrick Knapp, and Ryan McBride. The role of flux advection in the development of the ablation streams and precursors of wire array z-pinches. *AIP Conference Proceedings*, 1088(1):53–56, 2009.

[73] J. B. Greenly. personal communication, 2015.

[74] James C. Simpson, John E. Lane, Christopher D. Immer, and Robert C. Yougquist. Simple analytic expressions for the magnetic field of a circular current loop. *NASA Technical Report No. NASA/TM-2013-217919*, 2001.

[75] M. R. Gomez, S. B. Hansen, K. J. Peterson, D. E. Bliss, A. L. Carlson, D. C. Lamppa, D. G. Schroen, and G. A. Rochau. Magnetic field measurements via visible spectroscopy on the Z machine. *Rev. Sci. Instrum.*, 85(11):11E609, 2014.

[76] F. F. Chen. *Introduction to Plasma Physics and Controlled Fusion*. Plenum Press, 2nd edition, 1984.

[77] Illustration of the fiber-based Faraday effect. `https://en.wikipedia.org/wiki/Faraday_effect`. Accessed October 5, 2015.

[78] L. Sun. *All-fiber Faraday Devices Based on Terbium-doped Fiber*. PhD thesis, University of Rochester, 2010.

[79] L. Sun, S. Jiang, and J. R. Marciante. Compact all-fiber optical Faraday components using 65-wt%-terbium-doped fiber with a record Verdet constant of –32 rad/(Tm). *Opt. Express*, 18(12):12191–12196, Jun 2010.

[80] L. Sun, S. Jiang, and J. R. Marciante. All-fiber optical magnetic-field sensor based on Faraday rotation in highly terbium-doped fiber. *Opt. Express*, 18(6):5407–5412, Mar 2010.

[81] L. Sun, S. Jiang, J. D. Zuegel, and J. R. Marciante. All-fiber optical isolator based on Faraday rotation in highly terbium-doped fiber. *Opt. Lett.*, 35(5):706–708, Mar 2010.

[82] William L. Baker, Miles C. Clark, James H. Degnan, Gerald F. Kiuttu, Charles R. McClenahan, and Robert E. Reinovsky. Electromagnetic-implosion generation of pulsed high-energy-density plasma. *Journal of Applied Physics*, 49(9):4694–4706, 1978.

[83] T. W. Hussey, N. F. Roderick, and D. A. Kloc. Scaling of (MHD) instabilities in imploding plasma liners. *Journal of Applied Physics*, 51(3):1452–1463, 1980.

[84] R. E. Reinovsky, W. E. Anderson, W. L. Atchison, C. E. Ekdahl, R. J. Faehl, I. R. Lindemuth, D. V. Morgan, M. Murillo, J. L. Stokes, and J. S. Shlachter. Instability growth in magnetically imploded high-conductivity cylindrical liners with material strength. *IEEE Trans. Plasma Sci.*, 30(5):1764–1776, Oct 2002.

[85] P.J. Turchi, K. Alvey, C. Adams, B. Anderson, H.D. Anderson, W.E. Anderson, E. Armijo, W.L. Atchison, J. Bartos, R.L. Bowers, B. Cameron, T. Cavazos, S. Coffey, R. Corrow, J.H. Degnan, J. Echave, B. Froggett, D. Gale, F. Garcia, J.A. Guzik, B. Henneke, R.J. Kanzleiter, G. Kiuttu, C. Lebeda, R.T. Olson, D. Oro, J.V. Parker, Jr. Peterkin, R.E., K. Peterson, R. Pritchett, R.B. Randolph, R.E. Reinovsky, J. Roberts, G. Rodriguez, D. Sandoval, G. Sandoval, M.A. Salazar, W. Sommars, W. Steckle, J.L. Stokes, J. Studebaker, L. Tabaka, and A.J. Taylor. Design, fabrication, and operation of a high-energy liner implosion experiment at 16 megamperes. *Plasma Science, IEEE Transactions on*, 30(5):1777–1788, Oct 2002.

[86] R. L. Bowers, J. H. Brownell, H. Lee, K. D. McLenithan, A. J. Scannapieco, and W. R. Shanahan. Design and modeling of precision solid liner experiments on Pegasus. *Journal of Applied Physics*, 83(8):4146–4159, 1998.

[87] J P Chittenden, S V Lebedev, C A Jennings, S N Bland, and A Ciardi. X-ray generation mechanisms in three-dimensional simulations of wire array z-pinches. *Plasma Phys. Controlled Fusion*, 46(12B):B457, 2004.

[88] Allen C. Robinson and Christopher J. Garasi. Three-dimensional z-pinch wire array modeling with ALEGRA-HEDP. *Comput. Phys. Commun.*, 164(13):408–413, 2004.

[89] Allen C. Robinson, Thomas A. Brunner, Susan Carroll, Richard Drake, Christopher J. Garasi, Thomas Gardiner, Thomas Haill, Heath Hanshaw, David Hensinger, Duane Labreche, Raymond Lemke, Edward Love, Christopher Luchini, Stewart Mosso, John Niederhaus, Curtis C. Ober, Sharon Petney, William J. Rider, Guglielmo Scovazzi, O. Erik Strack, Randall Summers, Timothy Trucano, V. Greg Weirs, Michael Wong, and Thomas Voth. ALEGRA: An arbitrary Lagrangian-Eulerian multimaterial, multiphysics code. In *Proceedings of the 46th AIAA Aerospace Sciences Meeting and Exhibit, 7–10 January 2008, Reno, Nevada*. AIAA, 2008.

[90] Marc Jobe. Sandia National Laboratories Memorandum, September 22, 2015.

Appendix A

An obsolete lens-coupled setup for SVS measurements on Z

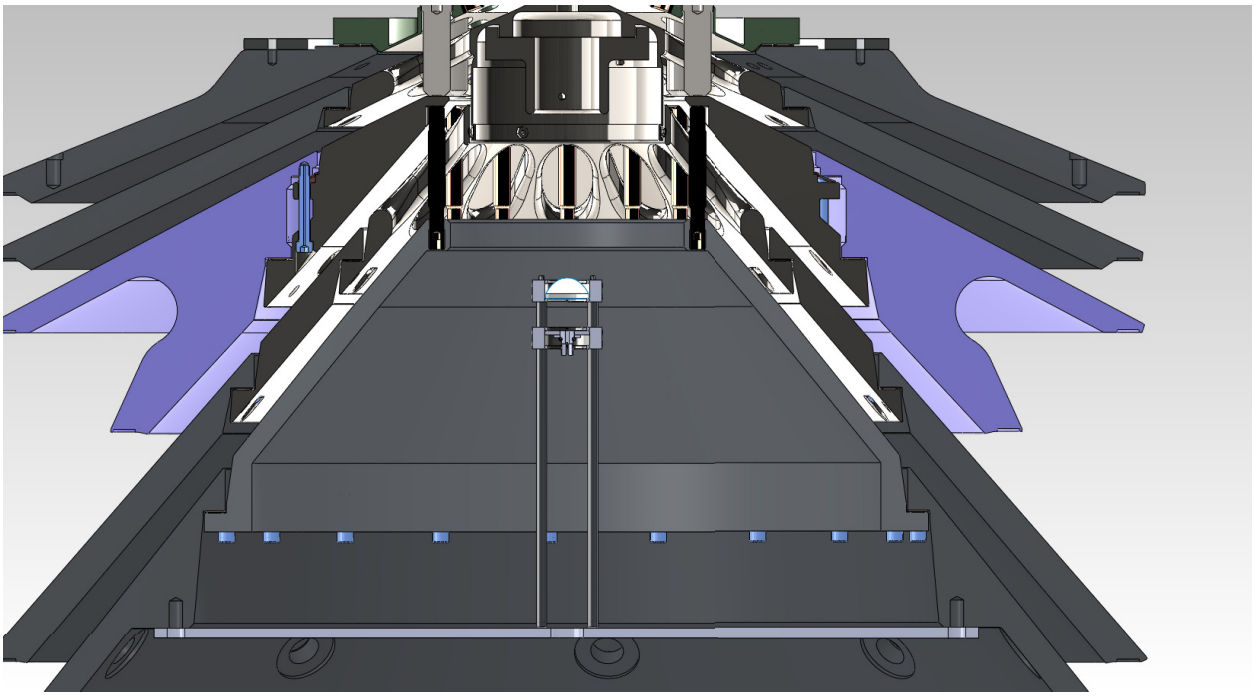

Figure A.1: The lens-coupled SVS setup used on Z shots 2493, 2494, and 2537. This system collected too much background light to be useful. This background light was probably emitted from the double post-hole convolute structure on Z. For this reason, we switched to the target-mounted fiber optic setup shown in Fig. 3.1.

Appendix B

GORGON simulations to study the effects of the metallic load hardware on the dynamic fringe fields

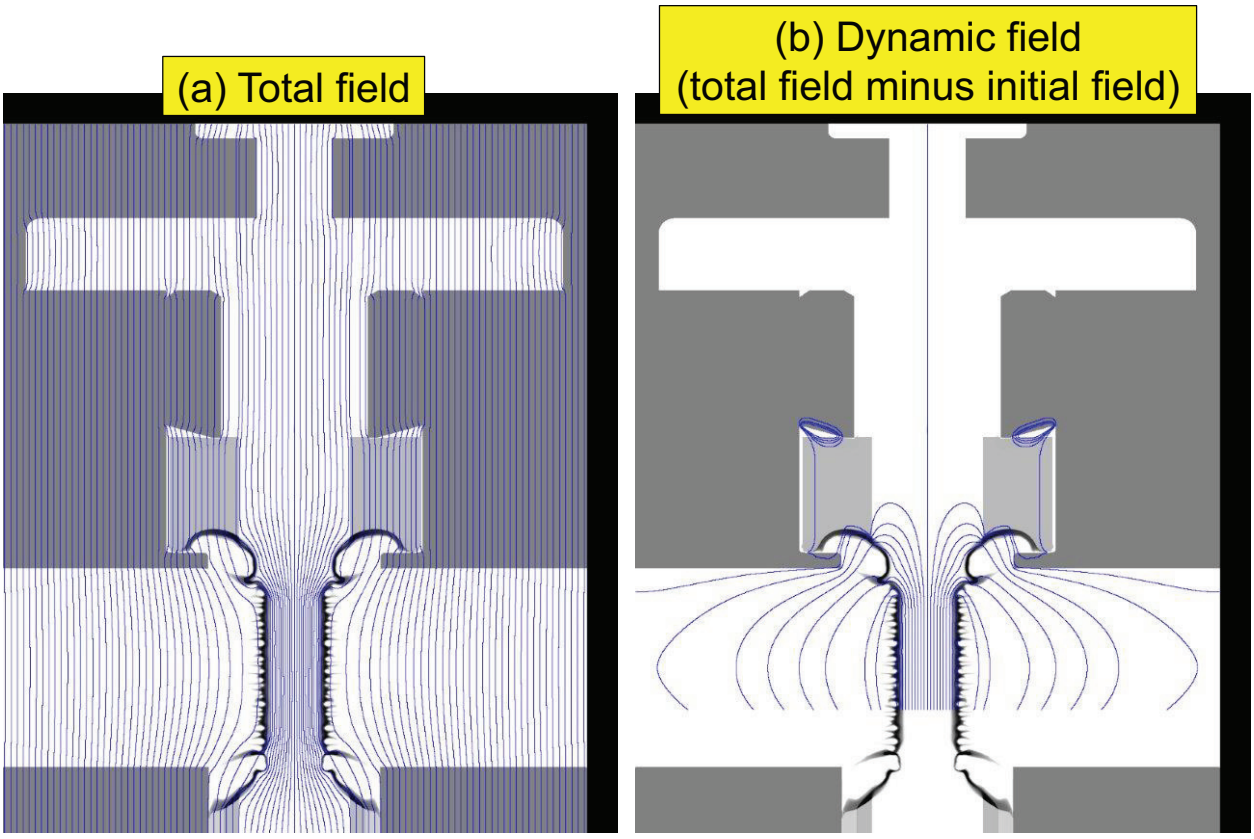

Figure B.1: GORGON simulations to study the effects of the surrounding metallic load hardware on the dynamic fringe fields. The resulting field lines are similar to those of the simple model presented in Fig. 2.1, thus ruling out the hypothesis that the surrounding metal structures are somehow responsible for the anomalously large fringe field signals presented in Fig. 3.13. Furthermore, additional GORGON simulations (not shown here) showed that an on-axis plasma jet propagating upward could indeed be the reason for the anomalously large fringe field signals of Fig. 3.13.

Appendix C

GORGON design simulations to compare a plastic liner fill with a vacuum liner fill

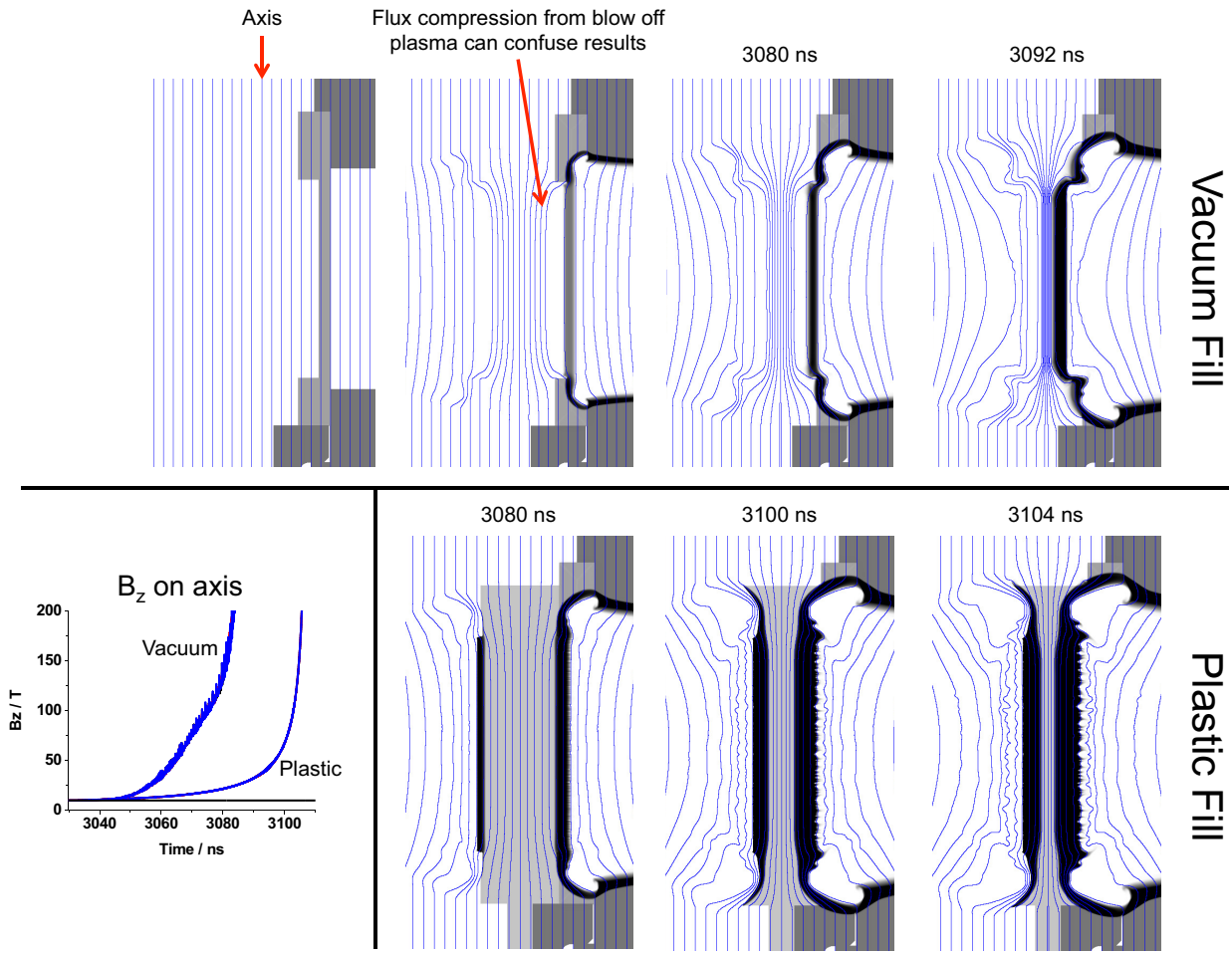

Figure C.1: GORGON design simulations to compare a plastic liner fill with a vacuum liner fill. The motivation for the plastic liner fill was to remove any ambiguity (in both experiments and simulations) caused by low density plasmas injected into the liner's interior by completely filling the liner's interior with solid, low-density dielectric. The low mass density of the nylon fill would allow the liner to implode fairly unimpeded. Unfortunately, this target broke during assembly and thus was never tested. Nevertheless, this target could have been successful and therefore we document it here.

Appendix D

Conference presentations associated with this LDRD project

1. *Invited*—R. D. McBride, K. J. Peterson, T. J. Awe, D. B. Sinars, M. R. Gomez, S. B. Hansen, C. A. Jennings, S. A. Slutz, M. R. Martin, R. W. Lemke, D. E. Bliss, P. F. Knapp, P. F. Schmit, D. C. Rovang, and M. E. Cuneo, "Experiments on Liner Dynamics and Magnetic Flux Compression for MagLIF", at the *26th IEEE Symposium on Fusion Engineering*, (Austin, May 31–June 4, 2015).

2. *Invited*—M. R. Gomez, "Measuring magnetic fields in magnetized liner inertial fusion experiments: past successes and future opportunities", at the *4th Magnetic Fields in Laboratory High Energy Density Plasmas (LaB) Meeting at Princeton University*, (Princeton, November 11–13, 2015).

3. R. D. McBride, M. R. Gomez, S. B. Hansen, C. A. Jennings, D. E. Bliss, P. F. Knapp, P. F. Schmit, T. J. Awe, M. R. Martin, D. B. Sinars, J. B. Greenly, T. P. Intrator, and T. E. Weber, "Magnetic flux compression experiments on the Z pulsed-power accelerator", at the *56th Annual Meeting of the American Physical Society Division of Plasma Physics*, (New Orleans, October 27–31, 2014).

4. M. R. Gomez, S. B. Hansen, K. J. Peterson, R. D. McBride, C. A. Jennings, D. E. Bliss, A. L. Carlson, D. C. Lamppa, D. G. Schroen, D. J. Ampleford, T. J. Awe, J. E. Bailey, A. J. Harvey-Thompson, B. Jones, P. F. Knapp, M. E. Cuneo, G. A. Rochau, and D. B. Sinars, "Magnetic Field Measurements via Visible Spectroscopy on the Z Machine", at the *20th Topical Conference on High-Temperature Plasma Diagnostics*, (Atlanta, June 1–5, 2014).

5. D. E. Bliss, R. D. McBride, D. C. Lamppa, and T. P. Intrator, "Measurement of Magnetic Flux Compression in Imploding Liners by Faraday Rotation in Tb Doped Optical Fibers", at the *20th Topical Conference on High-Temperature Plasma Diagnostics*, (Atlanta, June 1–5, 2014).

6. R. D. McBride, D. C. Lamppa, D. C. Rovang, T. J. Awe, J. B. Greenly, M. R. Martin, C. A. Jennings, M. R. Gomez, S. B. Hansen, M. H. Hess, T. P. Intrator, A. C. Owen, S. A. Slutz, C. W. Nakhleh, D. B. Sinars, M. E. Cuneo, and M. C. Herrmann, "Implementing and Diagnosing Magnetic Flux Compression on Z", at the *NNSA Laboratory Directed Research and Development Symposium*, (Washington D.C., June 12, 2013).

DISTRIBUTION:

1 Thomas Weber
P-24 Plasma Physics
Bikini Atoll Road, SM 30
Los Alamos National Laboratory
Los Alamos, NM 87545

1 John Greenly
Cornell University
439 Rhodes Hall
Ithaca, NY 14853

1	MS 0352	Lu Fang, Org. 1718
1	MS 0359	Donna Chavez, LDRD Office, Org. 1911
3	MS 1168	Kurt Tomlinson, Gary Smith, and Reny Paguio, Org. 1683
2	MS 1182	Derek Lamppa and Marc Jobe, Org. 5445
30	MS 1193	Ryan McBride, Org. 1688
1	MS 0899	Technical Library, 9536 (electronic copy)


Sandia National Laboratories